Charge Dynamics in Novel Semiconductors

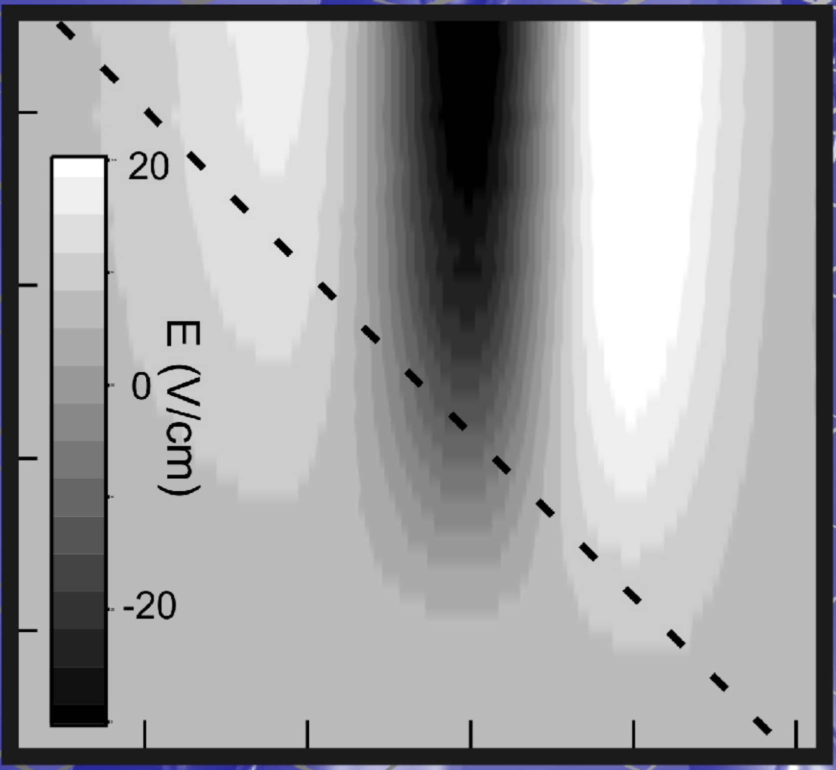

Euan Hendry

Charge Dynamics in Novel Semiconductors

ACADEMISCH PROEFSCHRIFT

ter verkrijging van de graad van doctor
aan de Universiteit van Amsterdam
op gezag van de Rector Magnificus
prof. mr. P.F. van der Heijden
ten overstaan van een door het college voor promoties
ingestelde commissie in het openbaar te verdedigen
in de Aula der Universiteit
op vrijdag 25 november 2005, te 10.00 uur

door

Euan Hendry
geboren te Bellshill, Schotland

Promotiecommissie

Promotor	Prof. Dr. M. Bonn
Overige leden	Prof. Dr. L.D.A. Siebbeles
	Prof. Dr. T. Gregorkiewicz
	Prof. Dr. H.B. van Linden van den Heuvell
	Dr. P.C.M. Planken
	Prof. Dr. A.W. Kleyn
	Prof. Dr. T.F. Heinz
	Prof. Dr. H.J. Bakker

Faculteit der Natuurwetenschappen, Wiskunde en Informatica.

ISBN: 90-6464-461-6

Publications

This thesis is based on the following publications:

Chapter 3:
J.M. Schins, E. Hendry, M. Koeberg, M. Bonn and H.G. Muller.
“On the physical meaning of the third-order susceptibility in phase-resolved pump-probe spectroscopy”
(in preparation)

Chapter 4:
E. Hendry, F. Wang, J. Shan, T.F. Heinz and M. Bonn.
“Electron transport in TiO_2 probed by THz time-domain spectroscopy”
PHYSICAL REVIEW B **69**, 081101(R) (2004)

M. Bonn., F. Wang, J. Shan, T.F. Heinz and E. Hendry.
“Ultrafast scattering of electrons in TiO_2”
FEMTOCHEMISTRY AND FEMTOBIOLOGY, eds. M.M. Martin and J.T. Hynes, Elsevier, 517 (2004)

E. Knoesel, J. Shan, F. Wang, E. Hendry, M. Bonn, T.F. Heinz.
“Probing electrical conductivity in liquids and solids by THz time-domain spectroscopy”
ABSTRACTS OF PAPERS OF THE AMERICAN CHEMICAL SOCIETY **226**, U342 481-PHYS Part 2 (2003)

E. Hendry, F. Wang, J. Shan, T.F. Heinz and M. Bonn.
“Intermediate size polarons in rutile type TiO_2”
(in preparation)

E. Hendry, M. Koeberg and M. Bonn.
“Charge-charge interactions in semiconductors”
(in preparation)

E. Hendry, M. Koeberg, Brian O'Regan and M. Bonn.
“Electron transport in porous TiO_2”
(in preparation)

Chapter 5:

E. Hendry, M. Koeberg and M. Bonn.
"Dynamics of exciton formation in ZnO"
(in preparation)

E. Hendry, M. Koeberg and M. Bonn.
"Cooling dynamics above and below the Mott density in a direct gap semiconductor"
(in preparation)

Chapter 6:

E. Hendry, M. Koeberg, F. Wang, T.F. Heinz, H. Zhang, C. de Mello Donega, D.A.M. Vanmaekelbergh and M. Bonn.
"Direct observation of electron to hole energy transfer in CdSe quantum dots"
(Submitted to PHYSICAL REVIEW LETTERS)

Chapter 7:

E. Hendry, J.M. Schins, L. P. Candeias, L. D. A. Siebbeles, and M. Bonn.
"Efficiency of exciton and charge carrier photogeneration in a semiconducting polymer"
PHYSICAL REVIEW LETTERS **92**, 196601 (2004)

E. Hendry, M. Koeberg, J.M. Schins, L. D. A. Siebbeles, and M. Bonn.
"Ultrafast charge generation in a semiconducting polymer studied with THz emission spectroscopy"
PHYSICAL REVIEW B **70**, 033202 (2004)

E. Hendry, M. Koeberg, J.M. Schins, H. K. Nienhuys, V. Sundström, L. D. A. Siebbeles, and M. Bonn.
"Interchain effects in the ultrafast photophysics of a semiconducting polymer: THz time-domain spectroscopy of thin films and isolated chains in solution"
PHYSICAL REVIEW B **71**, 125201 (2005)

E. Hendry, M. Koeberg, J.M. Schins, L. D. A. Siebbeles, and M. Bonn.
"Sub-picosecond excitation dynamics of PCBM-polymer blends"
(in preparation)

Contents

Chapter 1 Introduction Page

Chapter 2 Experimental Techniques

Chapter 3 Analysis of THz-TDS measurements

Chapter 4 Electron transport in TiO_2 and TiO_2 solar cells

Chapter 5 Exciton formation in ZnO

Chapter 6 Exciton cooling in CdSe quantum dots

Chapter 7 Charge generation in conjugated polymers

Chapter 1

Introduction

1.1 Background

Electrical conductivity (a measure of how well a material supports the transport of electrical charge in response to an externally applied electric field) is a key property governing the application of most materials in electrical devices. Metals are good conductors, since they have many free (mobile) electrons, and have correspondingly large values of conductivity >100 S/m. Insulating materials, on the other hand, have conductivities $<10^{-6}$ S/m. Semiconductors are a class of materials that can be engineered to either conduct or insulate. This property makes semiconductors essential in the design of many electrical components and devices.

Most current semiconductor devices are made from silicon and germanium. In the last decade, however, new semiconducting materials, with compositions and structures different from crystalline silicon, have emerged. These have many advantages over the more traditional semiconductors. In this thesis, the electrical properties of some of these novel materials are investigated using a combination of ultrafast, laser based techniques. Such techniques allow the investigation of fast conduction processes in real time, providing new insights into the fundamental properties of novel semiconductors and their suitability for application in electronics.

1.2 Electronic structure of semiconductors

In the quantum mechanical picture, the wave nature of the electron gives rise to specific electronic states, each characterized by a specific wavelength (λ_e), dependent on the electron's energy and momentum. In a crystal, these electron waves can interact with the lattice potential: a periodic lattice consisting of a repeating unit of atoms gives rise to mirror planes in the structure which can act as reflectors for the electron wave. In figure 1.1, the case of an electron wave in a one-dimensional lattice is shown. When the wavelength of the electron is comparable to the separation of mirror planes, reflected waves combine to interfere destructively with the forward traveling wave. States corresponding to such electron wavelengths are forbidden and are referred to as (band) gap states.

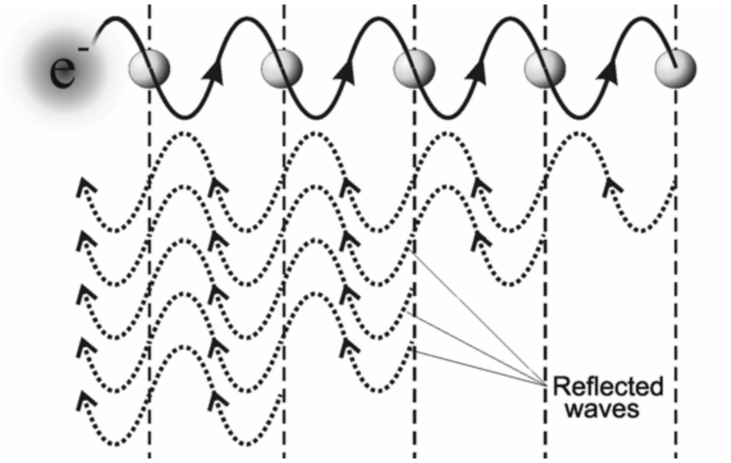

Figure 1.1 Wave representation (solid line) of an electron in a periodic lattice, the atoms represented as grey spheres. Mirror planes (dashed lines) cause reflection of the electron wave (dotted lines). When the wavelength of the electron corresponds to the separation of mirror planes, reflected waves combine to interfere destructively with the forward traveling wave.

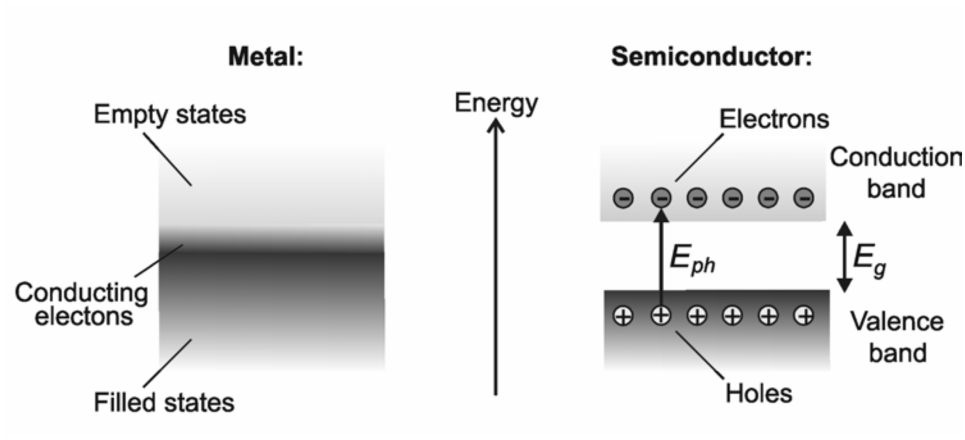

Figure 1.2 Left: Energy continuum of a metal. Right: Energy band structure of a semiconductor, with band gap E_g. Photoexcitation with photons with energy $E_{ph}>E_g$ results in mobile electrons in the conduction band and corresponding mobile holes in the valence band.

According to the Pauli exclusion principle, each electron state can only be occupied by one electron at any one time, leading to a build up of occupied states, with increasing energy (see figure 1.2). Well away from the band gap energies, the density of states is very high, and can be approximated by a continuum. In figure 1.2 the energy structure in a metal, with its quasi-continuum of energy states, is compared to that of a semiconductor/insulator with a gap in the allowed energy states (described band gap energy E_g). In a pure semiconductor, states below the band gap (valence band) are fully occupied, while states above the band gap (conduction band) are empty. Since the valence band states are fully occupied, and electrons in these states have no available momentum states to move into, they do not contribute to the material conductivity. Instead, only electrons excited into the upper band are involved in the conduction process. At temperatures around absolute zero, the dark conductivity (i.e. in the absence of light) in a semiconductor is therefore zero. The distinction between a semiconductor and an insulator can be made by the size of the band gap: though the exact definitions are somewhat arbitrary, a rule of thumb is E_g<2 eV for a semiconductor and E_g>2 eV for an insulator.

Mobile electrons can be introduced in the conduction band of a semiconductor by doping – either chemically or by photo-injection. Photoexciting a semiconductor (or insulator) with photons of light of energy (E_{ph}) larger than E_g can generate excited mobile electrons in the conduction band, and can increase conductivity by orders of magnitude. In this case, the vacancy the electron leaves upon excitation is also mobile, and is referred to as a hole. A hole behaves much like a positively charged electron. The subsequent equilibration – cooling – of these initially 'hot' charge carriers (electrons and holes) to energy levels around the band gap occurs by carrier-carrier and carrier-phonon scattering. These processes are well understood in bulk semiconductors and typically occur on (sub-)picosecond timescales [3].

Just above and below the band gap, electrons and holes do not behave as if they were in vacuum. In these electronic states, wave interference due to the interaction with the periodic lattice modifies the characteristics from those of a free electron of the same energy. This means the properties of an electron are not determined by just one traveling wave, but by the sum of all forward and back-reflected waves in the material (see figure 1.1). To account for this, the concept of an effective band mass has been introduced. The band mass (m^*) of an electron (or hole) is the mass the particle appears to have when moving through a periodic crystal. Since the wavelength of an electron in the conduction band is slightly different from that of its corresponding hole in the valence band, wave interference results in quasiparticles with different band masses. This difference can be very large: in the case of silicon, the electron band mass relevant for describing conductivity just above the gap is $0.32m_e$ (with m_e the free electron mass), while the hole band mass is $0.49m_e$. Band mass can also vary a lot from material to material: for example, the electron band mass in gallium arsenide is $0.067m_e$.

1.3 The Drude model for electron transport

The simplest model for electron transport is the Drude model. This is a purely classical model, based on the application of kinetic theory to a non-interacting electron gas. By treating the electrons in the conduction band as quasi-particles with modified mass m^*, the description of a classical gas of charge carriers can be adopted for many semiconductors. If the material is photo-doped, then after the initial cooling period, the mobile carriers are in thermal equilibrium with the crystal lattice (temperature T), and the root mean square speed of the thermal distribution is given by $v = \sqrt{3k_bT/m^*}$, with k_b the Boltzmann constant.

In the Drude model, the conduction electrons in a semiconductor are considered free, interacting with the lattice only through momentum altering collisions. In the absence of an electric field (solid line in figure 1.3) the velocity of an electron remains, on average, constant in-between collisions, and motion through the lattice follows a random walk with mean free path l_r. The direction of the electron's velocity after a collision is considered random, such that the time-averaged velocity is zero. In an applied field $\boldsymbol{E}$, preferential acceleration between collisions in the direction opposite of the field induces a drift velocity $\boldsymbol{v}_\mathbf{d}$ in the electron motion (dotted line in figure 1.3). For ordinary currents in semiconductors, $\boldsymbol{v}_\mathbf{d}$ is on the order of millimeters per second, much smaller than the average thermal electron speed, which is on the order of a hundred thousand meters per second at room temperature.

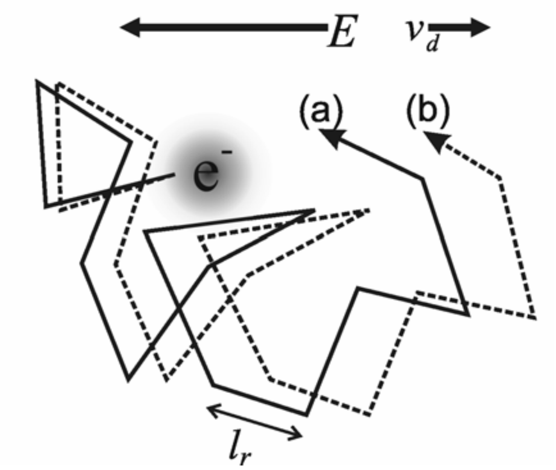

Figure 1.3 Top: In the Drude model, the electron is considered free, only interacting with the lattice through elastic collisions with ions. In the absence of an electric field (solid line, (a)) the velocity of the electron remains constant in-between the momentum altering collisions. The electron then follows a random walk through the lattice, described by a mean free path l_r. Since collisions are random, the time-averaged velocity is zero. In the presence of a static electric field $\boldsymbol{E}$, the electrons are accelerated in-between collisions (dotted line, (b)) such that the time averaged velocity has a non-zero component $\boldsymbol{v}_d$ in the opposite direction to the applied field.

From a classical point of view, one might expect that the electrons are scattered by the constituent atoms in the lattice, leading to a mean free path that is on the order of the unit cell of the crystal. In reality, the mean free path is much larger. In the quantum mechanical picture, the electrons must be pictured as waves, which can propagate through the oscillating potential of a perfect lattice without scattering. Instead, the electron scatters from imperfections and distortions in the lattice structure, leading to much longer mean free paths, typically orders of magnitude larger than the lattice spacing in the crystal [2]. Acceleration is damped by a frictional force due these elastic collisions, characterized by average time τ_r between collisions. This damping accounts for the observed resistance to current. In the case of a time varying field $\boldsymbol{E}(t)$, the motion is described by the first order differential equation:

$$\frac{\partial}{\partial t} v_d(t) + \frac{1}{\tau_r} v_d(t) = -\frac{e}{m^*} E(t), \tag{1.1}$$

where e is the elementary charge of an electron. For a sinusoidal field $E = E_0 e^{-i\omega t}$, differential equation (1.1) has the solution:

$$v_d = -\frac{e\tau_r}{m^*} \frac{1}{1 - i\omega\tau_r} E_0 e^{i\omega t}. \tag{1.2}$$

Since the magnitude of the drift velocity is dependent on the magnitude of the applied driving field, it is convenient to define an electron mobility μ, the proportionality factor between $\boldsymbol{E}$ and $\boldsymbol{v_d}$:

$$\mu(\omega) = \frac{e\tau_r}{m^*} \frac{1}{1 - i\omega\tau_r}. \tag{1.3}$$

The electron mobility is a measure of how easily an electron moves through a material: when the time between collisions is small, the electrons are relatively immobile and are not easily perturbed by an applied field. Often, this property is expressed in terms of the DC (direct current) mobility measured at frequency ω=0.

The electrical properties of a material on a macroscopic scale can be dependent on a large density N of mobile electrons, all responding to the applied field. It is therefore useful to define a material conductivity:

$$\sigma(\omega) = Ne\mu(\omega), \tag{1.4}$$

or

$$\sigma(\omega) = \frac{\varepsilon_0 \omega_p^2 \tau_r}{1 - i\omega\tau_r}, \omega_p^2 = \frac{e^2 N}{\varepsilon_o m^*}, \tag{1.5}$$

where ω_p is the plasma frequency, and ε_0 the vacuum permittivity. Conductivity is an intrinsic material property and does not depend on the dimensions of the material.

The Drude model, in its primitive form described here, contains some drastic simplifications. For example:

(1) The Drude model incorporates interaction of an electron with the lattice only through scattering. This is called the *free electron approximation*, and can only be applied to non-polarizable materials. By incorporating the Coulomb interaction of conduction electrons with (partially) charged atoms of the lattice, the Drude model can be extended to describe conductivity in polarizable semiconductors (see section 1.4).

(2) The conduction electrons are treated as an ideal classical gas, whereas the electron density can be orders of magnitude higher than what can be considered "ideal". The neglect of electron-electron interactions is named the *independent electron approximation* (see section 1.5).

(3) All mobile electrons are treated equivalently: the mass and the scattering time are independent of the velocity of the electron, and assumed to be isotropic. A distribution of electron velocities and scattering times, however, can lead to deviations from the Drude model. There are more general models which can account for these deviations [1].

Because of these simplifications, the Drude model for conductivity fails to describe some basic observations in solid state physics. For example, the Drude model brakes down at high field and/or high electron density. However, even with the drastic approximations involved, the Drude Model is quite successful in explaining a large number of observations regarding the conductivity of both metals and semiconductors.

1.4 Polarons: breakdown of the free electron approximation

In a polarizable semiconductor, the constituent atoms retain a (partial) positive or negative ionic charge, and a negatively charged electron (or a positively charged hole) can interact with the ionic lattice through repulsive and attractive Coulomb interactions. A conduction electron (or hole) together with its self-induced polarization in a lattice forms a quasiparticle, which is called a polaron (figure 1.4).

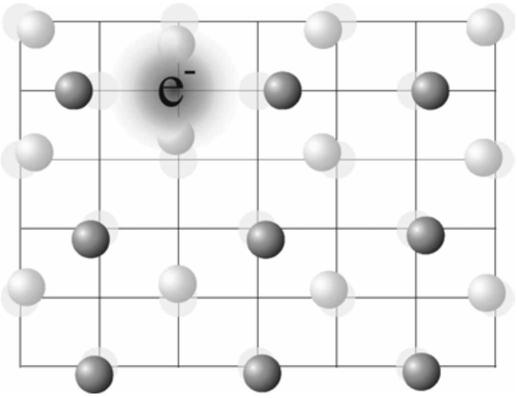

Figure 1.4 In a polarizable lattice (assembled from positive and negative ions) the presence of a negatively charged electron distorts the lattice around it, attracting the positive ions (light gray) while repelling the negative ions (dark grey). As this electron moves through the lattice, it must drag this distortion with it, giving rise to the polaron quasi particle: an electron dressed with a lattice deformation.

The physical properties of a polaron can differ greatly from those of a free electron, depending on the strength of the coupling to the lattice (described by coupling constant α_{ph}) [4, 5]. In the weak coupling regime (α_{ph}<1), large polarons, with spatially extended wavefunctions, are formed. In this picture a conduction electron entrains the lattice deformation, resulting in an effective (or polaron) mass m^{**} exceeding its band mass, and exhibits Drude like conduction. For a sufficiently strong interaction (α_{ph}>10), small polarons are formed. These electrons (or holes) are self-trapped within the potential well caused by the lattice deformation. Small polaron conductivity is very low, since charge transport can only occur through tunneling or hopping from one local site to the next. In chapter 4 of this thesis, the properties of polarons in titanium dioxide are investigated.

1.5 Breakdown of the independent electron approximation

At high densities, carrier-carrier interactions begin to play a role in the conductive response of a material. Collisions between electrons do not directly alter the combined momentum and hence should not be included as a momentum scattering event within the Drude model. Electron-electron interactions do, however, play a role through the Pauli exclusion principle, which states that no two electrons (or holes) may occupy the same state. At high electron (or hole) densities, this leads to occupation of high energy states. In this high density regime, the breakdown of the independent electron approximation means that the conducting electron gas cannot be described as a classical kinetic gas. The average velocity of an electron gas in this regime can be orders of magnitude higher than that predicted by classical kinetic theory. In metals, where the electron density is high, typical electron velocities can approach one tenth of the speed of light. In chapter 4, carrier-carrier interactions in highly photo-excited titanium dioxide are compared to those in silicon.

1.6 Excitons

Electron-electron effects cause a breakdown of the independent electron approximation in the *high* density regime. Since they result from the same excitation, however, electron-hole coulomb interactions can cause a breakdown of the independent electron approximation even in the *low* density regime. In many materials, the coulomb interaction between the electron and its associated hole is strong enough to enable binding (described by energy E_b). The resulting quasi-particle is called an exciton. Since the combined charge of an electron-hole pair is zero, excitons are insulating particles and do not contribute to the DC conductivity. However, the strong electron-hole correlation means that excitons have a high radiative recombination probability. The high luminescence yield of excitonic materials makes them important building blocks of many electro-optical devices, especially in optical displays and light emitting diodes (LEDs).

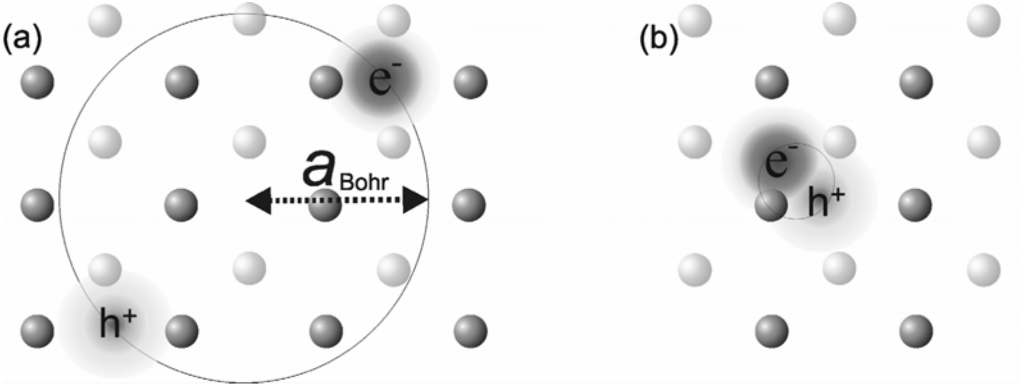

Figure 1.5 Depending on the magnitude of the exciton binding energy electrons and holes pair to form (a) Wannier excitons (weakly bound, with the average distance between the electron and hole larger than the lattice spacing) or (b) Frenkel excitons (strongly bound, with the average distance between the electron and hole of the order or smaller than the lattice spacing).

Excitons can be treated in two limiting cases (see figure 1.5), depending on the strength of the electron-hole interaction [7]. The strength of this interaction is determined the screening effect of the surrounding lattice: polarizable lattices, with high dielectric function ε, screen the electron-hole attraction, resulting in a small exciton binding energy (typically $E_b < 0.1$ eV). At low temperatures, this results in a Wannier exciton, which has a spatial extent much larger than the lattice spacing of the crystal. Since the exciton extends over several crystal unit cells, the effect of the lattice potential can be incorporated into the effective masses of the constituent electron and hole, and the exciton has solutions to the Schrödinger equation similar to those of the hydrogen atom. Because of the lower masses and the screened Coulomb interaction, the binding energy is much lower than a hydrogen atom and the Bohr radius (a_{Bohr}) is considerably larger than the typical size of an atom (see figure 1.5). In less polarizable lattices (low ε), the high exciton binding energy results in strongly bound Frenkel excitons, with a spatial extension of the same order as the interatomic distance of the crystal.

Excitons have many properties similar to atoms, including their electronic structure and interactions with other particles. For this reason, excitons are sometimes referred to as "artificial atoms". Energy levels are discreet, much like in atoms (analogously assigned state descriptions 1S, 2S, 2P etc – see figure 1.6): strongly bound excitons have very large energy level spacing, while weakly bound excitons have a much denser energy level structure. In the limit of no electron-hole coupling, the energy level density increases to that of the band structure (and the charges can be considered free). In chapter 5, the formation of a gas of strongly bound excitons from an initially excited hot free electron and hole plasma is studied.

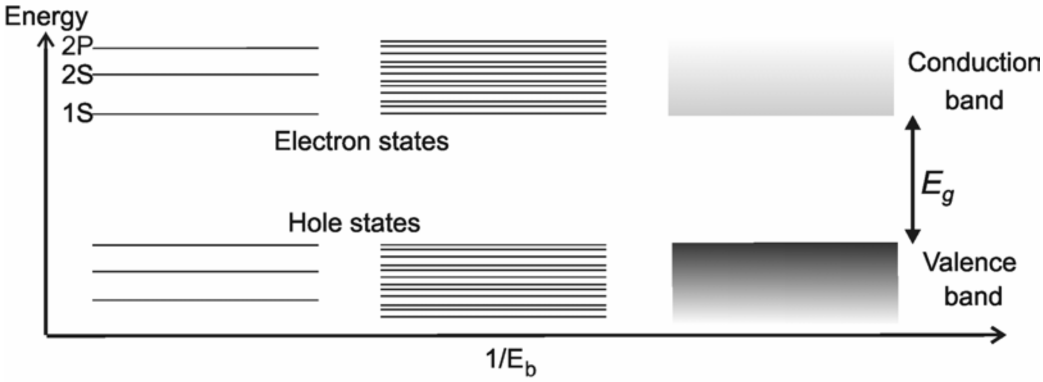

Figure 1.6 Dependence of the exciton energy level spacing on the binding energy of the electron-hole interaction. Strongly bound excitons have large energy spacing. On increasing the electron-hole screening, the energy level density increases until the band structure is recovered.

In nanostructured semiconductors such as quantum dots (QDs), spatial confinement of an electron with its corresponding hole increases their Coulomb binding energy. As such, these materials are highly luminescent, and are finding increasing applications in a new generation of optoelectronic devices, such as in light emitting diodes [9], solar cells [10] and nanocrystal lasers [11]. For very small QDs, the resulting exciton binding energy can be orders of magnitude higher than in the bulk crystal [8], and the energy level spacing is correspondingly larger. It has also been suggested that this large energy spacing (>200 meV, much larger than phonon energies) should slow cooling by hindering the phonon emission process, resulting in a 'phonon bottleneck' in the cooling of hot charges [12]. Such slow cooling would allow hot charge harvesting in solar cells [13]. On the other hand, slow cooling would hinder other applications such as in quantum dot lasers, where rapid cooling is essential [11]. It should be noted, however, that despite the evident technological interest in the carrier cooling process in QDs, its precise rate and mechanism have remained controversial [14]. In chapter 6, the cooling process in quantum dots is investigated as a function of diameter using a combination of ultrafast laser techniques.

1.7 Design of semiconductor devices

The conversion of light into mobile charge carriers, and the reverse process (the conversion of carriers into light), forms the basic operating principle of all modern optoelectronics: electron-hole pair separation may provide a photocurrent, while electron-hole recombination leads to the emission of a photon. For example, a solar cell is designed to convert light energy from the sun into electrical energy. A light emitting diode (LED), on the other hand, converts electricity into light for use in electronic displays etc (see fig 1.7).

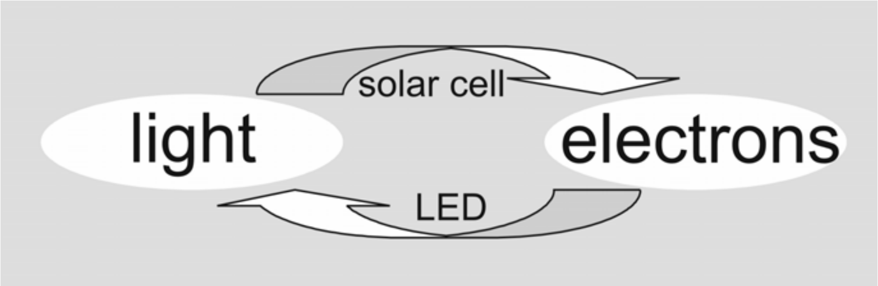

Figure 1.7 The basic operating principle of an optoelectronic device relies on the conversion of light into mobile charges or vice versa: a solar cell converts light into electricity, while an LED converts electricity into light.

The electronic structure of semiconductors facilitates this conversion: absorption of light generates mobile electrons and holes, which can be used to drive an electrical current. The reverse process (the injection of mobile charges into a semiconductor conduction band), can generate light from electrical energy. Clearly, a semiconductor which generates primarily free charges upon photoexcitation is most suited to applications in solar cells, while an excitonic material is most suited to light emission applications, as bound electron-hole pairs have a high radiative recombination probability.

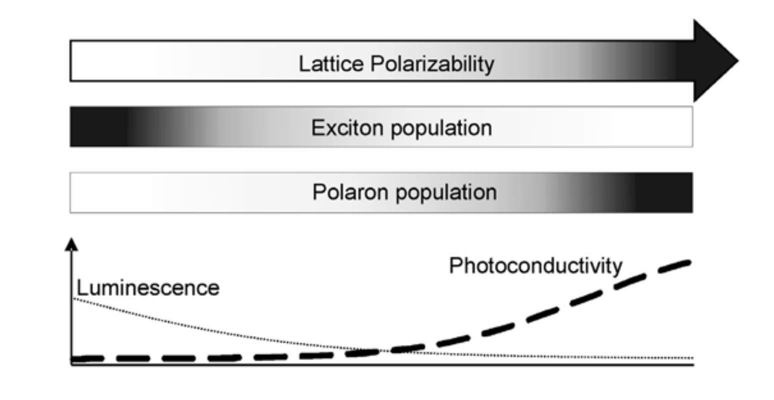

Figure 1.8 Schematic diagram representing the relative probabilities of exciton and polaron formation for increasing lattice polarizability. In non-polarizable materials, insulating excitons are predominantly formed upon photoexcitation, while in polarizable materials polarons are more commonplace. Material properties such as luminescence efficiency and photoconductivity are directly related.

Figure 1.8 shows a simplified picture of these semiconductor properties upon photo-excitation. In non-polarizable semiconductors (i.e. with low dielectric function), exciton formation generally leads to a high luminescence emission, but low conductivity, as excitons cannot support electrical current under an applied static field. More polarizable materials (with high dielectric functions) screen the electron-hole attraction and excitons have much weaker binding energies. This leads to a higher probability of exciting free electrons and holes, and these materials tend have lower luminescence efficiencies and higher photoconductivities. It should be noted that this is a very much simplified overview, and there are many other factors, including band-structure and polaron self-trapping, which can have a drastic influence on luminescence and conductivity in semiconductors and insulators. Indeed, for very polarizable (ionic) materials, polaron formation is known to severely limit the mobility (this effect is discussed in detail for the case of titanium dioxide in chapter 4) and hence the photoconductivity. Furthermore, even a small number of defects in a material may drastically affect conductivity and luminescence properties. Also, the economic costs and the ease of processing can be important factors in the choice of material for electro-optic applications.

The semiconductor most often used in today's devices is silicon. Silicon is a material of intermediate dielectric function, and as such has a reasonably high conductivity, making it suitable in a wide range of electro-optical applications. The purification of silicon, however, is difficult, and the manufacturing of the high purity silicon used in electro-optical devices is expensive. Consequently, there has been much research in the last decade devoted to the engineering of alternative semiconducting materials.

In particular, the efficiency-to-cost ratio of commercial silicon solar cells limits their widespread application [15]. Energy conversion efficiencies of solar cells are limited by the basic properties of the component materials (see figure 1.9):

(a) Incident photons with energy less than the band gap of the semiconductor do not photo-excite mobile charges, and cannot generate any electrical energy.
(b) Excess energy (above band gap) given by incident light generates hot carriers. Rapid cooling (~1 ps in bulk semiconductors [3]) means it is difficult to harvest the carrier energy exceeding the band edge of the semiconductor.
(c) Resistance to the current flow of photo-excited carriers towards the outer electrodes of a cell lowers its power output.

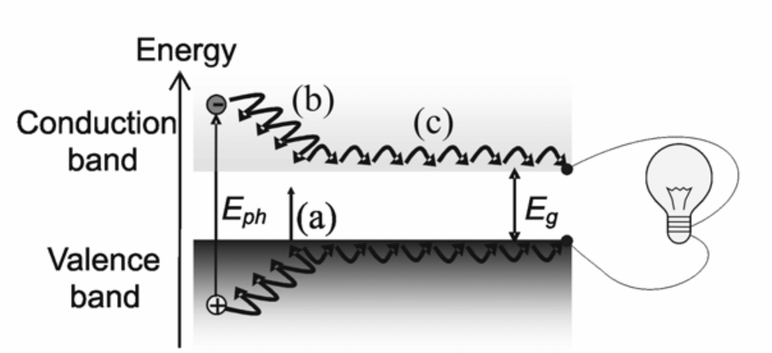

Figure 1.9 Energy loss processes in a solar cell: (a) loss of photons with below band gap energy, (b) cooling of hot carriers and (c) resistance to current flow.

The theoretical limit for the efficiency of photovoltaic cells based on a single band-gap semiconductor (a 1st generation solar cell) is limited by factors (a) and (b) in figure 1.9. As a result, the theoretical solar energy conversion of a single band-gap cell is limited to an efficiency of 33 % (the Shockley-Queisser limit [16]). Step (c) additionally restricts the power output of a working solar cell: transfer of photo-generated electrons and holes towards the outer electrodes of the cell costs extra energy, determined by the internal resistance of the cell.

Despite significant developments over the last few decades, the high cost of material processing necessary to make 1st generation silicon solar cells has remained a limiting factor in the implementation of solar electricity on a large scale [15]. This has fuelled research into possible low cost alternatives. In particular, pioneering work by O'Regan and Grätzel [17] has led to the development of thin film dye sensitized titanium dioxide (TiO_2) solar cells. These cheap, 2nd generation solar cells have only recently started to realize their commercial potential.

Quantum dot solar cells [13] are an example of 3rd generation cell. These cells employ so-called smart design to overcome the Shockley-Queisser efficiency limit of conventional 1st and 2nd generation solar cells. Incorporating QDs as light absorbers, for example, and making use of their size tunable absorption energy as well as the proposed "phonon bottleneck" in cooling, could increase the theoretical efficiency of a QD solar cell to beyond 66% [16]. This is done by restricting the energy loss in the initial stages ((a) and (b) in figure 1.9) after photon absorption.

1.8 Organic conductors and semiconductors

Organic (semi)conductors – i.e. semiconductors based on poly-hydrocarbons – are a fairly recent discovery in materials science. However, since their discovery in the 1970s, these polymers have received considerable interest owing to their potential in technological applications, particularly in electronics [18]. Polymers have many advantages over conventional inorganic conductors and semiconductors: They are low-cost, easy to process, lightweight and malleable, and have shown significant promise in optoelectronics [19] and laser optics [20]. Indeed, organic light emitters are already being used in commercial display technology [21].

In conjugated polymers, a long backbone of alternating single and double bonds between carbon atoms forms a chain, which can be thousands of atoms long. The p_z orbitals of the carbon atoms in such a chain can combine to form delocalized molecular orbitals (see figure 1.10). The energy density of these states (determined by the spacing between the molecular energy levels) is strongly dependent on the number of contributing carbon atoms. For an infinitely long chain of carbon atoms, these discrete energy levels merge to form π (bonding) and π^* (antibonding) bands, separated by an energy gap E_g in the range 1 - 3 eV. However, it should be noted that it is impossible to synthesize long chain polymers without defects. Indeed, even a chemically perfect polymer has thermally excited torsional defects in the carbon-carbon backbone [22]. Hence, the bands in a real polymer are not well defined, and the properties of conjugated polymers are very dependent on *conjugation length* (defined as the average number of continuous defect-free polymer units).

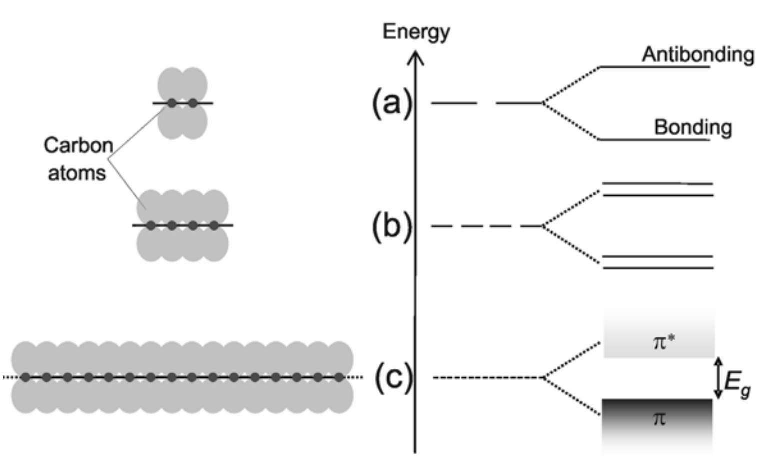

Figure 1.10 Representation of the electronic bonding in a conjugated carbon chain. In a molecule containing two carbon atoms, the p_z orbitals are able to overlap, forming a π-bonding and a π^*-antibonding orbital. For a four carbon chain, the molecular orbitals are more closely spaced, though still discrete. Extending this towards an infinite chain of carbon atoms forms a π-band structure, separated by an energy gap E_g, much like in an inorganic semiconductor such as silicon.

An organic polymeric semiconductor is a conjugated polymer in which all the π electronic states are occupied, and π^* states are empty. There are many similarities to inorganic semiconductors in terms of photophysics: photons with energies greater than the energy gap can be absorbed leading to the population of π^* states, much like the photo occupation of the conduction band in an inorganic semiconductor. As a consequence, these organic semiconductors have many of the properties associated with their inorganic counterparts: due to the delocalization of the π bands, absorption of a light triggers electrical conduction [23] (a property which can be utilized to make polymer solar cells [24]), while charge injection can result in efficient luminescence. Furthermore, the mechanical flexibility of polymeric organic semiconductors has lead to increased application in electro optical devices.

Despite their apparent similarity to inorganic semiconductors, there are, however, obvious differences with conjugated polymers. For example, polaron mobilities in polymer films are orders of magnitude lower than in conventional semiconductors [25]. The DC mobilities in polymer films also increase with temperature [26], while mobilities in inorganic semiconductors tend to decrease with temperature [27, 28].

Despite their obvious technological importance, many of the fundamental aspects of photo-excitation in conjugated polymers remain the subject of intense debate. One of the key remaining questions [29-32] is whether, initially upon photoexcitation, excitons or polarons are primarily formed. In the band picture, excitation with photons of energy greater than the band gap forms a polaron gas, which may subsequently decay to a lower energy exciton state. It has been suggested that a molecular exciton picture [33] is more relevant for polymers. In this model, absorption of a photon generates a hot exciton, which may dissociate into polarons after migration to defects [34], by absorption of a second photon [35] or by bimolecular exciton-exciton annihilation [36]. Whether the band picture or the exciton model is more appropriate to describe photoexcitation processes in polymers depends on the electron-hole binding energy, i.e. whether excitons may be described as Wannier or Frenkel type. Reports of the exciton binding energies in polymers span a huge range, from 20 meV [23, 37] to more that 1 eV [38]. While the observation of significant photoconductivity [23] demonstrates the presence of polarons, it has remained unclear whether carriers are generated directly on ultrafast timescales or produced on longer timescales through exciton dissociation mechanisms. In chapter 7, in order to unravel the charge generation mechanisms at work in these materials, the ultrafast photo-physics in a semiconducting polymer solution are investigated, and compared to those of a thin polymer film.

1.9 This thesis

Many processes which determine the photoconductivity of a material occur on ultrafast (sub) picosecond timescales. Information on this timescale is difficult to access, and much of the current research into charge transport focuses on the time averaged properties. Such steady state measurements give little information about processes actually occurring on fast timescales.

One of the key aspects underlying the application of novel materials in electro-optical devices is the steps immediately following photo-excitation: the cooling, transport and recombination of charge carriers. This thesis presents experimental work investigating ultrafast photo-processes in various technologically relevant materials. By using a combination of femtosecond techniques, photoexcitation and conduction processes are followed in real time, and new insight is gained into fundamental material properties. The goals of this thesis include:

(a) The study and control of carrier relaxation and exciton dynamics in materials.
(b) The determination of the rate and mechanisms of these processes.
(c) The investigation of the role of general material properties such as morphology on excitation and relaxation processes.

The remainder of this thesis is divided into six chapters: chapter 2 deals with the experimental techniques used to investigate ultrafast photoexcitation processes, focusing on the novel technique of THz time domain spectroscopy (THz-TDS). This technique allows the extraction of the complex conductivity spectrum in the THz frequency range with sub-picosecond resolution. Chapter 3 is dedicated to the analysis of THz-TDS spectra. Chapters 4, 5, 6 and 7 present experimental data investigating charge transport in various technologically relevant materials: titanium dioxide (TiO_2) and TiO_2 nanostructures, zinc oxide, cadmium selenide quantum dots, and semiconducting polymers respectively.

References

[1] N. V. Smith, Phys. Rev. B **64**, 155106 (2001).
[2] N. W. Ashcroft and N. D. Mermin, in *Solid State Physics* (Saunders College, 1976).
[3] J. R. Goldman and J. A. Prybyla, Phys. Rev. Lett. **72**, 1364 (1994).
[4] D. Emin, Phys. Rev. B **48**, 13691 (1993).
[5] T. Holstein, Annals of Physics **281**, 706 (2000).
[6] M. G. Calkin and P. J. Nicholson, Rev. Mod. Phys. **39**, 361 (1967).
[7] D. L. Dexter and R. S. Knox, *Excitons* (Interscience Publishers, New York, 1965).
[8] A. L. Efros and M. Rosen, Annu. Rev. Mater. Sci. **30**, 475 (2000).
[9] V. L. Colvin, M. C. Schlamp, and A. P. Alivisatos, Nature **370**, 354 (1994).
[10] W. U. Huynh, J. J. Dittmer, and A.P. Alivisatos, Science **295**, 2425 (2002).
[11] V. I. Klimov, A. A. Mikhailovsky, S. Xu, et al., Science **290**, 314 (2000).
[12] T. Inoshita and H. Sakaki, Phys. Rev. B **46**, 7260 (1992).
[13] V. Aroutiounian, S. Petrosyan, A. Khachatryan, et al., J. Appl. Phys. **89**, 2268 (2001).
[14] A. J. Nozik, Annu. Rev. Phys. Chem. **52**, 193 (2001).
[15] M. Gratzel, Nature **414**, 338 (2001).
[16] A. Luque and A. Marti, phys. Rev. Lett. **78**, 5014 (1997).
[17] B. Oregan and M. Gratzel, Nature **353**, 737 (1991).
[18] M. Angelopoulos, IBM J. Res. Dev. **45**, 57 (2001).
[19] R. H. Friend, R. W. Gymer, A. B. Holmes, et al., Nature **397** (1999).
[20] N. Tessler, G. J. Denton, and R. H. Friend, Nature **382**, 695 (1996).
[21] L. Rothberg, M. Angelopoulos, M. C. Beard, et al., in *SPIE*, edited by Bellingham (WA, WA, 1993), Vol. 1910, p. 122.
[22] F. C. Grozema, P. T. v. Duijnen, Y. A. Berlin, et al., J. Phys. Chem. B **106**, 7791 (2002).
[23] C. H. Lee, G. Yu, and A. J. Heeger, Phys. Rev. B **47**, 15543 (1993).
[24] V. Dyakonov, Appl. Phys. A - Mater. **79**, 21 (2004).
[25] E. Lebedev, T. Dittrich, V. PetrovaKoch, et al., App. Phys. Lett. **71**, 2686 (1997).
[26] P. W. M. Blom, M. J. M. d. Jong, and M. G. v. Munster, Phys. Rev. B **55**, R656 (1997).
[27] J. Shan, F. Wang, E. Knoesel, et al., Phys. Rev. Lett. **90**, 247401 (2003).
[28] E. Yagi, R. R. Hasiguti, and M. Aono, Phys. Rev. B **54**, 7945 (1996).
[29] G. Hadziioannou and P. F. v. Hutten, in *Semiconducting Polymers* (Wiley-VCH, Weinheim, 2000).
[30] A. Kohler, D. A. d. Santos, D. Beljonne, et al., Nature **392**, 903 (1998).
[31] D. Moses, A. Dogariu, and A. J. Heeger, Phys. Rev. B **61**, 9373 (2000).
[32] D. Moses, J. Wang, A. J. Heeger, et al., Synth. Met. **125**, 93 (2001).
[33] V. I. Arkhipov, E. V. Emelianova, and H. Bässler, Phys. Rev. Lett. **82**, 1321 (1999).
[34] B. Dulieu, J. Wery, S. Lefrant, et al., Phys. Rev. B **57**, 9118 (1998).
[35] C. Silva, A. S. Dhoot, D. M. Russell, et al., Phys. Rev. B **64**, 125211 (2001).
[36] G. J. Denton, N. Tessler, N. T. Harrison, et al., Phys. Rev. Lett. **78**, 733 (1997).
[37] C. H. Lee, G. Yu, D. Moses, et al., Phys. Rev. B **49**, 2396 (1994).
[38] M. Chandross, S. Mazumdar, S. Jeglinski, et al., Phys. Rev. B **50**, 14 702 (1994).

Chapter 2

Experimental Techniques

2.1 Why THz?

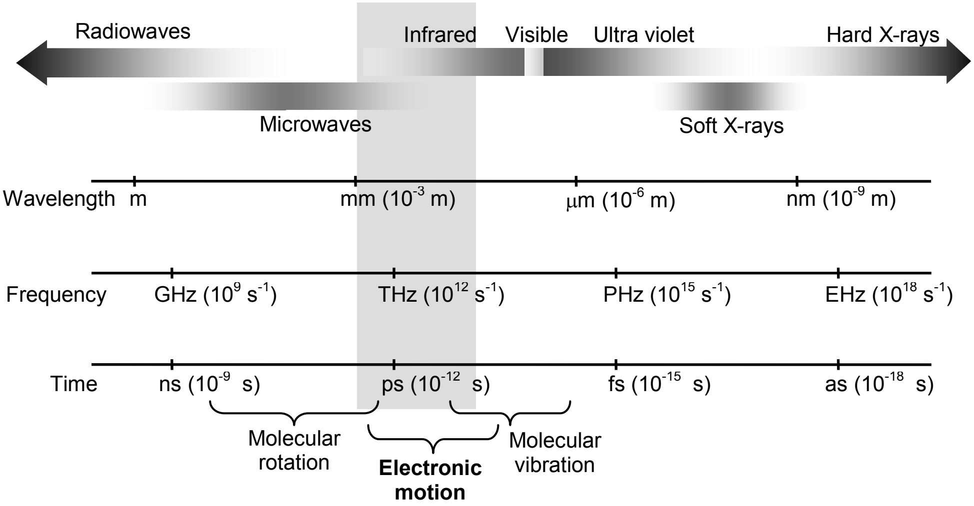

Figure 2.1 The electromagnetic spectrum. Photons in the THz region of the spectrum have wavelengths of the order of 10^{-3} m, frequencies ~10^{12} s^{-1} and oscillation periods ~10^{-12} s. The period corresponds to the typical timescales involved in electron transport (for example, Drude scattering times).

The key factor determining the transport of a Drude charge carrier is its scattering time, the mean time between momentum changing collisions that act to impede the flow of current under an applied electric field. Scattering times typically range from femtoseconds to picoseconds, depending on the precise material. These timescales correspond to the THz frequency range in the electromagnetic spectrum (see figure 2.1). Due to the matching of transport time and field oscillation time, radiation in the THz frequency range interacts in a specific manner with charge carriers, making THz radiation the ideal probe for charge carriers.

As such, THz spectroscopy has proven to be a useful tool in the characterization of charge transport and related phenomena [1-5]. By probing the frequency dependence of a material's conductivity in the THz range, useful information can be obtained about charge mobility, charge mass and scattering time [2, 3, 5]. In polarizable materials, information concerning the polaron binding energy, mass increase and lattice coupling constant can also be determined [5]. In less polarizable materials, the drastically different THz response of excitons to that of free charge carriers and polarons can be a useful tool in distinguishing and probing different species [4].

To investigate photoconductivity, we combine THz radiation with a visible pump pulse (to excite, for example, mobile electrons into the conduction band of a semiconductor). By using pulsed radiation for both the visible pump and the THz probe, valuable information can be obtained about the dynamics of photoconductivity. The scheme of such an experiment is represented in figure 2.2. A sample is photo-excited by an optical pump, upon which charge carriers are created. By delaying the THz probe pulse with respect to the pump pulse, the dynamics of carrier cooling, transport, trapping and decay processes can be followed in real-time.

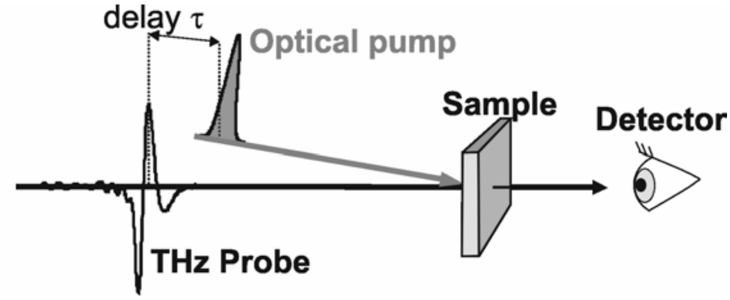

Figure 2.2 Schematic diagram of time-resolved THz experiments: a sample is photo-excited by an optical pump, upon which charge carriers are created. By delaying the THz probe pulse with respect to the pump pulse, the dynamics of cooling can be followed in real-time, as well as the subsequent trapping and decay processes.

2.2 THz time domain spectroscopy (THz-TDS)

The THz frequency range is in-between electronically attainable frequencies and optical frequencies, making it a difficult to generate and detect experimentally. Since the development of ultrafast lasers, this frequency range has become more accessible. In particular, THz time domain spectroscopy (THz-TDS) has emerged as a powerful optical probe of charge transport in condensed matter [1-5]. THz-TDS provides a contact-free (i.e. not requiring electrodes) approach to determine the complex conductivity of materials over a wide frequency range (0.1-2 THz; 3-70 cm^{-1}; 0.4-8 meV). The sub-picosecond time resolution allows the dynamics of generation, cooling and decay processes to be followed in real time.

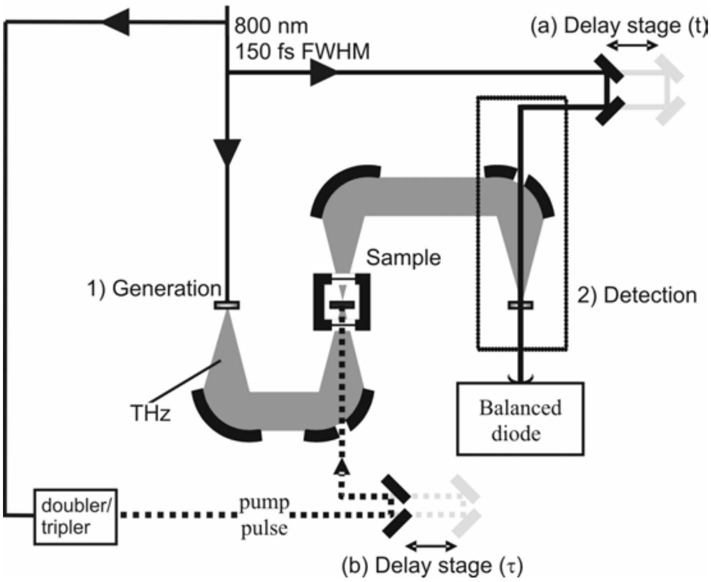

Figure 2.3 The THz spectrometer: 1) generation of THz occurs in a ZnTe crystal through optical rectification. Generated THz pulses are first collimated and then focused onto a sample using off-axis parabolic mirrors. The sample can be housed in a closed cycle helium cryostat for temperature control. Transmitted THz pulses are re-collimated and focused onto a detection crystal. 2) THz field waveforms are detected through electro-optical sampling in a second ZnTe crystal by scanning the temporally narrow 800 nm pulse over the THz field using delay stage (a). A pump pulse can be used to excite the sample at a negative delay τ using delay stage (b).

The typical experimental set-up used in a THz-TDS experiment is plotted in figure 2.3. The laser system used to run the spectrometer is based on a Coherent Legend regenerative amplifier (Regen) seeded by a Coherent Verdi (790 nm central wavelength, 120 fs temporal intensity FWHM, 80 MHz repetition rate, 500 mW output power) and pumped by Coherent Evolution (527 nm central wavelength, 20 ns temporal FWHM, 1 kHz repetition rate, 23 W output power). The amplified output of the Regen intensity is centered around 800 nm, has a temporal FWHM 150 fs (corresponding to 5.5 THz FWHM in the spectral domain) and a 1 kHz repetition rate. Of the 2.5 W output power of the Regen, 90 mW is used to run the spectrometer.

Generation of THz radiation occurs in a phase-matched manner in a zinc telluride (ZnTe) crystal (<110> orientation, size 10×10×1.2 mm thickness, from MarkeTech) through optical rectification [6] using 80 mW of the Regen output. The Regen output is weakly focused by lens (50 cm focal length) onto the generation crystal to a ~3 mm diameter spot size. Generated THz pulses are first collimated and then focused onto a sample using a pair of rhodium-coated off-axis parabolic mirrors from Melles Griot (6.7 cm focal length, 5.7 cm diameter aperture centered along the mechanical axis). The sample can be housed in a closed cycle helium cryostat (Air Products) for temperature control (10-300 K). Transmitted THz pulses are re-collimated and focused onto a second ZnTe detection crystal (also <110> orientation) using a second pair of paraboloids.

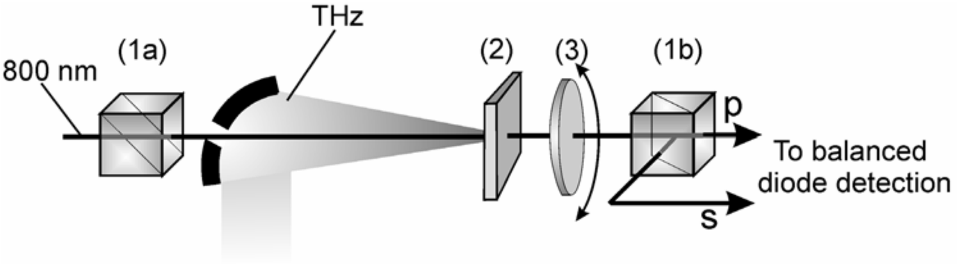

Figure 2.4 THz detection scheme (dotted box in figure 2.3): the THz field strength is measured using electro-optical sampling. The polarization of the femtosecond 800 nm pulse is cleaned using a cube polarizer (1a). The femtosecond pulse is then spatially overlapped with the imaged THz spot onto a birefringent ZnTe crystal (10×10×1.2 mm, <110> orientation). The electro-optic effect causes rotation of the femtosecond pulse polarization in the presence of the THz field. Using a polarizer (1b), oriented perpendicular to (1a), the pulse is split into s and p polarizations. The intensities of these two beams are balanced in the absence of a THz field using a quarter wave plate (3).

The field strength of the THz field imaged onto the sampling crystal is detected through electro-optical sampling [7] using 5 mW of the Regen output, weakly focused using a 2 m focal length lens to a ~1 mm diameter spot size centered on the THz focus (~3 mm). Electro-optical sampling utilizes the considerable electro-optical activity of ZnTe (the perturbation of the material's refractive index by an externally applied field): the THz field induces a small birefringence in the ZnTe crystal which can be probed using the femtosecond 800 nm laser pulses. Since the THz pulses are significantly longer than the laser pulses (several ps compared to 150 fs), the THz field can be approximated as a static field biasing the detection crystal. On passing through such a crystal, the initially linearly polarized 800 nm pulse becomes elliptically polarized, the initial linear polarization and crystal angle optimized for maximum ellipticity [7]. The ellipticity of transmitted detection pulses can be determined using crossed polarizers (1a and 1b in figure 2.4). A quarter wave plate is used to balance the s and p polarized outputs of 1b in the absence of the THz field, and the intensity difference is tracked using balanced diodes. The magnitude and sign of the ellipticity induced when the THz field is applied is recorded as a change in the intensity of s and p polarizations of the detection pulses. For perturbatively small modulations, the intensity change is linear with the applied THz field strength [7], and the output signal of the detector is proportional to the magnitude and the sign of the field of the THz pulse at each time defined by the arrival of the probe pulse. The magnitude of the electro-optic signal can be calibrated by applying a static field across the detection crystal in the absence of any THz field. Hence, by varying the delay (*t*) between THz and 800 nm probe pulses the temporal profile of the detected THz field, $E_{free}(t)$, can be obtained. This “gating” technique allows a time resolution better than the THz pulse duration [8], permitting the study of the conductivity in materials with sub-picosecond temporal resolution, and the probing of ultrafast excitation processes real time. Typical measurements of the THz electric field waveform are plotted (full lines) in figure 2.5. These have been measured in dry nitrogen, removing water absorptions from the spectrum.

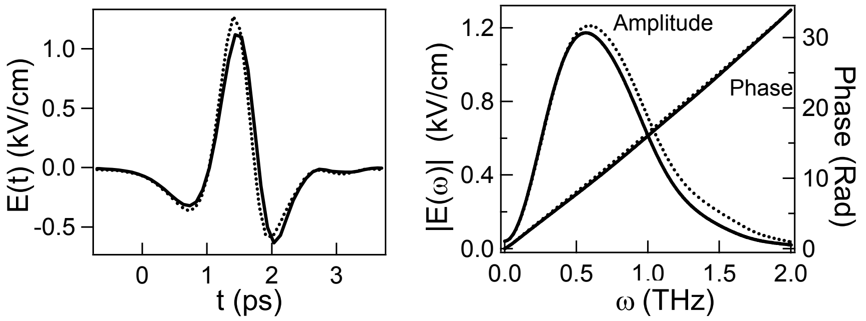

Figure 2.5 Left: (full lines) typical THz waveforms $E_{free}(t)$ – measured without sample – using electro-optical detection. Right: the Fourier transform contains both amplitude and phase information. Dotted lines: THz field strength incident on the detector, taking into account the detector response function (see section 2.3).

The THz pulses are essentially single cycle oscillations of an electric field, with a period of ~1 ps and peak electric field ~1 kV/cm. The direct measurement of the electric field strength in the time domain allows the determination of both amplitude and phase. This is in contrast to conventional transient-absorption studies, in which generally only the spectrally integrated intensity of the probe beam is recorded. Fourier transforming into the frequency domain yields the spectrum of the pulse, the resolution of which is determined by the length of the time domain measurement (i.e. the length scanned by delay stage (a) in figure 2.3). The measurement of both the amplitude *and* phase allows simultaneous extraction of both the real *and* imaginary components of the complex conductivity of a sample (see chapter 3) without the need for Kramers-Kronig analysis, in the frequency range from 0.2 to 2 THz. It should be noted that these <1 kV/cm fields are much lower than the MV/cm fields typically used in devices, so that our THz pulse acts as a true probe pulse, not perturbing the system.

In order to study changes in photoconductivity a pump pulse can be introduced to excite the sample at a time τ preceding the THz pulse, using delay stage (b) in figure 2.3. The variation of this delay allows the photoexcitation dynamics to be followed. Doubling and tripling the remaining Regen output (i.e. that not used in the THz spectrometer), allows the excitation wavelength to be set to either 800 nm (1.55 eV), 400 nm (3.10 eV) or 266 nm (4.66 eV) with excitation powers 0-800 mW, 0-300 mW or 0-80 mW respectively. Care is taken to ensure homogenous excitation of the THz pulse imaged onto the sample. The signal to noise is enhanced by chopping the excitation pulse and detecting at this frequency using a lock-in amplifier, the read out of which (as well as the control of the detection pulse delay) is controlled by a personal computer. In this way, and using signal averaging, photo-induced delays of the transmitted THz pulse as small as 20 attoseconds (20×10^{-18} s) can be recorded.

2.3 System response function

The propagation of the THz field through the electro-optic sensor used in the experiments causes a distortion of the waveform. This can lead to a different detected waveform $E_{free}(t)$ from that incident on the detector $E_{free}^{inc}(t)$. In some experiments, this must be taken into account in the extraction of conductivity (see chapter 3).

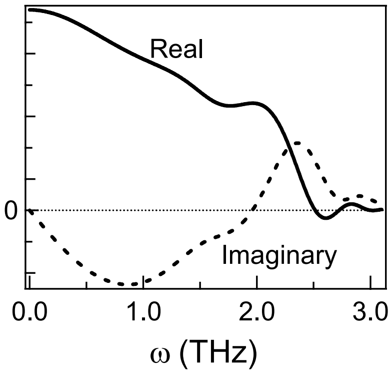

Figure 2.6 Real and imaginary parts of the detector response function $f(\omega)$ which distorts the incident THz waveform on propagation through the detector. The detected waveform is related to the incident field through equation 2.1.

The Fourier transform of the detected waveform $E_{free}(\omega)$, is related to the electric field incident on the detector $E_{free}^{inc}(t)$, through the detector response function $f(\omega)$, such that:

$$E_{free}(\omega) = f_{\det}(\omega) E_{free}^{inc}(\omega) \tag{2.1}$$

Gallot and Grischkowsky [9] have analyzed the distortion of THz pulses during electro-optic sampling and found:

$$f_{\det}(\omega) = \left[\int_{-\infty}^{+\infty} E_{opt}^{*}(\omega')E_{opt}(\omega'-\omega)d\omega' \right] \times \chi_{dif}^{(2)}(\omega) \times \frac{\exp\left(\frac{i\omega l_{\det}}{c}\Delta n(\omega) \right) - 1}{\frac{i\omega l_{det}}{c}\Delta n(\omega)}. \tag{2.2}$$

The first term is the frequency domain autocorrelation of the 800 nm detection pulse. The second is the second order susceptibility for difference frequency generation at 800 nm taken from ref. [9]. The final, and dominant, term describes the velocity matching of the 800 nm detection pulse and the THz frequency, ω, required for efficient detection in the ZnTe crystal of length l_{det}=1.2 mm, where $\Delta n(\omega)$ is the difference between the complex, frequency-dependent THz refractive index and the refractive index corresponding to the *group* velocity of the 800 nm pulse. The THz refractive index has been measured by Gallot *et al.* [9], while the group index at 800 nm in ZnTe has been evaluated by Bakker *et al.* [10] to be 3.24. The complex detector response function has been plotted in figure 2.6 for these values. By measuring the THz waveform using the electro-optical detector, the waveform before propagation can be obtained using equations (2.1) and (2.2) – plotted as dotted lines in figure 2.5.

2.4 A typical THz-TDS experiment

The goal of a THz-TDS experiment is to measure the response of a sample to the probe. This response to the THz field can be described in terms of the material refractive index (n_{sample}), relative dielectric function (ε_{sample}) or conductivity (σ_{sample}), all of which contain equivalent information. These complex parameters are related through

$$n_{sample}^{2} = \varepsilon_{sample}, \tag{2.3}$$

$$\sigma_{sample} = \text{-i}\omega\varepsilon_{sample}\varepsilon_{0}, \tag{2.4}$$

where ε_0 is the vacuum permittivity.

A typical THz-TDS experiment involves the measurement of the transmitted THz field in three circumstances: transmitted with no sample $E_{free}(t)$, through the unexcited sample $E_{trans}(t)$ and through the sample at time τ after photo-excitation $E_{trans}^{exc}(t,\tau)$ – see figure 2.7. $E_{free}(t)$ and $E_{trans}(t)$ are related to the response of the unexcited sample. To avoid confusion, this response is represented throughout this thesis by the (complex) lattice dielectric function ε. $E_{trans}(t)$ and $E_{trans}^{exc}(t,\tau)$ depend on the *modified* response due to the photoexcitation, described here by the photoconductivity σ. Since the measurements contain both amplitude *and* phase information, ε and σ extracted from the data contain both real *and* imaginary parts (see chapter 3). In this thesis, the dielectric function will be presented in its relative form (i.e. $\varepsilon=\varepsilon_{abs}/\varepsilon_0$, where ε_{abs} is the absolute value in SI units) and photoconductivity in SI units of Siemens per meter (S/m).

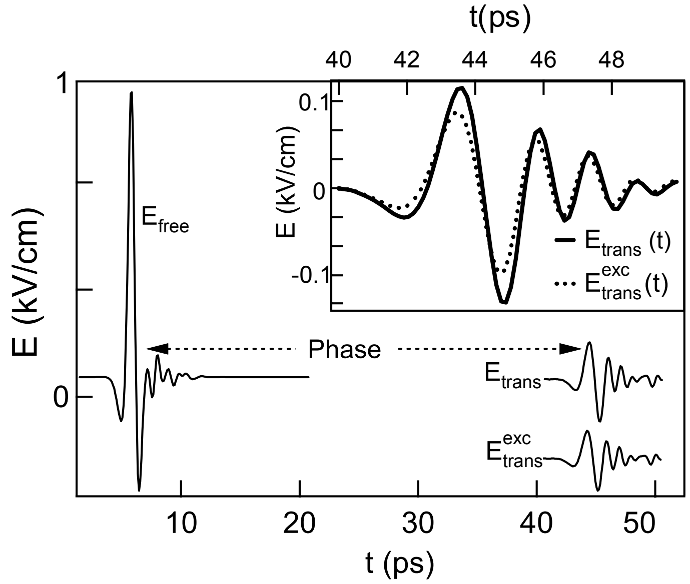

Figure 2.7 Three THz-scans measured in a typical THz-TDS experiment: The pulse transmitted through air (or nitrogen) with no sample $E_{free}(t)$, through the unexcited sample $E_{trans}(t)$ and through the photo-excited sample $E_{trans}^{exc}(t)$. The scans contain both amplitude (absorption) and phase (refraction) information. Inset: $E_{trans}^{exc}(t)$ has a distinctly different shape from $E_{trans}(t)$, providing us with the phase and amplitude information required to extract the real and imaginary parts of the complex photoconductivity.

2.5 THz emission spectroscopy

As several dynamic processes may occur directly following photoexcitation, carrier properties on ultrafast timescales can be very different from the equilibrium behavior of a material. Conventional transient photoconductivity measurements [11, 12] lack the resolution to resolve ultrafast excitation processes. In these experiments, a static electric field is applied to the sample and the resulting electrical current on photoexcitation is measured. An alternative to measuring the generated photocurrent is to probe the radiation dispersed by the accelerating charges [13, 14]. This emission is in the THz frequency range when changes in photocurrent occur on (sub)-picosecond timescales. The temporal profile of the emitted THz pulse is determined by the rise and decay of the photocurrent [13], and thus provides a direct probe of the ultrafast transient photoconductivity. Hence, THz emission spectroscopy is complimentary to other ultrafast measurements such as THz-TDS.

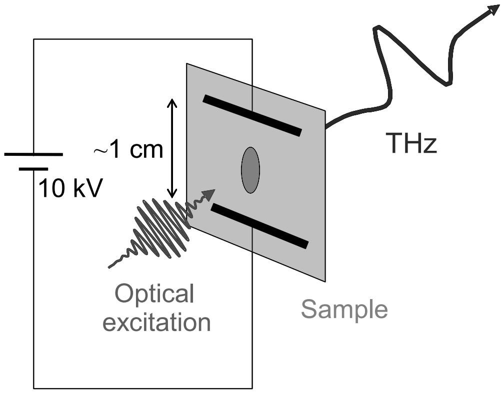

Figure 2.8 The concept of THz emission spectroscopy: the sample is excited with a femtosecond visible pulse, and mobile photo-charges are accelerated by an applied DC field. The emitted THz radiation is detected in the far field using electro-optical sampling.

The concept of THz emission spectroscopy is represented in figure 2.8: the sample is excited with a femtosecond visible pulse, and mobile photo-charges are accelerated by an applied DC (direct current, 10 ns pulses at 1 kHz) electric field. The emitted THz radiation is detected in the far field (>1 cm) using electro-optical sampling. In this manner, information regarding the rate of charge carrier generation and time-dependent mobility can be obtained. This technique is ideally suited to the study of charge generation and cooling on sub-picosecond timescales, and has been successfully applied to study the photoexcitation dynamics in materials such as low temperature grown GaAs [13].

2.6 Transient absorption and time resolved luminescence

One of the aims of this thesis is to combine THz-TDS with more common ultrafast optical techniques, allowing a more complete characterization of sample properties. Two of these techniques, femtosecond transient absorption and luminescence up-conversion, are represented in figure 2.9. Both these experiments make use of similar 800 nm femtosecond pulses.

Femtosecond transient absorption is probably the most commonly used ultrafast technique for characterizing photoexcitation properties of novel materials, particularly for conjugated polymers [15-19]. This technique uses light with frequencies in the visible region of the electromagnetic spectrum to probe transient spectral changes after photoexcitation. Transient absorption measurements can be very useful in identifying different photo-excited species due to their distinct absorption features in the transient spectra. The drawback of such measurements is that the transient spectra tend to be very complicated and difficult to interpret [18, 19], and absorption features in a transient spectrum are often assigned to very different species [16, 17]. Transient absorption measurements presented in this thesis are limited to the 800 nm probe pulses.

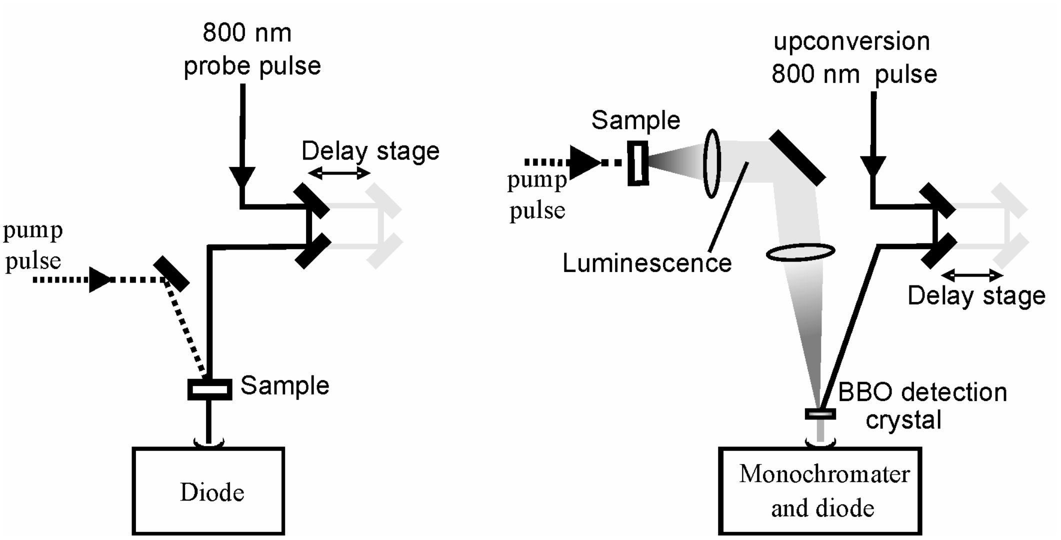

Figure 2.9 Left: transient absorption with 800 nm. The sample is excited with a pump pulse, and then probed at different times after excitation by an 800 nm probe pulse. Right: luminescence up-conversion. The sample is again excited by a pump pulse, and the resulting luminescence is gathered and focused onto a phase matched BBO crystal. The luminescence at different times after excitation is then up-converted by an 800 nm pulse, and the frequency mixed pulse is passed through a monochrometer (to allow frequency selection) and detected by a diode.

Luminescence up-conversion probes the luminescence emitted by a sample after photoexcitation by a femtosecond excitation pulse. The up-conversion technique has much higher time resolution compared to other luminescence measurements, allowing the investigation of ultrafast dynamics [20]. The disadvantage of luminescence techniques is that they are only sensitive to luminescent species (i.e. excitons). This makes it difficult to extract information about charge carrier density and mobility, as well as carrier cooling. The luminescence up-conversion measurements presented in this thesis were carried out in the lab of Dr. Hong Zhang, in the Chemistry Department of the University of Amsterdam. The experimental set-up is described in more detail in ref. [21].

References

[1] M. C. Beard, G. M. Turner, and C. A. Schmuttenmaer, J. Phys. Chem. B **106**, 7146 (2002).
[2] E. Knoesel, M. Bonn, J. Shan, et al., Phys. Rev. Lett. **86**, 340 (2001).
[3] J. Shan, F. Wang, E. Knoesel, et al., Phys. Rev. Lett. **90**, 247401 (2003).
[4] E. Hendry, J. M. Schins, L. P. Candeias, et al., Phys. Rev. Lett. **92**, 196601 (2004).
[5] E. Hendry, F. Wang, J. Shan, et al., Phys. Rev. B **69**, 081101 (2004).
[6] X. C. Zang, Y. Jin, and X. F. Ma, App. Phys. Lett. **61**, 2764 (1992).
[7] P. C. M. Planken, H. K. Nienhuys, H. J. Bakker, et al., J. Opt. Soc. Am. B **18**, 313 (2001).
[8] P. Jepsen, et al., App. Phys. Lett. **79**, 1291 (2001).
[9] G. Gallot and D. Grischkowsky, J. Opt. Soc. Am. B **16**, 1204 (1999).
[10] H. J. Bakker, G. C. Cho, H. Kurz, et al., J. Opt. Soc. Am. B **15**, 1795 (1998).
[11] C. H. Lee, G. Yu, D. Moses, et al., Phys. Rev. B **49**, 2396 (1994).
[12] D. Moses, H. Okumoto, C. H. Lee, et al., Phys. Rev. B **54**, 4748 (1996).
[13] H. Nemec, A. Pashkin, P. Kuzel, et al., J. Appl. Phys. **90**, 1303 (2001).
[14] C. Soci and D. Moses, Synth. Met. **139**, 815 (2003).
[15] M. Yan, L. G. Rothberg, F. Papadimitrakopoulos, et al., Phys. Rev. Lett. **72**, 1104 (1994).
[16] B. Kraabel, D. McBranch, N. S. Sariciftci, et al., Phys. Rev. B **50**, 18543 (1994).
[17] S. Stagira, M. Nisoli, G. Lanzani, et al., Phys. Rev. B **64**, 205205 (2001).
[18] V. I. Klimov and D. W. McBranch, Phys. Rev. Lett. **80**, 4028 (1998).
[19] V. I. Klimov, A. A. Mikhailovsky, D. W. McBranch, et al., Phys. Rev. B **61**, R13349 (2000).
[20] D. F. Underwood, T. Kippeny, and S. J. Rosenthal, J. Phys. Chem. B **105**, 436 (2001).
[21] P. van der Meulen, H. Zhang, A. M. Jonkman, et al., Journal Of Physical Chemistry **100**, 5367 (1996).

Chapter 3

Analysis of THz-TDS measurements

3.1 Objective of a THz-TDS experiment

In a THz-TDS experiment, a pulse of THz radiation passes through a sample and has its time profile changed compared to that of a reference pulse. Through analysis of the spectral changes of the pulse introduced by the sample, the frequency dependent response of the material can be obtained. This response can be equivalently described in terms of complex refractive index, dielectric function or conductivity (see section 2.4). In this thesis, in order to avoid confusion, the response of the unexcited sample is described in terms of its dielectric function ε, while the change in response on photoexcitation is described in terms of photoconductivity σ. In this thesis, the dielectric function will be presented in its relative form (i.e. $\varepsilon=\varepsilon_{abs}/\varepsilon_0$, where ε_{abs} is the absolute value in SI units) and photoconductivity in SI units of Siemens per meter (S/m).

3.2 Extraction of the sample dielectric function

A typical set of THz measurements involves measuring the THz field transmission under three conditions – with no sample ($E_{free}(t)$), the unexcited sample ($E_{trans}(t)$), and with the photo-excited sample ($E_{trans}^{exc}(t)$). Data analysis is most conveniently performed in the frequency domain using the corresponding Fourier transforms of the time domain data: $E_{free}(\omega)$, $E_{trans}(\omega)$ and $E_{trans}^{exc}(\omega)$. The first two measurements contain information about the response of the unexcited sample, described in terms of its dielectric function $\varepsilon(\omega)$.

In general, the transmission of an electric field through a homogenous region described by dielectric function ε_j and length l_j (see figure 3.1) can be written as:

$$E_{j+1}(\omega)=\rho_j(\varepsilon_{j-1},\varepsilon_j,\varepsilon_{j+1},l_j)E_{j-1}(\omega), \tag{3.1}$$

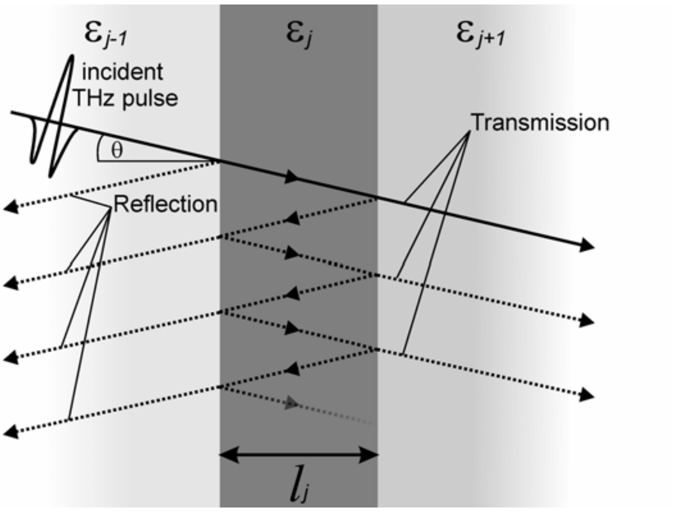

Figure 3.1 Transmission of a THz pulse through a homogeneous region described by dielectric function $\varepsilon_j(\omega)$ and length l_j. In the experiment, THz pulses can be approximated as plane waves incident along the surface normal (i.e. θ=0). The total transmission is determined by direct transmission and contributions from multiple reflections (dotted lines) within the homogeneous region.

where ε_{j-1} and ε_{j+1} describe the dielectric function before and after the region respectively. Here, ρ_j defines the transmission function through the region in question. Since the THz pulses used in the experiment are reasonably described as plane waves at normal incidence (i.e. θ=0 in figure 3.1), it can be shown using Maxwell's equations that the transmission function through a dielectric slab of thickness l_j, summing over an infinite number of multiple reflections, has the simple form [1]:

$$\rho_j(\varepsilon_{j-1},\varepsilon_j,\varepsilon_{j+1},l_j)=\frac{T(\varepsilon_{j-1},\varepsilon_j)T(\varepsilon_j,\varepsilon_{j+1})e^{i(\sqrt{\varepsilon_j})\omega l_j/c}}{1+R(\varepsilon_{j-1},\varepsilon_j)R(\varepsilon_j,\varepsilon_{j+1})e^{2i(\sqrt{\varepsilon_j})\omega l_j/c}}, \tag{3.2}$$

where the interfacial Fresnel transmission and reflection coefficients for normal incidence have the form:

$$T(\varepsilon_j,\varepsilon_{j+1})=\frac{2\sqrt{\varepsilon_j}}{\sqrt{\varepsilon_j}+\sqrt{\varepsilon_{j+1}}},R(\varepsilon_j,\varepsilon_{j+1})=\frac{\sqrt{\varepsilon_{j+1}}-\sqrt{\varepsilon_j}}{\sqrt{\varepsilon_{j+1}}+\sqrt{\varepsilon_j}}. \tag{3.3}$$

The transmission through a homogeneous sample of dielectric function $\varepsilon(\omega)$ and length L surrounded by air or vacuum simplifies to:

$$E_{trans}(\omega)=\rho(1,\varepsilon,1,L)E_{free}(\omega)e^{-i\omega L/c} \tag{3.4}$$

Since the measurements contain information about *both* the relative amplitude and phase of E_{trans} with respect to E_{free}, the complex transmission function ρ can be solved iteratively for the *both* real and imaginary parts of sample dielectric function $\varepsilon(\omega)$.

3.3 Pump-probe THz-TDS

THz-TDS pump-probe experiments are in some respects similar to pump-probe experiments with visible light: a visible-light pump pulse creates an excitation in a sample, which is probed with a second pulse at a time τ after the excitation (see figure 2.3). The strength of THz-TDS lies in the distinctive detection technique [2, 3]: not only the change in absorbance on photoexcitation is determined, but also the phase shift of all frequency components contained in the probe field. This information is best expressed in terms of the complex photoconductivity spectrum $\sigma(\omega, \tau)= \sigma'(\omega, \tau)+i\sigma''(\omega, \tau)$, which depends explicitly on time τ after photoexcitation. In principle, the experimentally-determined absorption and phase shift of the THz field are fully determined by $\sigma(\omega, \tau)$ [4].

3.4 The steady state approximation

If the variations in the sample response due to photoexcitation occur on a timescale that is slow compared the FWHM of the THz probe pulse (~1 ps), the leading edge of the THz pulse probes the same material properties as the trailing edge, and a quasi-steady state approximation, in which the transmitted field is not explicitly dependent on τ, is valid. In this case, $E_{trans}(\omega)$ and $E_{trans}^{exc}(\omega)$ can be analyzed in a manner similar to that presented in the previous section to extract the photoconductivity $\sigma(\omega)$ at time τ. For spatially homogeneous excitation (i.e. when the sample is homogeneously excited along the direction of the THz pulse propagation) the analysis is straightforward and reduces to:

$$E_{trans}^{exc}(\omega) = \rho(1, \varepsilon + \frac{i\sigma}{\omega\varepsilon_0}, 1, L)\frac{E_{trans}(\omega)}{\rho(1, \varepsilon, 1, L)}. \tag{3.5}$$

Hence, with the transmission through the excited (E_{trans}^{exc}) and unexcited (E_{trans}) sample, coupled with prior knowledge of the ground state dielectric function (ε) – which can be independently determined as described in section 3.2 – it is straightforward to iteratively solve equation 3.5 to obtain the quasi-steady state conductivity $\sigma(\omega)$.

The data analysis becomes more complicated in the case of spatially inhomogeneous excitation, i.e. when the sample is inhomogeneously excited along the direction of the THz pulse propagation. This occurs, for example, for an excitation process involving linear (one-photon) absorption characterized by a penetration depth l_0 of the excitation light smaller than the sample thickness L. In that case, the excitation density N decays in the propagation direction *z* by $N(z) = N_0 e^{-z/l_0}$ – shown by the dotted line in figure 3.2. The distance l_0 can be inferred from the visible absorption spectrum [5] or, equivalently, from the refractive index or dielectric function [6]. While the case of an exponential dependence is discussed in the following text, it should be noted that a similar analysis can be carried out for any known spatially varying density.

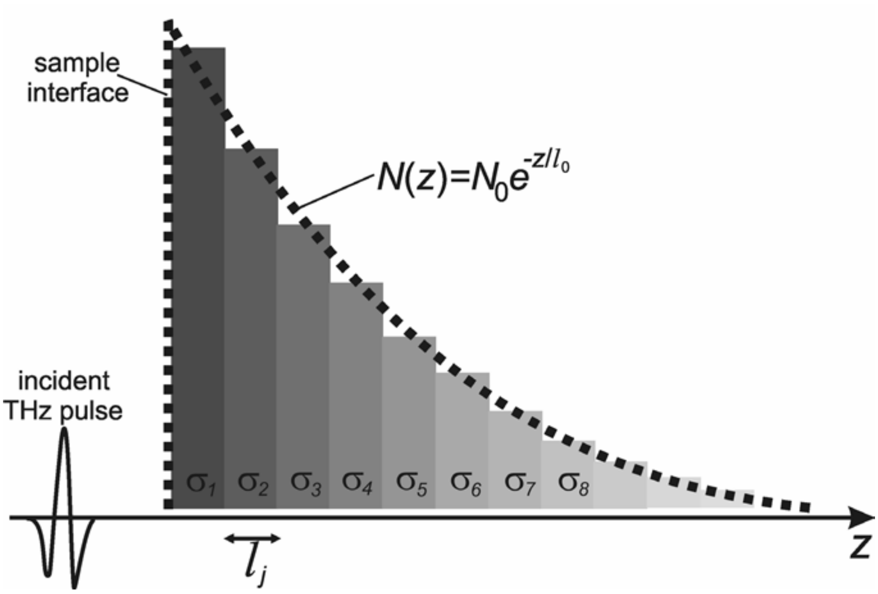

Figure 3.2 Spatial dependence of excitation density (dotted line) in the THz propagation direction *z* for linear absorption. The decay of the conductivity can be approximated by a series of homogeneous slabs of thickness l_j.

If the excitation density is low enough, particle-particle interactions can be neglected and the conductivity is simply proportional to density (see equation 1.4). In this density regime, the conductivity has a simple parametric dependence on *z*. For example, for one-photo absorption:

$$\sigma(\omega, z) = \sigma_0(\omega) e^{-z/l_0}, \tag{3.6}$$

where σ_0 is the conductivity at the sample interface. By splitting the excitation region into a number N_{slabs} of homogeneous slabs with thickness δl that is small compared to l_0, and approximating the smooth spatial decay of the conductivity by the discrete series $\sigma_j(\omega)$ – see figure 3.2 – we can analyze the transmission through the excitation region by calculating the transmission from one slab to the next and evaluating the entire sequence:

$$\begin{aligned}
E_{trans}^{exc}(\omega) = {} & \rho_1\left(1,\varepsilon+\frac{i\sigma_1}{\omega\varepsilon_0},\varepsilon+\frac{i\sigma_2}{\omega\varepsilon_0},\delta l\right) \\
& \times \prod_{j=2}^{N_{slabs}-1} \frac{\rho_j\left(\varepsilon+\frac{i\sigma_{j-1}}{\omega\varepsilon_0},\varepsilon+\frac{i\sigma_j}{\omega\varepsilon_0},\varepsilon+\frac{i\sigma_{j+1}}{\omega\varepsilon_0},\delta l\right)}{T_{j-1}\left(\varepsilon+\frac{i\sigma_{j-1}}{\omega\varepsilon_0},\varepsilon+\frac{i\sigma_j}{\omega\varepsilon_0}\right)} \\
& \times \frac{\rho_{N_{slabs}}\left(\varepsilon+\frac{i\sigma_{N_{slabs}-1}}{\omega\varepsilon_0},\varepsilon+\frac{i\sigma_{N_{slabs}}}{\omega\varepsilon_0},1,\delta l\right)}{T_{N_{slabs}-1}\left(\varepsilon+\frac{i\sigma_{N_{slabs}-1}}{\omega\varepsilon_0},\varepsilon+\frac{i\sigma_{N_{slabs}}}{\omega\varepsilon_0}\right)} \\
& \times \frac{E_{trans}(\omega)}{\rho(1,\varepsilon,1,L)}.
\end{aligned} \tag{3.7}$$

In numerical analysis, care is taken to ensure that the number of slabs N_{slabs} is sufficiently large so that the extracted response is independent of the number chosen. Hence, coupled with knowledge of the excitation penetration depth l_0 and sample dielectric function ε, the complex conductivity σ can be extracted from the measurements E_{trans}^{exc} and E_{trans} using equation 3.7.

A consequence of this extensive analysis is the extracted conductivities σ are a varying function of spatial coordinate z. For a meaningful comparison between different measurements, we discuss the conductivity at the sample interface σ_0. This quantity allows for a convenient and meaningful comparison between the conductivities in two samples with very different penetration depths and/or absorption properties.

Due to uncertainties in the experimental excitation fluences and absorption coefficients, it should be noted that the spatial decay of the excitation density assumed in the extraction of the conductivity is somewhat approximate. Furthermore, this analysis neglects effects of charge diffusion in-between excitation and the arrival of the THz probe. This can be a severe approximation when extracting the conductivity of a sample for longer pump-probe times τ, or when the penetration depth l_0 is much smaller than the mean free path of the excited charges l_r. The characteristic distance of the spatial distribution of charge in the sample is then given by $\sim \sqrt{D\tau}$, for a diffusion coefficient D. This effect will be discussed in more detail, where appropriate, later in the text.

The uncertainty in the charge distribution in the sample introduces errors in the *absolute* values of the extracted interface conductivities. However, since we measure the THz wave transmitted through the entire excited region (and the modulation of the THz is essentially proportional to the product of density *and* penetration depth), the relative error (i.e. in the ratio of two measured conductivities) is small. Comparison *between* measured conductivities is therefore still possible.

3.5 Non-steady state conditions

The steady-state approach in the previous section is not valid if the properties of the sample change rapidly, for example during the excitation by the pump pulse, when the charge carriers exhibit fast trapping or recombination dynamics, or when the response of charges is time-dependent as a result of, for instance, carrier cooling [7-9]. Here, one would like to extract a time-dependent conductivity spectrum $\sigma(\omega, \tau)$ [4]. The extraction of this quantity that is varying both with frequency and pump-probe time is not trivial, as will be shown in the next section. In these transient experiments it is useful to define an absorption induced modulation of the transmitted THz field:

$$\Delta E_{trans}(t,\tau) = E_{trans}^{exc}(t,\tau) - E_{trans}(t) \tag{3.8}$$

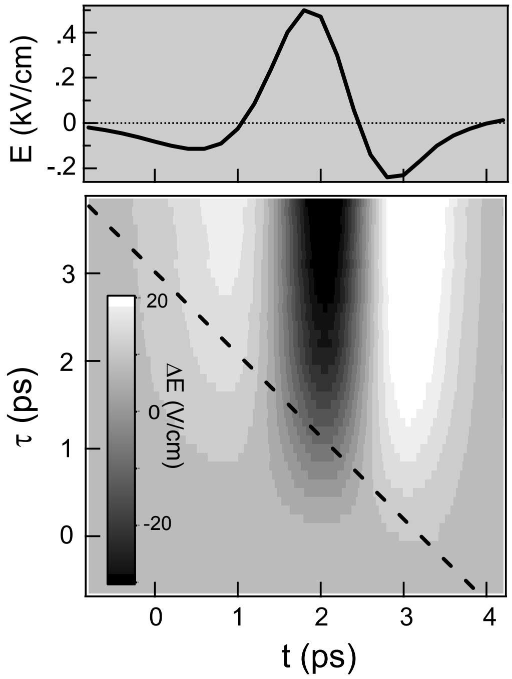

Figure 3.3 An example of a measurement with rapidly changing sample properties. Upper panel: THz field transmission through gallium arsenide wafer. Lower panel: modulation of transmitted field on excitation as a function of pump probe time τ. The dashed line shows the temporal path of the excitation pulse.

An example of such a measurement with rapidly changing sample properties is shown in figure 3.3. The lower panel of the figure shows the modulation of the THz field transmission through a gallium arsenide wafer (1 mm thick from Crystal-GmbH) after excitation with a 400 nm (3.1 eV) excitation pulse (fluence 10 mJ/m^2, FWHM 150 fs). The dashed line shows the diagonal temporal path of the excitation pulse in the measurement: each point on the temporal profile of the THz field arrives at a different time after excitation, such that the end of the THz pulse experiences a different material response from the start. This effect must be taken into account in any analysis that is aimed at deriving $\sigma(\omega, \tau)$ from the data.

3.6 Non-steady state analysis

In this section, analyses of material responses which vary on the timescale of the probe THz pulse are considered. As an introduction, it is instructive to first consider the contributions to the THz signal for a constant, time-independent carrier density (such as the situation depicted in figure 3.4(a)). Before taking into account the THz field actually used in the experiment, it is instructive to consider the impulse-response current $j(t)$ after an infinitely short pulsed field $E(t) = \delta(t-t')$. We can write the impulse-response current as the product:

$$J_\delta(t) = Nj_0(t), \tag{3.9}$$

where N is the concentration of (photo-excited) charge carriers and $j_0(t)$ is the single-particle current response function [10] – the contribution from as single charge to the time dependent current, after impulse by a delta-function field at time t=0. The sample conductivity spectrum $\sigma(\omega)$ – the quantity of interest – is the Fourier transform of $J_\delta(t)$. When N is time-independent, as in this steady-state approximation, $J_\delta(t)$ is simply proportional to $j_0(t)$, which decays with time after impulse by $\delta(t-t')$. In figure 3.4(a), the case for a Drude response is plotted, described by $j_0(t)=\exp(-t/\tau_r)$, with τ_r the Drude scattering time (see section 1.3).

The total current $J(t)$ generated by an *arbitrary* THz pulse $E_{trans}(t)$ is then obtained by integrating over the probe field

$$J(t) = N\int_{-\infty}^{\infty} E_{trans}(t')j_0(t-t')dt'. \tag{3.10}$$

This is more simply written as a convolution between the time dependent THz field and the current response function:

$$J(t) = NE_{trans}(t) * j_0(t). \tag{3.11}$$

In pump-probe experiments, the change $\Delta E_{trans}(t)$ in the transmitted THz field due to photoexcitation is measured. This is the electric field resulting from the charge acceleration described in the current response function. For a sample with an excitation thickness l_0, surrounded by a medium with dielectric function ε, it can be derived from the Maxwell equations [11] that the radiated field, $\Delta E_{trans}(t)$, and $J(t)$ are related through

$$\Delta E_{trans}(t) = -\frac{l_0}{2c\varepsilon_0\sqrt{\varepsilon}}J(t). \tag{3.12}$$

It should be noted that this solution applies only to samples with no dispersion and small modulations of the incident field, i.e. $\Delta E_{trans}(t) << E_{trans}(t)$. The applicability of these assumptions is discussed in section 3.8.

The sample conductivity spectrum $\sigma_0(\omega)$ in this steady state approximation can be obtained straightforwardly by considering the Fourier transforms of equations 3.11 and 3.12 so that

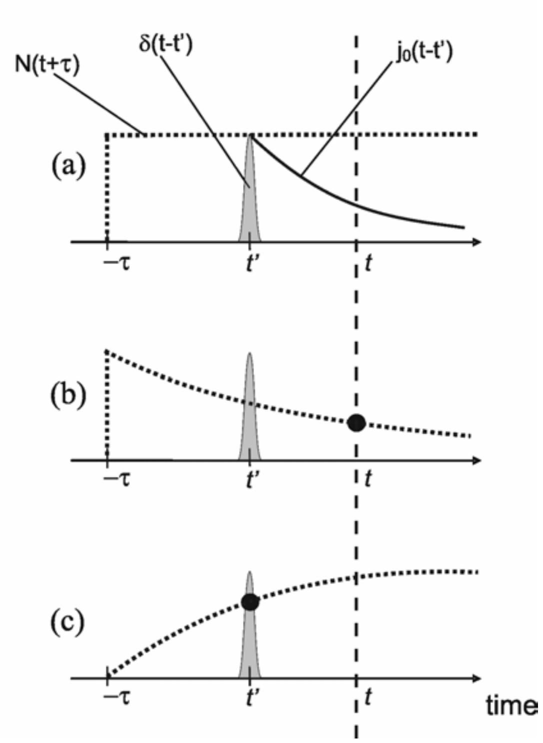

Figure 3.4 Evaluation of the current from an impulse by the THz field (here represented, for simplicity, as a delta function field $\delta(t-t')$). The current density, $J(\tau, t, t')$, at some time t (highlighted by the vertical large dash line) after excitation is separated into an amplitude function $N(t+\tau)$ –dotted line – which describes the amplitude dependence on the pump delay $(t+\tau)$, and the average single-particle response to the impulse field, $j_0(t-t')$ (solid line). (a) In the case where the conductivity is independent of pump-probe delay, $N(t+\tau)$ is constant in time and the current at time t is given by $J(\tau, t, t') = N\, j_0(t-t')$. (b) When the conductivity is *decreasing* with pump-probe delay, only the contribution of remaining particles at time t (highlighted by the black dot) is to be considered, such that the current density is given by $J(\tau, t, t') = N(t+\tau)\, j_0(t-t')$. (c) When the conductivity is *increasing* with pump-probe delay, $J(\tau, t, t')$ depends on the amplitude at time t' (at the time of impulse, again highlighted by the black dot), since any additional change in amplitude after this point is unaffected by the impulse field $\delta(t-t')$. Then, the current density at time t is given by $J(\tau, t, t') = N(t'+\tau)\, j_0(t-t')$.

$$\Delta E_{trans}(\omega) = \frac{-l_0}{2c\varepsilon_0\sqrt{\varepsilon}}\sigma_0(\omega)E_{trans}(\omega), \tag{3.13}$$

where $\Delta E_{trans}(\omega)$ and $E_{trans}(\omega)$ are the Fourier transforms of the THz time fields $\Delta E_{trans}(t)$ and $E_{trans}(t)$.

It should be noted that the above approach is valid only if the charge-carrier concentration N does not change significantly over the duration of the THz pulse (FWHM~1 ps), as assumed in references [12-14]. Also, (multiple) reflections have been ignored in this formulation for the sake of simplicity. This is equivalent to setting T=1 and R=0 in equation 3.2. In this case, if the photo-excited change in the THz field (ΔE_{trans}) is small compared to the transmitted field (E_{trans}), it can be shown (by approximating the exponential terms with their first order Taylor expansions) that equation 3.7 reduces to equation 3.13.

The extraction of $\sigma(\omega, \tau)$ from $\Delta E_{trans}(t, \tau)$ is considerably more complicated [4, 7] if $\sigma(\omega, \tau)$ varies on a timescale τ that is shorter than or comparable to the THz pulse duration, as different sample properties are probed with the beginning of the THz pulse than with the tail. This effect must clearly be taken into account in the data analysis.

A rapidly decaying signal, such as in references [8, 9], can be described by a time-varying charge density. The discussion above can easily be expanded for a population $N(t+\tau)$ decaying monotonously and simultaneously in the positive direction for both t and τ. Again, considering the simplified case of an infinitely short probe field $\delta(t-t')$, we must take into account the additional current decay in the temporal region t' to t – see figure 3.4(b) – since carriers that decay in this region do not contribute to the current at time t. The contribution of the remaining density to the current at time t is indicated by a black dot in figure 3.4(b), and is given by $N(t+\tau)$. Expanding this for a density decaying monotonously across an arbitrary THz pulse shape, we can follow the formalism introduced above (by equations 3.9-3.11) for a time varying density and obtain

$$J(t,\tau) = N(t+\tau)\left[E_{trans}(t) * j_0(t)\right]. \tag{3.14}$$

In order to extract the time-dependent conductivity from the data, we use a method that was introduced by Schmuttenmaer et al. [4, 7]. Prior to carrying out Fourier transforms on the time-domain data, we apply the transformation $\tau' = t+\tau$ to equation 3.14 and obtain

$$J'(t,\tau') = N(\tau')\left[E_{trans}(t) * j_0(t)\right]. \tag{3.15}$$

This is equivalent to projecting the experimental data along the path of the excitation pulse (shown by a dotted line in figure 3.3) so that all points on a horizontal cross section of ΔE_{trans} have the same pump-probe delay. The equivalent of equation 3.13 for time-dependent density is then given by

$$\Delta E'_{trans}(t,\tau') = -\frac{l_0}{2c\varepsilon_0\sqrt{\varepsilon}} J'(t,\tau'). \tag{3.16}$$

The conductivity spectrum, $\sigma(\omega,\tau')$ can then be calculated, as for the steady state case, by considering the one dimensional Fourier transforms of equations 3.15 and 3.16 so that

$$\Delta E'_{trans}(\omega,\tau') = -\frac{l_0}{2c\varepsilon_0\sqrt{\varepsilon}} \sigma'(\omega,\tau') E_{trans}(\omega). \tag{3.17}$$

The dependency of the conductivity on the pump-probe delay τ' is straightforward and represents the decay of the charge-carrier population, while the frequency-dependence corresponds to the response of an infinitely long-lived charge carrier.

It should be noted, however, that equations 3.14-3.17 do not adequately describe the case where new charge carriers are being created during or after the THz pulse. This problem is most easily illustrated again for a delta function probe field $\delta(t-t')$ – see figure 3.4(c). In the case that the density is *increasing* between t' and t, the additional charges are *not* affected by the field at time t', and hence do not contribute to any current at time t. The relevant density for calculating the current is then $N(t'+\tau)$ in place of $N(t+\tau)$. However, the introduction of t' dependence in N means that the equivalent form of equation 3.14 for increasing density is a complicated convolution:

$$J(t,\tau) = \left[\left\{N(t'+\tau)E_{trans}(t)\right\}\right] * j_0(t)\right], \tag{3.18}$$

and the interpretation of any extracted conductivity spectrum is not straightforward. This means that the transformation applied to the data (described above) does not give meaningful results when the pump and THz pulses overlap or when the onset of conductivity is slowed by charge particle cooling (contrary to previous claims [7, 8]). For this reason, we do not consider extraction of the complex conductivity from data for pump-THz delays < 0.5 ps.

The more general case – that of an arbitrarily changing density – does not readily allow for a simple analytical approach and extraction from of the complex conductivity from the data is far more complex. A more detailed mathematical extraction procedure, including the extraction of the conductivity spectrum at short times, is beyond the scope of this thesis, and will be presented in a later publication [11, 15].

3.7 Effects from the detector response function

Within the steady state approximation, the proportionality between detected waveforms (see equation 3.7) means the detector response function is not an important factor, as it simply divides out in data analysis. This means that the detected field $E(\omega)$, and that incident on the detector $E^{inc}(\omega)$, are completely interchangeable in analysis.

This is *not* the case when the sample properties are changing rapidly. After data projection (see equation 3.16) the parametric dependence of the modulated waveform ΔE_{trans} on the detection time t is convoluted, such that the proportionality on transformation to the frequency domain is removed. Therefore, before experimental data can be related to the conductivity, one additional step is required *before* projection and transformation: the deconvolution of the detector response function. The incident waveforms are related to the detected waveform through $E_{trans}^{inc}(\omega) = E_{trans}(\omega) / f_{\det}(\omega)$ and $\Delta E_{trans}^{inc}(\omega) = \Delta E_{trans}(\omega) / f_{\det}(\omega)$ – see section 2.3.

3.8 General notes

It should be noted that there are several assumptions made in the analysis described in section 3.6. Firstly, it assumes no dispersion between the propagation of visible pump and THz probe pulses in the excited region of the sample. This requires either that the absorption of the pump light is very strong (such that the excitation region is spatially narrow compared to the THz wavelength and can be treated as infinitely thin) or that the refractive indices of the sample at THz and visible frequencies are flat and comparable in magnitude (such that both pulses propagate at a similar speed in the sample). Care is also taken to ensure that the modulation of the THz field is much smaller than the incident THz field.

Secondly, the solutions to Maxwell's equations presented in equations 3.12 and 3.16 are exact only for an infinitely thin excited region surrounded by a homogeneous material, and do not properly take into account effects due to (multiple) reflections of the THz pulse. Reflection effects can be taken into account in a numerical analysis of THz propagation through a spatially extended excitation region (as in section 3.4), assuming that the pump-probe delays (τ) for all contributions of a transmitted THz pulse (i.e. each dotted line exiting to the right in figure 3.1) can be treated as identical. This requires either that the time for a THz pulse to transverse the excited region is fast compared to the time varying sample properties (generally true for a very strong pump absorption), or that the contribution of multiple reflections to the transmitted THz pulse is small (generally true for a very weak pump absorption).

Lastly, the analysis assumes that there is only one charge carrier type contributing to the signal. Therefore, the extracted conductivities and mobilities should only be considered as an approximate average of an ensemble. A more complex mathematical analysis which circumvents all of these approximations will be presented in a separate publication [11, 15].

3.9 Frequency units

The equations presented in this chapter allow the extraction of the frequency dependent complex conductivity $\sigma(\omega)$. The frequency represented in this quantity is the *radial* frequency, in radians per second. It should be noted that all extracted conductivities in this thesis are presented in units of THz, and are related to the corresponding radial frequencies through the factor $2\pi\times10^{12}$.

References

[1] E. Hecht, *Optics* (Addison Wesley, 4th edition, 2002) p426.
[2] M. C. Beard, et al., J. Phys. Chem. B **106**, 7146 (2002).
[3] P. C. M. Planken, et al., J. Opt. Soc. Am. B **18**, 313 (2001).
[4] J. T. Kindt and C. A. Schmuttenmaer, J. Chem. Phys. **110**, 8589 (1999).
[5] For single photon absorption, the absorption coefficient $\beta^{(1)}$ or penetration depth $l_0=1/\beta^{(1)}$ are related to the excitation intensity through $dI/dz=-\beta^{(1)}I$. The excitation density then follows $N\propto I\propto e^{-\beta z}$.
[6] The absorption coefficient is related to the visible refractive index n or dielectric function ε through $\beta^{(1)}=4\pi\,\mathrm{Im}(n)/\lambda$ or $\beta^{(1)}=4\pi\,\mathrm{Im}(\sqrt{\varepsilon})/\lambda$, where λ is the excitation wavelength.
[7] M. C. Beard, et al., Phys. Rev. B **62**, 15764 (2000).
[8] M. C. Beard, et al., J. Appl. Phys. **90**, 5915 (2001).
[9] E. Hendry, et al., Phys. Rev. Lett. **92**, 196601 (2004).
[10] N. V. Smith, Phys. Rev. B **64**, 155106 (2001).
[11] H. K. Nienhuys and V. Sundström, Phys. Rev. B **71**, 235110 (2005)
[12] E. Knoesel, et al., Phys. Rev. Lett. **86**, 340.
[13] E. Knoesel, et al., J. Chem. Phys. **121**, 394 (2004).
[14] J. Shan, et al., Phys. Rev. Lett. **90**, 247401 (2003).
[15] J. Schins, et al., in preparation.

Chapter 4

Electron transport in TiO_2 and TiO_2 solar cells

4.1 Background

Titanium dioxide (TiO_2) is a semiconductor widely used in photocatalysts and solar energy converters [1]. In these devices, the absorption of photons results in the generation of electrons and holes, which, upon separation, can provide an electric potential or trigger chemistry. A key factor determining the efficiency of these devices is the transport of the charges following photogeneration. In particular, for TiO_2-based dye-sensitized solar cells (Grätzel solar cells), it has been demonstrated that the efficiency is limited by electron transport through TiO_2 nanostructures [1, 2]. Higher electron mobility is therefore desirable, since it allows for a lower internal resistance of the cell, the possibility of longer recombination paths, and enhanced efficiency.

Although the transport of electrons in TiO_2 has received considerable attention, the nature and efficiency of electronic charge transport in TiO_2 has remained ambiguous: Despite the need for accurate values for charge mobility in bulk TiO_2, e.g. for precise modeling of solar cell properties, reported room-temperature electron Hall mobilities range from 0.01 to 10 cm^2/Vs [3-5]. In addition, the precise nature of the transport has remained unresolved. It is clear that the ionic character of TiO_2 gives rise to a strong electron-lattice interaction, described by coupling constant α_{ph}. This coupling leads to the formation of a polaron [6, 7], a quasi-particle consisting of an electron and the accompanying lattice deformation (see section 1.4). For a sufficiently strong interaction ($\alpha_{ph}>>6$), small polarons are formed with localized, self-trapped electrons, and charge transport occurs through tunneling or hopping from one local site to the next. Large polarons, with electron or hole wavefunctions that extend beyond the dimensions of the crystal unit cell, are formed for weaker coupling strength ($\alpha_{ph}<<6$) and exhibit Drude like behavior. In this picture a conduction electron entrains the lattice deformation, resulting in an effective (or polaron) mass exceeding its band mass (the mass associated with an electron in a rigid lattice).

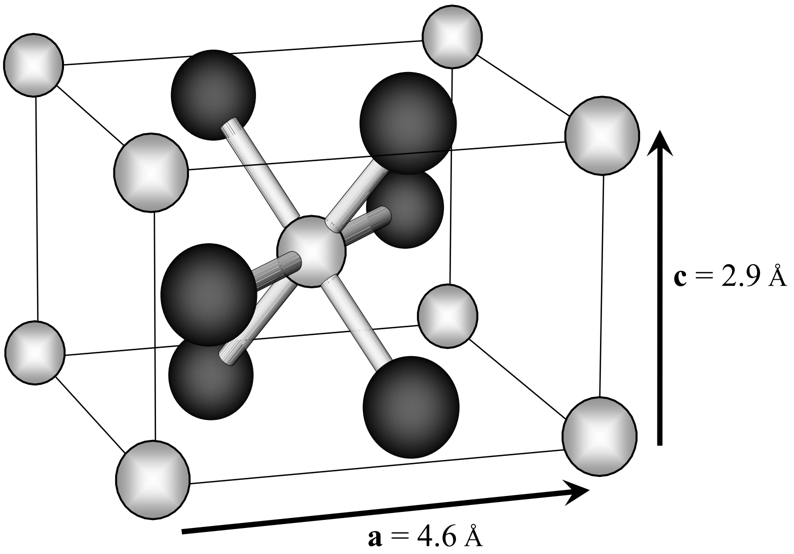

Figure 4.1 One unit cell of rutile (dark spheres – oxygen ions; light spheres – titanium ions). The large anisotropy in cell dimensions reflects the large anisotropy in many crystal properties.

Rutile is the most common and thermodynamically stable polymorph of TiO_2. It has a tetragonal crystal structure (see figure 4.1) described by lattice vectors **a**=4.6 Å and **c**=2.9 Å. As a result, the material is birefringent and has correspondingly large anisotropy in properties such as electrical conductivity [5].

Reports of the polaron mass (m^{**}) in rutile range from $8m_e$ - $190m_e$ (m_e = free electron mass) [5, 8-14], and there have been conflicting arguments for the existence of small [5, 6, 15] and large [11, 16] polarons in rutile. Also, as mentioned above, reported room temperature mobilities μ range from 0.01 to 10 cm^2/Vs [3-5]. The range of reported polaron mass and mobility span the complete crossover region [7] between small (μ <<1 cm^2/Vs, m^{**}>>m_e) and large (μ >>1 cm^2/Vs, m^{**}~m_e) polaron regimes.

Complications in these previous experimental studies may, however, be noted: firstly, carriers were introduced through oxygen deficiencies, which have been found to reduce conductivity significantly [3, 17] and give a temperature-dependent carrier concentration [11]. We circumvent these limitations by photo-exciting (stoichiometric) single-crystal rutile TiO_2 and investigating electron transport using THz-TDS (see chapter 2). This all-optical technique does not require electrodes, eliminating any effects from electrode impedance. From the measurement we also determine *drift* mobilities (proportional to the conductivity), which can be directly compared to theoretical calculations. The reliable experiments on rutile have measured *Hall* mobilities [3-5], with a strong magnetic field perpendicular to the current. In anisotropic materials such as rutile, these are not the same, and can have very different magnitudes and temperature dependences [4], making any comparison of previously measured mobilities to theory very difficult.

Our experiments allow the extraction of the complex, frequency dependent photoconductivity (see chapter 2), determined by the carrier *drift* mobility. Furthermore, THz-TDS measures the carrier mobility on a picosecond timescale. We can measure the mobility of carriers *after* thermalization with the lattice but before equilibrium with defect trapping states is achieved. Therefore we can determine short-term electron mobility (intrinsic to the material), rather than the long-term mobility (which includes time spent in defect-related traps) measured on longer timescales [18].

In this chapter, we investigate the charge transport properties of single crystal rutile TiO_2 and porous TiO_2 (used in Grätzel solar cells) using THz spectroscopy. In the single crystal sample we find transport to be limited by polaron formation, leading to an electron effective mass $m^{**}>>m_e$ and low electron mobilities ~1 cm^2/Vs at room temperature. In the porous sample, screening of the electric field due to spatial variations in the dielectric function restricts electron mobility further, and we set an upper limit for short term electron mobility in these samples ~10^{-3} cm^2/Vs. This value is still significantly larger than long term mobilities measured with time of flight techniques on porous samples, indicating that significant improvement of charge transport in Grätzel cells is possible.

4.2 Experimental details

The rutile TiO_2 samples, mounted in a closed-cycle Helium cryostat (10-300 K), are single-crystal rutile as grown commercially by Crystal GmbH. The band gap of rutile is 2.9 eV at room temperature, increasing slightly at lower temperatures [19]. The 1mm-thick (001) and (110)-cut crystals provide the possibility to study the electronic response with the (THz) electric field perpendicular (⊥) and parallel (//) to the **c** axis, respectively.

The transport of electrons in TiO_2 is investigated with the experimental set-up described in section 2.2. As shown in figure 4.2, THz pulses are essentially single cycle electromagnetic pulses, with a period of ~1 ps. The transmitted field strength is detected directly in the time domain. The transmission of these pulses through air, $E_{free}(t)$, the unexcited sample, $E_{trans}(t)$, as well as through the irradiated sample, $E_{trans}^{exc}(t)$, is recorded (see figure 4.2). In this last measurement, electrons can be excited into the conduction band either by linear absorption of 150 fs, 266 nm or 400 nm (fluence f_l typically ~4 Jm^{-2}) pulses, or by 2-photon absorption of 800 nm (f_l~30 Jm^{-2}). Data analysis is most conveniently performed in the frequency domain using the corresponding Fourier transforms of the time domain data: $E_{free}(\omega)$, $E_{trans}(\omega)$ and $E_{trans}^{exc}(\omega)$.

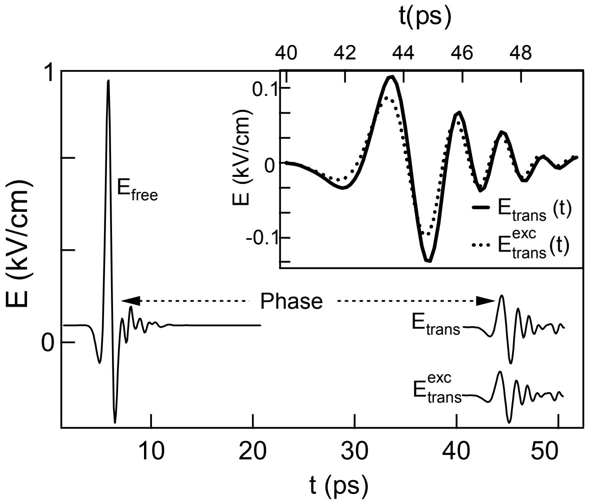

Figure 4.2 Three THz-scans at 30K, measured on a rutile (001) crystal, exciting with 4 J/m^2, 400 nm pulses: The pulse transmitted through, respectively, air ($E_{free}(t)$), the unexcited sample ($E_{trans}(t)$) and the photo-excited sample ($E_{trans}^{exc}(t)$). The scans contain both amplitude (absorption) and phase (refraction) information. Inset: $E_{trans}^{exc}(t)$ has a distinctly different shape from $E_{trans}(t)$, providing the phase and amplitude information required to extract both the real and imaginary part of part of the complex conductivity.

4.3 The ground state dielectric function of rutile

The temperature (T) dependent complex dielectric function, $\varepsilon(\omega, T)$, associated with the TiO_2 lattice, inferred from $E_{free}(\omega)$ and $E_{trans}(\omega)$ using the analysis using the analysis presented in section 3.2, is shown in figure 4.3 for various crystal temperatures. Only the real parts are plotted, since the imaginary parts are negligibly small (<< 1). The top panel shows the dielectric function of rutile at 0.6 THz, as a function of temperature. As there are no phonon modes (i.e. resonances) below this frequency, the dielectric function at 0.6 THz is essentially the zero-frequency value ε_{dc}, which is determined by the DC (direct current) polarizability of the material. The dielectric function of rutile is much larger than for many other semiconductors such as silicon (ε_{dc}=12). Larger values are measured in rutile with the

THz polarization parallel to the **c** axis (further denoted as 'parallel'), revealing that along this direction the material is more polarizable. While a decrease with temperature is measured in both crystal directions, the decrease is more marked in the parallel direction.

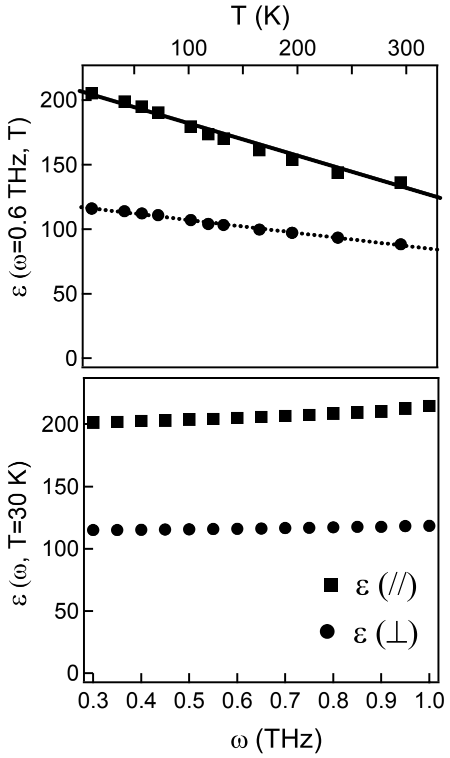

Figure 4.3 Upper panel: Temperature dependence of the real part of lattice dielectric function (ε) at 0.6 THz, extracted from $E_{free}(t)$ and $E_{trans}(t)$, with the THz polarization parallel (//) or perpendicular (⊥) to the **c** axis of the crystal. Only the real parts are plotted, since the imaginary parts negligibly small (more than two orders of magnitude smaller). The largest dielectric function is measured in the direction parallel to the **c** axis, though the anisotropy decreases slightly with temperature. Lower panel: Frequency dependence of the dielectric function at 30K, which is almost completely flat over this frequency range in the perpendicular direction, and increasing slightly with frequency in the parallel direction. The shape of the frequency dependence is similar at all temperatures. The lines drawn through the data in the upper panel (straight line fits yielding $\varepsilon_{//}$=207-0.265×T and $\varepsilon_{\perp}$=117-0.101×T) are to guide the eye.

The lower panel depicts the frequency dependence of the lattice dielectric function at 30K. There is a slight increase with increasing frequency, particularly in the **c** direction, caused by the resonance of the B_{1u} optical phonon centered at 3 THz [20]. For our relatively thick samples, this limits the transmitted frequency range to <1 THz. The relative increase in dielectric function (in the **c** direction) with increasing frequency does not change significantly with temperature.

4.4 Photoconductivity of rutile

By varying the delay between pump and probe THz pulses, it is observed that the change in the material response upon photoexcitation contained in $E_{trans}^{exc}(t)$, decays on a nanosecond timescale, i.e. much slower than the FWHM of the THz probe pulse of 1 ps. This means $E_{trans}(\omega)$ and $E_{trans}^{exc}(\omega)$ can be analyzed using the quasi-steady state approximation described in section 3.4 to extract the photoconductivity, $\sigma(\omega)$. For 2-photon excitation with 800 nm (where the photon energy lies below the band gap of rutile) the excitation density is homogeneous throughout the sample. This makes it straightforward to iteratively solve equation 3.5 for the complex conductivity $\sigma(\omega,T)$ for any given lattice temperature T, using the transmission through the excited (E_{trans}^{exc}) and unexcited (E_{trans}) sample, coupled with prior measurement of the ground state dielectric function (ε) described in the previous section.

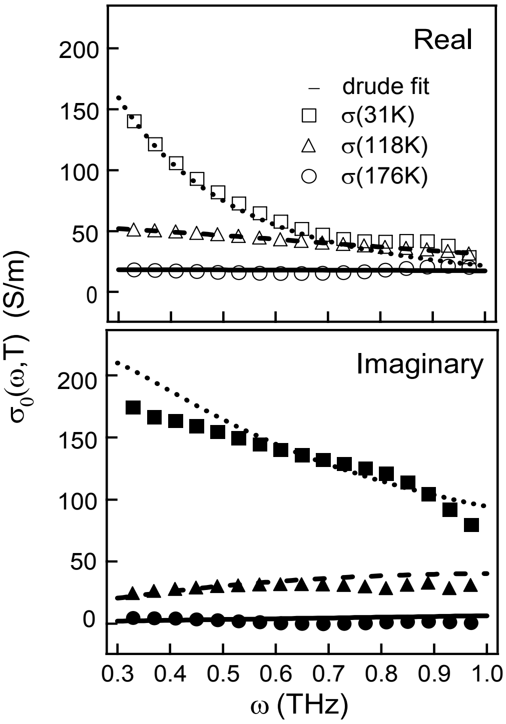

Figure 4.4 Pump (400 nm) induced complex conductivity at the sample interface (real parts plotted as hollow symbols, imaginary parts as filled symbols) measured perpendicular to the **c** axis for three different temperatures. The Drude model describes the data very well (lines), with one scattering time for both real and imaginary response at each temperature. A similar response is observed perpendicular to the **c** axis.

While the principle of extracting $\sigma(\omega,T)$ from E_{trans}^{exc}, E_{trans} and ε is the same for 400 nm excitation, the strong absorption causes an exponentially decaying density of photogenerated carriers (described by decay constant l_0~10 μm at 300 K, slightly larger at low temperatures, with virtually no anisotropy [19], i.e. much smaller than the sample thickness (L=1 mm)). This spatial variation of the excitation density must be taken into account by iteratively solving equation 3.7. The extracted photoconductivities at the sample interface, measured at three different sample temperatures and with the THz polarization perpendicular to the **c** axis, are plotted in figure 4.4.

By comparing the conductivity of photo-excited rutile to transmission experiments on a reduced sample (n-type doped TiO_{2-x}, x~0.0005 prepared according to ref. [21]) in the temperature range 10-110 K, it is apparent that the pump-induced THz absorption originates from electrons excited into the conduction band. This observation is corroborated by band calculations, which suggest that the conductivity band mass of photo-excited hole charges is more than four times that of photo-excited electrons [22, 23]. These heavy holes are much less mobile than the lighter electrons, and have a comparatively small response to the applied THz field.

At the low 400 nm fluences (f_l~4 Jm^{-2}) used in these measurements, a linear dependence of the sample response on fluence is observed. We also observe identical responses for 800 nm and 400 nm excitation, indicating that only the number of electrons determines the signal, and not their spatial distribution. This indicates that carrier-carrier interactions do not have a significant contribution to the measured signal. Indeed, the measured data can be very well described by Drude model (see equation 1.5), presented as lines in figure 4.4. These fits are determined by two parameters: the plasma frequency ω_p and the Drude relaxation, or scattering, time τ_r, plotted in figure 4.5 as a function of temperature. The plasma frequency ω_p is determined, amongst others, by the charge density, which is a function if the excitation fluence. The data in figure 4.5 were recorded at constant fluence. The decrease in the conductivity with increasing temperature observed in figure 4.4 is primarily determined by a strong decrease in the relaxation time (the time in between momentum changing collisions that act to impede the flow of current) with increasing temperature. Below 150 K we are able to fit the real and imaginary parts of the complex conductivity using the Drude model to directly extract both τ_r and ω_p. At higher temperatures (>150 K), the loss of phase information in the measured data (as the imaginary part of $\sigma(\omega)$ tends to zero) leads to an increased scatter in both ω_p and τ_r.

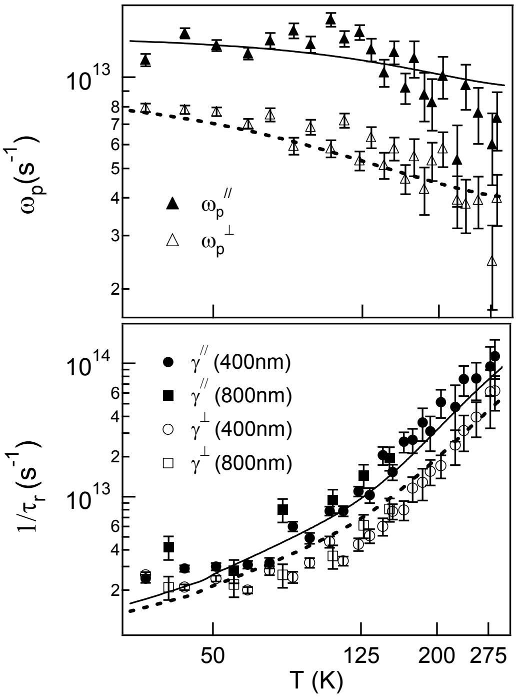

Figure 4.5 Plasma frequency ω_p (top) and the inverse of the Drude relaxation time τ_r (bottom) from fits to the measured photoconductivity, plotted as a function of temperature. The open symbols show the results in the perpendicular (⊥) direction (measured with the THz polarization perpendicular to the **c** axis) and the filled symbols in the parallel (//) direction (measured with the THz polarization parallel to the **c** axis). The lines are results of the Feynman polaron model (see section 4.6).

4.5 Scattering from phonons

Figure 4.5 reveals a decrease in τ_r by almost two orders of magnitude on increasing the sample temperature from 30 K to 300 K. The anisotropy of polaron transport is also clearly evident, with a larger scattering rates measured in the parallel direction. The very small relaxation times measured at room temperature (corresponding to one collision, on average, every 10 femtoseconds) are a consequence of scattering from longitudinal lattice vibrations (phonons). As the mobility is proportional to the Drude relaxation times, it is evident that polaron transport becomes increasingly hindered as the phonon density increases with temperature.

We can describe the temperature dependence of τ_r in figure 4.5 by considering separate contributions from acoustic (low frequency) and optical (high frequency) phonons.

At low temperatures, scattering from low-frequency acoustic phonons dominates, described by a $T^{3/2}$ temperature dependence [24]. At higher temperatures, the occupation of higher frequency optical phonons of the crystal will dominate scattering [25, 26]. We can sum the separate contributions to the scattering rate from acoustic and optical phonons:

$$\frac{1}{\tau_r} = \frac{1}{\tau_{acoustic}} + \frac{1}{\tau_{optical}} = \beta T^{3/2} + \frac{1}{\tau_{optical}(\alpha_{ph}, T)} \tag{4.1}$$

The $\beta T^{3/2}$ term describes scattering from acoustic phonons and $\tau_{optical}(\alpha_{ph}, T)$ describes the average time in between scattering events due to longitudinal optical (LO) phonons, as a function of the temperature T and electron-phonon coupling constant α_{ph}. This parameter characterizes the interaction between the electron and the surrounding lattice, which determines the electron-phonon scattering rate. In addition to its role in determining the scattering rate and the associated mobility, $\alpha_{ph.}$ is also the critical parameter describing polaron formation in the material, determining, e.g. the size of the polaron. Thus an analysis of the temperature-dependent phonon scattering times in figure 4.5 will also shed light on the nature of polarons in TiO_2.

4.6 The Feynman polaron model

A weak electron-lattice interaction results in a shallow potential well, and the effect on the electron wave function is correspondingly weak. Perturbative treatments, such as those embodied in the Lee, Low and Pines polaron model [25, 27], can then be used to describe the quantum mechanical electron-lattice interaction. As, in this case, the electron wave function extends over a relatively large spatial range, the electron is termed a *large* polaron, and is essentially delocalized and Drude-like in nature, with a small increase in electron mass. When the electron-lattice interaction is strong enough to generate a deep potential well, the electron wave function becomes localized. Transport can then only occur by hopping or tunneling from one site to the next. This self-trapped electron is termed a *small* polaron. The region in-between, where the electron wave function has a spatial extension comparable to the crystal lattice unit cell, is termed the *intermediate* coupling regime.

The large dielectric function of rutile (see figure 4.3) suggests that electron-phonon coupling in rutile should be fairly strong in nature, owing to the correspondingly large polarizability [28]. Indeed, small polarons in TiO_2 has been reported previously [5, 6, 15]. On the other hand, the two characteristics of small polaron transport (an increase in conductivity with both temperature and frequency [7]) are not observed in our experimental data. In fact, the observation that the conductivity is described fairly well within the Drude model indicates that the electrons are free to move through the lattice. Although both large (α_{ph}<<6) and small (α_{ph}>>6) polaron theories have been applied to describe polaron transport in TiO_2 [5, 15, 25], it is clear that a reliable description of the electron-phonon coupling requires analysis within the intermediate coupling regime (α_{ph} in the range 1 to 10) [28].

Although numerous electron-phonon coupling theories exist which work well in either the large and small polaron extremes, the crossover region is somewhat problematic [29, 30]. The non-perturbative approach in Feynman's polaron theory [30-33] is the only one which predicts the correct limits in both the large and small polaron regimes [30]. This means the theory can be applied without *any* prior assumptions regarding the electron-phonon coupling strength, and is applicable also in the intermediate regime.

The scattering efficiency and effective mass for an electron interacting with a phonon (with frequency ω_{ph}) are obtained from the Feynman polaron model by minimizing the expression for the free energy of an electron [33] including its temperature dependent interaction with the polarizable lattice. It is assumed that one phonon mode dominates the interaction. The dominant longitudinal optical (LO) phonon modes of TiO_2 can be inferred from the inverse of the infrared dielectric function, obtained from infrared spectroscopy [26]. For both crystal directions in rutile, LO phonon modes with essentially identical frequencies (ω_{ph}=24 THz, 800 cm^{-1} and ω_{ph}=25 THz, 830 cm^{-1}, with symmetries A_{2u} and E_u for parallel and perpendicular directions respectively [11, 28, 34]) dominate the spectra. These modes are expected to govern the polaron formation and the electron-phonon scattering processes. The resulting electron-phonon scattering rates calculated from the Feynman energy minimization procedure, with ω_{ph}=24 THz, are plotted in figure 4.6. The optical phonon scattering rate is dependent on both the electron-phonon coupling constant α_{ph} and the temperature T. The dashed lines show the coupling parameters α_{ph} that best reproduce the experimental data in figure 4.5: the data (lines) can be described using just two adjustable parameters – β (acoustic phonon contribution) and α_{ph} (optical phonon contribution) – using equation 4.1. This results in $\alpha_{//}$=4.0±0.5 and $\alpha_{\perp}$=6.0±0.5 for parallel and perpendicular crystal directions, respectively. Remarkably, the perpendicular coupling constant has two solutions in the Feynman analysis that are compatible with our experimental observations. To discern between the two, we make use of the constraint imposed by the conductivity band mass anisotropy [22, 23]: stronger coupling is concomitant with the higher electron band mass expected in the perpendicular direction [7, 33]. For both directions, the optical phonon scattering dominates over the acoustic phonons, except at the lowest temperatures (T<100 K).

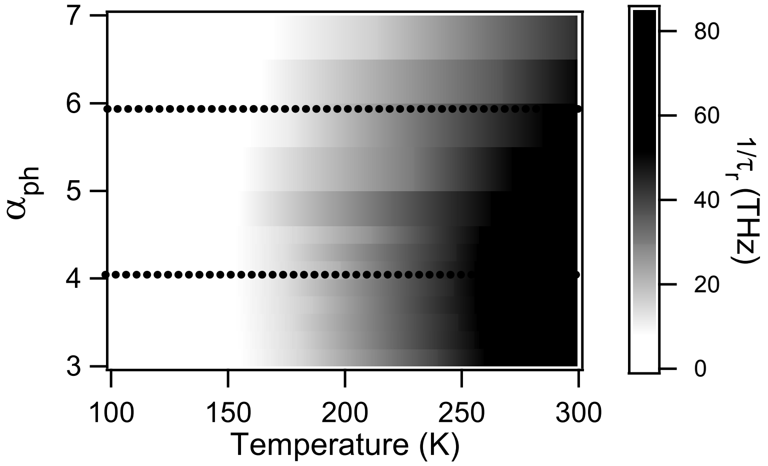

Figure 4.6 Temperature and coupling dependent polaron scattering rates calculated using Feynman polaron theory [30-33] for a phonon frequency of 24 THz.

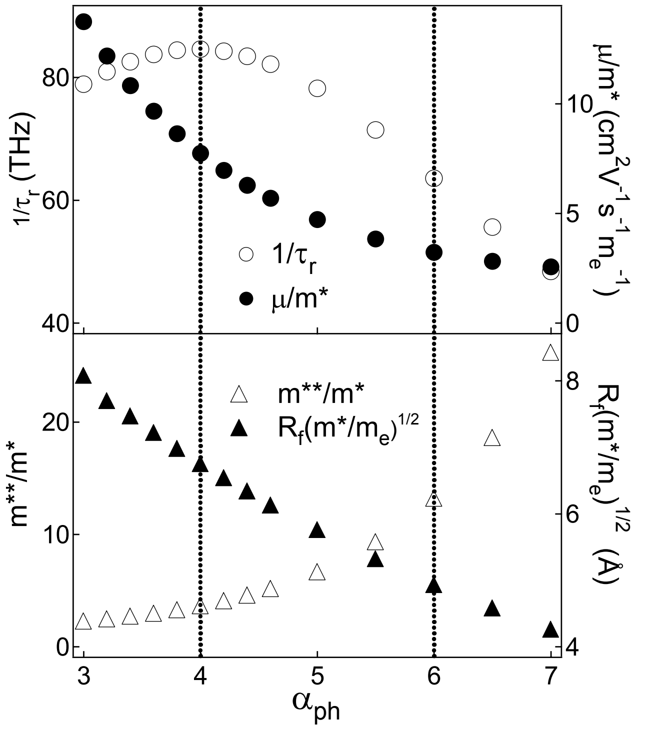

Figure 4.7 Polaron scattering rate ($1/\tau_r$), mobility (μ), mass (m^{**}), and radius (R_f), the latter three normalized to the crystal band mass (m^*), as a function of electron-phonon coupling strength α_{ph}, calculated using Feynman polaron theory [30-33] for a phonon frequency of 24 THz, a temperature of 300 K, and α_{ph} between 3-7. In this range, while the polaron mobility is a monotonically decreasing function of α_{ph}, the polaron scattering rate exhibits a maximum at α_{ph}=4. This region can be considered as a cross-over from large to small polaron behavior, as indicated by the rapidly increasing effective mass m^{**} and decreasing polaron radius R_f. Dashed lines denote values relevant for TiO_2 along the **a** and **c** axis.

An interesting feature of the experimental data in figure 4.5 is that the *higher* polaron scattering rate is observed for charge transport along the crystal direction for which a *higher* mobility has been previously reported [4, 5]. This counter-intuitive result can be understood by noting that the DC mobility $\mu = e\tau_r/m^{**}$ (see equation 1.3) is determined not only by the scattering time τ_r, but also by the polaron effective mass m^{**}. Although the scattering time τ_r is smaller along the **c** axis, the mobility μ is higher compared to the **a** axis. This is due to a lower polaron mass along the **c** axis. There are two factors contributing to this lower polaron mass along the parallel direction. The first is the anisotropy of the electron conductivity band mass m^*: ab-initio calculations of the band mass yield $m^*_{//}=0.6m_e$ and $m^*_{\perp}=1.2m_e$ [22, 23]. A more significant factor arises from a unique feature the Feynman polaron theory: As shown in figure 4.7, the calculated scattering rate at T=300 K as a function of α_{ph} exhibits a turning point at α=4, *i.e.* above α=4 the scattering from optical phonons actually begins to *decrease* with increasing coupling strength. In contrast, the polaron mobility and radius are monotonically decreasing functions of the electron-phonon coupling strength. This situation arises for $\alpha>4$ as the polaron mass (plotted in the lower panel of figure 4.7) tends rapidly towards the extremely large values associated with the small polaron regime [7].

Using ab-initio predictions for electron conductivity band mass of $m^*_{//}=0.6m_e$ and $m^*_{\perp}=1.2m_e$ [22, 23], the (room-temperature) polaron masses obtained from the Feynman model are $m^{**}_{//}=2m_e$ and $m^{**}_{\perp}=15m_e$ for $\alpha_{//}=4.0$ and $\alpha_{\perp}=6.0$, respectively. Thus, the anisotropy in polaron mass is sufficiently large to counteract the anisotropy in the scattering rate, resulting in room-temperature mobilities of $\mu_{//}=9.5$ cm^2/Vs and $\mu_{\perp}=1.7$ cm^2/Vs. Though not expected to be identical in anisotropic media (see section 4.1), our derived drift mobilities nicely reproduce the anisotropy of recent Hall measurements [5]. It should be noted that tight binding estimates of the band mass ($m^*\sim 8m_e$ [15]) predict much lower electron mobilities (<1 cm^2/Vs), although these are still well within the range of reported values [15]. The inferred mobilities are substantially smaller than those in more commonly used semiconductors such as silicon ($\mu\sim$1400 cm^2/Vs).

Again using ab-initio estimates for the band mass, the polaron mean free path l_r (the average distance traveled between scattering events) can be obtained, assuming a classical thermalized electron distribution described by root mean square speed $\sqrt{3k_bT/m^{**}}$, through $l_r \equiv \tau_r \times \sqrt{3k_bT/m^{**}}$, with k_b the Boltzmann constant and T the sample temperature. At 30K, this yields a mean free path $l_r\sim$40-100 Å, depending on crystal direction. By 300K the mean free path has decreased to $l_r\sim$4-10 Å, comparable to the lattice unit cell dimensions, testimony of the substantial electron-phonon coupling.

	τ_r	α_{ph}	m^*_{ai}	m^*_{tb}	m^{**}_{ai}	m^{**}_{tb}	μ_{ai}	μ_{tb}	Rf_{ai}	Rf_{tb}
	(fs)		(m_e)	(m_e)	(m_e)	(m_e)	(cm^2/Vs)	(cm^2/Vs)	(Å)	(Å)
Parallel (//)	11	4	0.6	~8	2	~26	9.5	~0.8	8.9	~2.5
Perpendicular (⊥)	15	6	1.2	~8	15	~100	~1.7	0.3	4.5	~1.8

Table 4.1 Room temperature properties of a polaron moving parallel and perpendicular to the **c** axis in rutile. From left to right: relaxation time (measured), electron-phonon coupling strength (from fits to Feynman model), band masses from ab-initio (ai) [22, 23] and tight binding (tb) [15] calculations, polaron masses, mobilities and polaron radii for ab-initio and tight binding band masses.

The polaron radius – the spatial extent of the electronic wavefunction – is also determined by the electron-phonon coupling constant, an can be estimated following Schultz [30]. The result is plotted in figure 4.7. For both the ab-initio and tight binding electron band masses (see table 4.1) the calculated radius is comparable to the lattice spacing of the crystal (a = 4.6 Å and c = 2.9 Å). It is evident that the polaron radius is comparable to the lattice unit cell dimensions, making both the small and large polaron limits inappropriate. The intermediate size of the polaron – neither small nor large – may account for some of the conflicting conclusions drawn from previous studies of transport in rutile [5, 6, 11, 15, 16].

4.7 Conductivity at high densities

Carrier-carrier interaction effects are important in doped semiconductor devices, where a relatively small number of constituent impurities can generate very high electron densities in the semiconductor conduction band. To investigate the role of carrier-carrier interactions in rutile, the rutile sample is excited with 266 nm photons instead of 400 nm photons, allowing for the generation of much higher excitation densities (the optical penetration depth is l_0~20 nm at 266 nm [35] as opposed to 10 μm at 400 nm [19]). This allows the study of sample conductivities in the high density regime, to investigate at what density, and how, carrier-carrier interactions begin to play a role in the conductive response of a material.

Whereas a collision between two electrons does not directly alter their combined drift momentum (i.e that generated by an externally applied field) and hence should not be included as a momentum scattering event within (for example) the Drude model, electron-*hole* scattering does contribute to momentum relaxation, as the drift momentum of a hole is opposite in sign to that of the electron. At high densities, we expect electron-hole collisions to play a role in photoconduction. Since the strength of the Coulomb interaction between an electron and a hole is strongly dependent on screening effects of the medium, we expect the effect of electron-hole scattering to change drastically with the polarizability of the material. In this section, the effects of carrier interaction in TiO_2, a high dielectric function material, are compared to those in silicon, a low dielectric function material.

Figure 4.8 shows examples of extracted conductivity, normalized to incident fluence, exciting the rutile sample (measured in the ⊥ direction at 30 K) and the silicon sample (0.5 mm industrial, non-doped wafer from ASMI, also at 30 K) with 266 nm photons. The conductivities in both silicon and TiO_2 are measured 10 ps after excitation, i.e. after thermalization of the charge distribution, but before any significant decrease in conductivity is observed due to carrier trapping or recombination. The penetration depth of 266 nm absorption is very small in both samples: l_0~20 nm for rutile [35], and l_0~10 nm for silicon [36], which introduces complications in the extraction of conductivity (see Refs. [37] and [38]).

For fluences $f_l < 1$ J/m^2 (the response for f_l=0.18 J/m^2, 2.4×10^{17} photons/m^2, is shown in figure 4.8(a)), the conductivity of rutile scales linearly with excitation fluence, and does not significantly change in it's frequency dependence, and the Drude model describes the data fairly well with parameters ω_p=54 THz and τ_r=0.4 ps (lines in figure 4.8(a)). This indicates that, at these low fluences, the generated densities are sufficiently low that charges are uncorrelated: photo-excited electrons behave as isolated, non-interacting charges. Plotted in figure 4.8(b) is the conductivity found for a higher excitation fluence f_l=6.40 J/m^2 (8.6×10^{18} photons/m^2). Clearly the shape of the frequency response changes drastically in this high density regime: on increasing the excitation fluence, the crossing point of the real and imaginary parts of the conductivity shifts towards higher frequencies. The lines in figures 4.8(b), respectively, are Drude model fits with parameters ω_p=2000 THz and τ_r=0.18 ps. While the plasma frequency scales linearly with excitation fluence, the scattering time is lowered dramatically upon increasing the charge density.

The lower panels in figure 4.8 show the extracted conductivities for the silicon crystal. It is clear that the conductivity in silicon varies in a similar manner to that in rutile with increasing excitation fluence. However, the observe changes occur already at much lower excitation fluences in silicon. The differences between figures 4.8(a) and (c) – the low fluence results for TiO_2 and Si – can be fully accounted for by the differences in scattering rates of isolated carriers in these different materials: the Drude model describes the Si data with parameters ω_p=95 THz and τ_r=2.5 ps (lines in figure 4.8(c)). As in rutile, the scattering time in silicon is lowered dramatically on increasing the excitation fluence: the lines in figures 4.8(d) is the best fit with parameters ω_p=1500 THz, τ_r=0.18 ps.

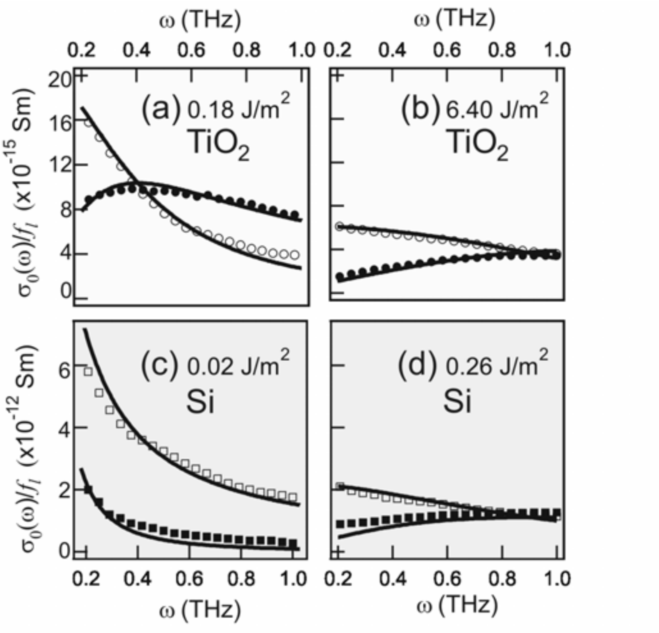

Figure 4.8 Real (open symbols) and imaginary (filled symbols) of the complex conductivity for rutile (in the ⊥ direction, upper panels) and silicon (lower panels), measured with different excitation fluences: (a) f_l=0.18 J/m^2, 2.4×10^{17} photons/m^2, (b) 6.40 J/m^2, 8.6×10^{18} photons/m^2 (c) 0.02 J/m^2, 2.5×10^{16} photons/m^2 and (d) 0.26 J/m^2, 3.5×10^{17} photons/m^2. All conductivities are normalized to the incidence excitation fluence. Solid lines represent fits using the Drude model, with decreasing relaxation times for higher densities.

The changes in scattering rate are too large to be due to local heating of the lattice: an upper limit for the local temperature changes on excitation can be made from the specific heat (~0.7 J/g/K in both materials) and mass density (2.3 g/cm^3 and 4.1 g/cm^3 for silicon and rutile respectively), assuming the above band gap energy is dissipated into the lattice. Even for a large excitation density N_0~10^{25} m^{-3} this results in a modest temperature increase per pulse of ~3 K and ~0.8 K in silicon and TiO_2 respectively. For thermal diffusion coefficients typical to semiconductors (in silicon >>1 cm^2/s at low temperatures) diffusion length scales for the 1 ms between excitation pulses are larger than the sample thicknesses, such that equilibrium with the cryostat is reasonably well maintained, and no significant steady-state heating is expected.

At high excitation density, however, the relaxation rate is expected to be a sum of contributions from charge-phonon scattering (τ_{ph}) and electron-hole scattering (τ_{eh}):

$$\frac{1}{\tau_r}=\frac{1}{\tau_{eh}}+\frac{1}{\tau_{ph}}. \tag{4.2}$$

The electron-hole (hole-electron) scattering rate is simply proportional to the hole (electron) concentration N_0 [39], so that equation 4.2 can be rewritten as

$$\frac{1}{\tau_r} = a \times N_0 + \frac{1}{\tau_{ph}}, \tag{4.3}$$

where a is just a proportionality factor. Assuming that the density is proportional to the excitation fluence (true for the initially excited charge distribution), this linear dependence is observed for the case of silicon in figure 4.9. The small deviations from linearity in figure 4.9 may be explained by density dependent diffusion effects [37]. Since the masses of electrons and holes in silicon are of comparable magnitude [40, 41], both are expected to contribute to the THz conductivity spectrum, and the relaxation times displayed in figure 4.9 are an average of both the electron and hole contributions.

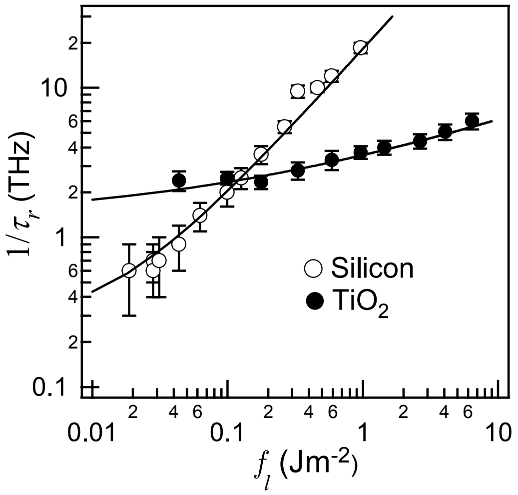

Figure 4.9 Value of relaxation time τ_r obtained from fitting the high density conductivity, plotted as a function of excitation fluence f_l. The lines are theoretical fits described in text.

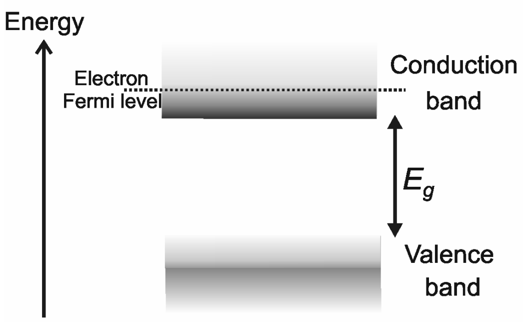

Figure 4.10 Band structure of a strongly photo-excited semiconductor: increasing occupation of the conduction band leads to a buildup of electrons in higher energy levels. The highest occupied energy level at T=0 K is referred to as the Fermi energy level.

While the increase in scattering rate with intensity in silicon is linear because of electron-hole scattering, the scattering rate in TiO$_2$ increases much more slowly with increasing fluence: the log-log plot in figure 4.9 indicates that the scattering rate in TiO_2 varies with $\sim f_l^{1/3}$. This suggests that a different density effect is operative in rutile. Momentum relaxation is also expected to be affected by band filling effects (in addition to electron-hole scattering effects): in a weakly photo-excited semiconductor, the electrons reside near the bottom of the conduction band and holes near the top of the valence band. In this low density regime, the electron hole gas behaves classically, and can be described by kinetic theory, i.e. the gas has a thermal distribution with root mean squared velocity given by

$$v_{thermal} \approx \sqrt{3k_b T / m_{dos}}, \tag{4.4}$$

where m_{dos} is the density of states effective mass, i.e. the mass which provides the density of states from the expressions for one isotropic, parabolic minimum. In anisotropic materials, or materials with multiple band minima, the density of states effective mass and the conductivity effective mass (which accounts for the complex band structure in conductivity calculations) are not expected to be identical [42].

On increasing the excitation density, the Pauli Exclusion Principle causes higher energy states of the semiconductor to be occupied. As a result, the average velocity will be correspondingly higher than predicted by kinetic theory. In materials with densely occupied conduction bands, where the highest occupied energy state (the Fermi level) is well away from the band minimum, the electron Fermi velocity (v_f) can be orders of magnitude higher than predicted by kinetic theory, and is given by

$$v_f = \frac{\hbar}{m_{dos}} \left(\frac{3\pi^2 N_0}{M} \right)^{1/3}, \tag{4.5}$$

where M is the number of equivalent band minima. As the average velocity of the electron (or hole) distribution increases with increasing density, the relaxation time will decrease. This is the cause of the very much smaller relaxation times in metals (typically <1 fs [43]) compared to those for typical semiconductors. As opposed to the electron-hole interaction described above, this latter effect is essentially due to electron-electron interactions.

Since the conductivity is determined by electron (or hole) states which are within thermal energies of the free states above the Fermi level, we expect a crossover on increasing the conduction band occupation, as the average velocity of the electron distribution increases from that determined by classical kinetic theory (in the limit $v_f \ll v_{thermal}$) to that of a quantum electron gas determined by the Fermi velocity ($v_f \gg v_{thermal}$). A very approximate description of the scattering rate resulting from this process is just the sum of the scattering rate of thermal electrons ($1/\tau_0$) plus the *increase* in scattering rate due to the shift of the Fermi level. Writing this contribution as v_f/l_{ph}, where l_{ph} is the electron mean free path, we get

$$\frac{1}{\tau_{ph}} = \frac{1}{\tau_0} + \frac{v_f}{l_{ph}}. \tag{4.6}$$

Equation 4.6 has the general features required of the scattering time: it tends asymptotically towards the two limiting cases as v_f increases from effectively zero at low density to values larger than $v_{thermal}$. The total scattering rate (i.e. including electron-hole scattering) may be written as

$$\begin{gathered} \frac{1}{\tau_r} = a \times N_0 + \frac{1}{\tau_0} + b \times \left(N_0\right)^{1/3}, \\ b = \frac{\hbar}{l_{ph} m_{dos}} \left(\frac{3\pi^2}{M}\right)^{1/3}. \end{gathered} \tag{4.7}$$

For acoustic phonon scattering (the dominant mechanism at low temperatures, see sections 4.5 and 4.6), the mean free path is expected to be independent of electron velocity [24]. Therefore, it is reasonable to assume a mean free path that is independent of excitation density, and can be estimated from $l_{ph} = \tau_0 \times \sqrt{3k_b T / m_{dos}}$. It should be noted that this approximation neglects screening of the electron-phonon interaction. However, this is clearly not the dominant effect here: screening should *lower* the scattering rate (*increase* the mean free path [44]) while we observe an *increase* in scattering rate with excitation fluence in figure 4.9.

Since the charge distribution in TiO$_2$ is not expected to vary significantly between pump and probe times, a straightforward estimation of the excitation density in the sample can be made from the measured incident pump fluence f_l, taking into account both the penetration depth (l_0~20 nm at 266 nm for rutile [35]) and reflective losses of the pump beam at the sample interface (see equation 3.3, with ε_{exc}=3.7+10.2i [35]):

$$N_0 \approx \frac{f_l}{l_0} \times \left| \left(\frac{2}{1+\sqrt{\varepsilon_{exc}}} \right)^2 \right|. \tag{4.8}$$

It should be noted that this is only an estimation of the excitation density in the sample, and is certainly an *upper* estimate, since we ignore diffusional and ballistic transport in the time window between excitation and the arrival of the THz probe pulse (for a more detailed discussion see ref. [37]).

Due to the coupling to optical phonon modes in TiO$_2$ (which increases greatly for heavier charges [28]) the hole contribution to the signal for rutile is expected to be negligible. Therefore, the data presented in figure 4.9 represent the effects of electron-hole and electron-electron (detailed above) interactions only. Calculations of the electron conduction band indicate that the band minimum in rutile is not degenerate [22], so that M=1 in equation 4.7.

The rutile scattering rates can then be fitted using equations 4.7 and 4.8, with parameters a=0 and b=7×10^{-9} (i.e. assuming no electron-hole scattering contribution) – see line in figure 4.9. This indicates that electron-electron interactions dominate over electron-hole interactions for TiO_2. The best fits to the data occur for $a<0.15\times10^{-25}$ and $b>2\times10^{-9}$, corresponding to an electron density of states effective mass in the range $m_{dos}\sim 6m_e - 20m_e$. Although the analysis described here contains some crude approximations, and, since rutile is anisotropic, the density of sates effective mass is not expected to be the same as the conductivity effective mass discussed in section 4.6 [42], the resulting electron mass in rutile is clearly consistent with calculated values (see table 4.1), in particular those from ab-initio calculations. Since, through neglect of diffusion effects [37], our estimation of N_0 is an *upper* limit, the values of m_{dos} obtained from fitting the data are certainly *lower* limits.

From the sub-linear fluence dependence of the scattering rate observed in rutile (figure 4.9), it is evident that the dominant scattering mechanism at the excitation densities used here is *not* electron-hole scattering. We expect electron-hole scattering to play an important in role in rutile at higher densities. In any case, it is clear that the highly polarizable lattice of rutile (and correspondingly high dielectric function) efficiently screen the coulomb interaction between electrons and holes [39], leading to much weaker electron-hole interactions in rutile than in silicon.

Due to the larger mobility of charges in silicon, the effect of charge redistribution between pump and probe pulses is larger in silicon than in rutile [37], so that a precise determination of the charge density in the silicon sample is more difficult. However, it is clear from figure 4.9 and Ref. [37] that the effects of charge-charge (in particular electron-hole) interactions on the conductivity appear at much lower densities in silicon that in rutile (one to two orders of magnitude lower). This is testament to the low dielectric function in silicon, which screens the coulomb interaction much less effectively than in rutile. The reason for the absence of significant electron-electron interactions in Si can be traced to the band structure. While the band structure of rutile is non-degenerate, the multivalley band structure of silicon (M=6 [45] in equation 4.7), so that band filling effects will not be observed until a 6-fold higher density is achieved..

In summary, titanium dioxide, compared to more common semiconductors such as silicon, is a very polarizable material (low temperature static dielectric function >100 and 12 respectively). At low electron densities, the lattice polarizability limits conductivity in rutile through polaron formation. At higher densities, however, screening of the Coulomb interaction in rutile means that electron-hole scattering does not significantly lower conductivity, while in silicon the scattering rate increases linearly for fluences >0.1 Jm^{-2}. In contrast, band filling effects do play a significant role in rutile due to the non-degeneracy of the band structure, as opposed to the 6-fold degenerate band in Si.

4.8 Electron transport in TiO_2 solar cells

The high cost of material processing required to produce silicon solar cells has remained a limiting factor for the implementation of solar electricity on a large scale. In recent years, this has fuelled research into possible low cost alternatives to silicon solar cells. In particular, pioneering work by O'Regan and Grätzel [46] has led to the development of thin film dye-sensitized TiO_2 solar (Grätzel) cells. These cells consist of a porous network of TiO_2 nanoparticles (see figure 4.11), acting as a transport matrix for photo-excited electrons. To reduce energy loss due to the large bandgap of TiO_2, the particles are sensitized with dye molecules which act as light absorbers, transferring energy from photoexcitation into mobile electrons in the conduction band of the TiO_2 matrix.

These cells, despite having a very high efficiency for the initial step (the conversion of visible photons into mobile conducting electrons), suffer from problems with low energy conversion [1], which limits their commercial viability as an alternative to the traditional silicon solar cell. The efficiency of these devices is limited, to a large extent, by the slow transport of the charges through the TiO_2 network [2, 47].Increasing the transport capability of the porous network is therefore critical to improving the overall efficiency of such thin film solar cells. While much work so far has involved monitoring the process of the electron being injected from the dye in to the semiconductor; and determining the speed at which this action occurs, the steps following charge injection have remained much less studied.

For TiO_2, both the mean free path and polaron size (section 4.6) are orders of magnitude smaller than the typical ~25 nm diameter particles, and scattering processes in nanostructures should therefore be dominated by bulk TiO_2 properties. However, the much lower reported room temperature mobilities of photo-generated carriers in *porous* rutile [48] ($<10^{-5}$ cm^2/Vs, as opposed to ~1 cm^2/Vs reported in section 4.6) indicate that charge transport in solar cells is not limited by electron-phonon interactions. In this section, the THz conductivity of an unsensitized (i.e. without dye) nanoporous TiO_2 film is compared to that of a rutile single crystal (in the $\perp$ direction). The nanoporous sample consists of a several microns thick film of Degussa P25 TiO_2 (particles of 25 nm diameter) spun onto a 1 mm thick quartz substrate. The comparison between a nanoporous sample and bulk rutile allows direct insight into the modified properties of nanoporous materials.

The porous rutile sample is a sintered composite of TiO_2 nanoparticles (see figure 4.11), i.e. it is an inhomogeneous mix of vacuum and semiconductor regions. In order to extract the conductivity of such a sample, the dielectric properties of the porous TiO_2 must therefore be derived using effective medium theory. The two most widely applied effective medium theories are those of Maxwell-Garnett (MG) [49] and Bruggeman (BR) [50]. For the effective dielectric function ε of non-interacting spherical particles with dielectric function ε_p embedded within a medium ε_m (=1 for air) – see figure 4.11 – the Maxwell-Garnett and Bruggeman theories take the form

MG: $$\frac{\varepsilon - \varepsilon_m}{\varepsilon + 2\varepsilon_m} = s\frac{\varepsilon_p - \varepsilon_m}{\varepsilon_p + 2\varepsilon_m}, \tag{4.9}$$

BR: $$s\frac{\varepsilon_p - \varepsilon}{\varepsilon_p + 2\varepsilon} = (s-1)\frac{\varepsilon_m - \varepsilon}{\varepsilon_m + 2\varepsilon}, \tag{4.10}$$

where s is the space filling factor. Both of these effective medium theories have limits to their applicability, as they weigh various characteristics of the problem differently. For example, Bruggeman's theory is only applicable to non-polarizable materials [50], making it unsuitable in this case. The derivation of the MG equation, meanwhile, requires the assumption of low space filling factor (strictly speaking $s<0.15$ [50]), as it neglects polarization coupling between particles. Despite this, there is convincing evidence which suggests that MG theory is more applicable to porous materials than Bruggeman's theory, producing more meaningful results even for materials with space filling $s>0.15$ [50, 51]. Indeed, it is thought that MG theory is generally superior for all granular materials [52]. For these reasons, we choose to apply MG theory to our measurements on porous TiO_2.

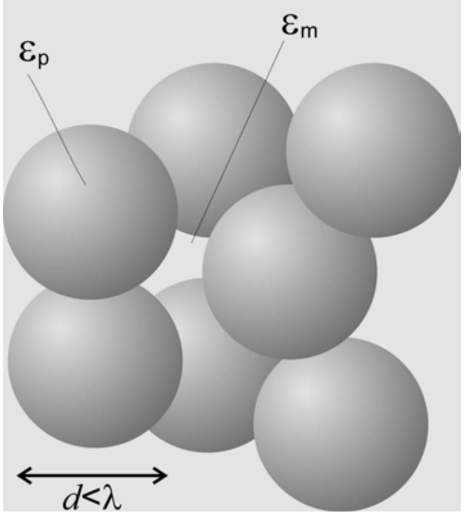

Figure 4.11 Nanoporous TiO_2: the sample is made from fused nanoparticles of TiO_2, average diameter d~25 nm. The sample has an effective dielectric function determined by the particle material ε_p and the medium (ε_m=1 for air).

Equation 4.9 is valid for spherical particles of diameter smaller than the probe wavelength. Although this criterion is readily met, it should be noted that the application of this equation to porous TiO_2 still requires a further approximation: the sample is not pure rutile type TiO_2, and is a mixture between rutile and anatase type TiO_2 with a ratio of around 1:3. However, the transport properties are found to be similar in both polymorphs [6, 53], and anatase and rutile devices have similar characteristics [54]. For want of a more detailed analysis, we apply MG theory using our measured values for the dielectric function of rutile. The isotropic dielectric function (i.e. for randomly orientated particles) at THz frequencies is then given by the dielectric function in figure 4.3: $\varepsilon_p=(\varepsilon_\perp+2\varepsilon_{//})/3=140$ at 30 K.

The porous TiO_2 used in the experiment has a space filling factor $s\sim 50$ %, such that the effective sample dielectric function at THz frequencies is estimated using equation 4.9 to be $\varepsilon\sim 3.9$. This value agrees well with estimates we make from the transmitted THz field using the analysis in section 3.2. At the frequencies in the excitation pulse used in the experiment (266 nm, 4.65 eV), the effective dielectric function, given the bulk dielectric function at 266 nm is $1.8+10.2i$ [35], is calculated to be $\varepsilon_{exc}=3.1+1.0i$, from which a penetration depth $l_0=70$ nm is inferred. A consequence of the conductivity extraction using these parameters, which takes into account the spatially decaying excitation density (see section 3.4), is that the extracted conductivities are also a varying function of spatial coordinate z. For a meaningful comparison between the different samples, we consider, as before, the conductivity at the interface $\sigma(z=0)$ normalized to the density of absorbed photons at the sample interface, defined as: $\sigma_0=\sigma(z=0)/N_0$. This quantity allows for a convenient and meaningful comparison between the conductivities in the two samples with very different excitation densities (characterized by penetration depths of $l_0\sim 10$ nm and 70 nm for single crystal and nanoporous samples, respectively).

In figure 4.12, the conductivity of single crystal rutile is compared to that of the porous TiO_2 sample. Both these measurements have been measured with the same fluence (266 nm, 1.06×10^{18} photons/m^2), low enough to avoid the charge-charge interaction effects detailed in section 4.7, and measured at $T=30$ K (before the onset of scattering from optical phonons). From the excitation fluence, N_0 is estimated to be $\sim 7.6\times10^{24}$ m^{-3} and $\sim 2.6\times10^{25}$ m^{-3} for single crystal and nanoporous samples respectively, using equation 4.8.

The most striking feature of the data in figure 4.12 is that the normalized conductivity in nanoporous TiO_2 is around three orders of magnitude lower than in the bulk rutile. While the conductivity in bulk rutile is described fairly well by the Drude model (full lines in the upper panel in figure 4.12), with $\omega_p=260$ THz and $\tau_r=0.4$ ps, the frequency dependence of the conductivity in the nanoporous sample is vastly different, and the imaginary component is even opposite in sign. We observe a similar frequency dependence in a dye sensitized porous sample [55] excited by 400 nm pulses (~10^{18} photons/m^2, see inset of figure 4.12).

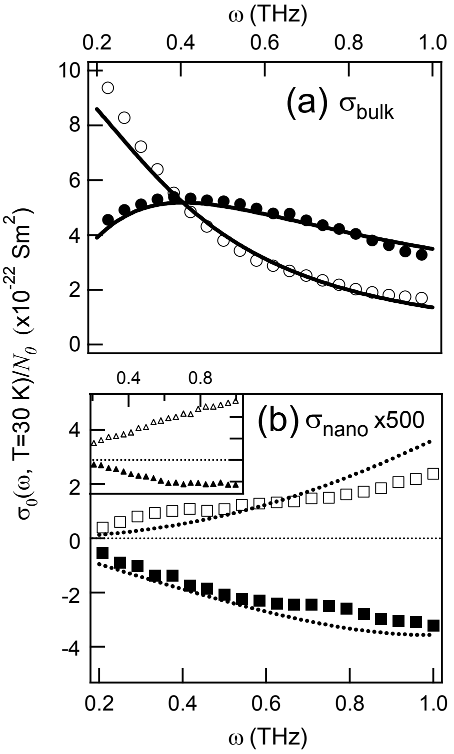

Figure 4.12 THz conductivities of the single crystal (a) and porous (b) TiO_2 samples, the real (open symbols) and imaginary (closed symbols) parts, normalized by the excitation density at the sample interface. The lines are fits to the Drude model (full) and Maxwell-Garnett effective medium theory (dotted, see text). Inset: THz conductivity of dye-sensitized sample excited by 400 nm light.

The distinctive THz response of porous TiO_2 observed in figure 4.12(b) is very similar to that previously observed by Turner et al [55] for sensitized samples with similar estimated electron densities. In this reference, the authors attributed this unusual frequency dependence to back-scattering of electrons due to the finite size of the particles. However, the small mean free paths of electrons in rutile (section 4.6) suggest that surface scattering, even at low temperatures and in a high purity sample, is negligibly small. The effective conductivity measured in the inhomogeneous TiO_2 sample must, however, be treated within effective medium theory. For Maxwell-Garnett theory, effective conductivity σ (i.e. the macroscopic conductivity of the sample) is related to the particle conductivity σ_p (i.e. the microscopic conductivity within the constituent particles) through the equation

$$\frac{\varepsilon + {}^{i\sigma}\!/_{\omega\varepsilon_0} - \varepsilon_m}{\varepsilon + {}^{i\sigma}\!/_{\omega\varepsilon_0} + 2\varepsilon_m} = s\frac{\varepsilon_p + {}^{i\sigma_p}\!/_{\omega\varepsilon_0} - \varepsilon_m}{\varepsilon_p + {}^{i\sigma_p}\!/_{\omega\varepsilon_0} + 2\varepsilon_m}. \qquad (4.11)$$

Combining equations 4.9 and 4.11 and solving for the effective conductivity σ yields

$$\sigma = \frac{9s{\varepsilon_m}^2}{s(\varepsilon_m - \varepsilon_p) + 2\varepsilon_m + \varepsilon_p} \times \frac{\sigma_p}{(s(\varepsilon_m - \varepsilon_p) + 2\varepsilon_m + \varepsilon_p) - {}^{i\sigma_p(s-1)}\big/_{\omega\varepsilon_0}}. \tag{4.12}$$

The effective conductivity calculated using equation 4.12, assuming a Drude model conductivity for σ_p with ω_p=110 THz and τ_r=0.1 ps, is plotted in the lower panel of figure 4.12 (dotted lines). The fit has all of the main features of the measured data: conductivity much smaller than in bulk, an increasing conductivity with frequency and a negative imaginary component. It may be noted that the best fit to the experimental data occurs with a plasma frequency ω_p and relaxation time τ_r larger and smaller (respectively) than expected for single crystal rutile. There are several reasons why this may be: firstly the purity of the crystal in the nanoporous TiO_2 will not be as high as in the single crystal sample, such that impurity scattering may play a significant role at these low temperatures. Secondly, the effective conductivity has been extracted ignoring the mixed phase composition (rutile vs. anatase in the ratio 2:3) of the nanoporous TiO_2. The third approximation, and possibly most significant, is the application of Maxwell-Garnett theory itself. Strictly speaking, Maxwell-Garnet theory only applies to an effective medium composed of isolated spherical particles. In reality, nanoporous TiO_2 is a sintered composite made from a distribution of nanoparticle shapes. This will give rise to a larger conductivity than that predicted by Maxwell-Garnett theory, especially at low frequencies, where interparticle transport will play a more important role. It is clear, however, that effective medium theory at least qualitatively predicts the features of the conductivity, without the need for introducing more exotic effects such as surface scattering [55] or charge build up at the particle interface [56].

The fluence dependence of the normalized conductivity in nanoporous TiO_2 is also very different from that of bulk rutile. While, at these low excitation densities, the normalized conductivity in bulk rutile is independent of excitation fluence, the normalized conductivity in nanoporous TiO_2 is strongly density dependent (see upper panel of figure 4.13, plotted for excitation fluences 0.40×10^{18} photons/m^2, 0.82×10^{18} photons/m^2 and 1.06×10^{18} photons/m^2).

Using equation 4.8 to estimate the excitation densities (N_0~2.8×10^{24} m^{-3}, 5.8×10^{24} m^{-3} and 7.6×10^{24} m^{-3}), and scaling the Drude plasma frequency correspondingly, equation 4.12 reproduces the features in the measured data fairly well (see lines in the upper panel of figure 4.13). The reason why the observed effective conductivity does not simply scale with excitation density, even if the particle conductivity does, is apparent from the function dependence of equation 4.12. Maxwell-Garnet effective medium theory also predicts the much weaker temperature dependence observed in nanoporous TiO_2 compared to bulk rutile (see open squares in lower panel of figure 4.13). The fit (dotted line) has been calculated using equation 4.12, assuming the temperature dependence of the THz dielectric function observed in bulk rutile (see figure 4.3) and the temperature dependence of electron-phonon scattering time (lines in bottom panel of figure 4.5) in the Drude conductivity. Both these quantities have been averaged over the two crystal directions.

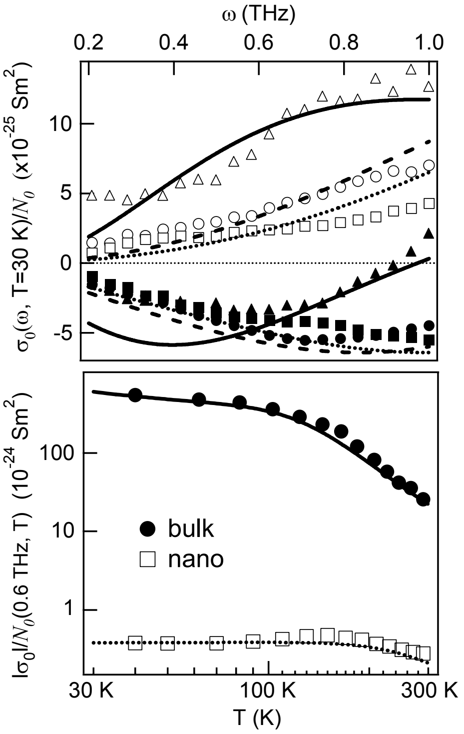

Figure 4.13 Upper panel: effective conductivity (open and filled symbols for real and imaginary parts respectively) measured at 30K in nanoporous TiO_2 for excitation fluences of 0.40×10^{18} photons/m^2, 0.82×10^{18} photons/m^2 and 1.06×10^{18} photons/m^2 (triangles, circles and squares respectively). The lines represent fits from Maxwell-Garnett effective medium theory. Lower panel: temperature dependence of the conductivity in single crystal rutile (filled circles) and nanoporous TiO_2 (open squares). The solid line is the temperature dependence predicted by the Drude model, with the relaxation time dominated by electron-optical phonon scattering (see section 4.6), given the temperature dependent THz dielectric function in bulk rutile plotted in figure 4.3. The dotted line represents the much weaker temperature expected for these effects within Maxwell-Garnett effective medium theory.

For the low electron densities ($N_0<10^{22}$ m^{-3} [57]) and high temperatures ($T\sim300$ K) applicable to operational solar cells, the corresponding low values of particle conductivity mean that equation 4.12 may be approximated by:

$$\sigma = \frac{9s\varepsilon_m^{\ 2}}{(s(\varepsilon_m - \varepsilon_p) + 2\varepsilon_m + \varepsilon_p)^2} \times \sigma_p. \tag{4.13}$$

Using the directionally average THz dielectric function ($\varepsilon_p=(\varepsilon_\perp+2\varepsilon_{//})/3=100$ at 300 K) in bulk rutile, equation 4.13 predicts that the conductivity in a porous TiO_2 sample with space filling s~50 % is reduced from that in the bulk material by around three orders of magnitude. Microscopically, this effect arises from the screening of an applied field by the highly polarizable component particles, leading to a larger flux density in the medium (in this case air) than in the TiO_2 particles (see figure 4.14). The local field experienced by an electron inside one of these particles is then lowered from that expected for a homogeneous sample of the bulk material, registering as a lower effective conductivity.

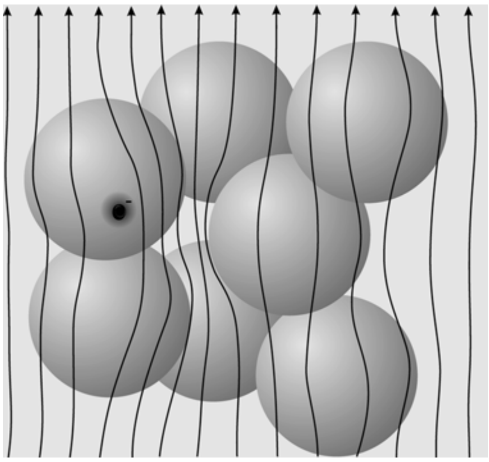

Figure 4.14 Schematic representation of the electric field lines (arrows) in a porous material: distortion due to shielding by the highly polarizable component particles leads to a redistribution of field strength within the material. The local field experience by an electron inside a particle is lowered from that experienced by an electron in the bulk material, leading to much lower conductivities in porous materials.

With THz spectroscopy, we measure the *short-term* mobility, the average mobility of charges on a ~1 ps timescale (i.e. not including time spent in traps). The mobility observed here for bulk rutile (~1 cm^2/Vs) therefore represents the *intrinsic* limit for electron transport at room temperature in single crystal TiO_2, while the value measured in the porous sample (~10^{-3} cm^2/V), represents the upper limit for electron mobility in porous TiO_2. Although the scattering rates inferred from our THz measurements are comparable for the two systems, Maxwell-Garnett effective medium theory reveals that the different mobilities are a result of screening of the electric field by the highly polarizable lattice. Hence, we expect the charge mobility μ (the quantity determining the motion of charges in response to an *electric field*) to be orders of magnitude lower in porous TiO_2 than in the single crystal. In a working solar cell, in which the pores are filled with an electrolyte solution, the contrast between ε_m and ε_p is expected to be lower, leading to a higher effective mobility than observed here. In any case, we do not expect such effects to influence the diffusion constant D (the quantity determining the *diffusive* transport of charge), since this quantity is unaffected by electric fields. While μ will determine the internal resistance of a cell, D is the important term describing the diffusive transport of charge to the outer electrodes of a cell and hence determines the overall quantum efficiency. We have shown here that a simple relationship between μ and D is not expected in polarizable porous materials, and that common experimental methods (such as time of flight measurement [48]) do not probe the *local* transport properties of porous materials. Our results further demonstrate that a lowering of the cell internal resistance is possible if screening effects can be reduced, either by increasing the spacing filling factor in the porous material, by using a *less* polarizable material for the transport matrix or using a *more* polarizable material for the medium (i.e. electrolyte).

Lower *long-term* electron mobilities (i.e. including time spent in defect-related traps [18]) have been observed in porous TiO_2 with time of flight measurements ($<10^{-5}$ cm^2/Vs [48], as opposed to $\sim10^{-3}$ cm^2/Vs reported here). One might expect a significant reduction of the long-term charge mobility in the porous sample due restrictions placed on the random walk of a charge, leading to slow interparticle transport, though low mobilities have also been attributed to efficient electron trapping [58]. Such effects would also lower the *diffusional* transport of charge, contributing to the low efficiency of TiO_2 solar cells [2, 47]. Eliminating these long-term transport effects would therefore increase the long-term mobility in porous TiO_2, as well as *diffusion* coefficient, by up to two orders of magnitude.

References

[1] K. Kalyanasundaram and M. Gratzel, Coord. Chem. Rev. **177**, 347 (1998).
[2] N. Kopidakis, et al., J. Phys. Chem. B **104**, 3930 (2000).
[3] R. G. Beckenridge and W. R. Hosler, Phys. Rev. **91**, 793 (1953).
[4] V. N. Bogomolov and V. P. Zhuze, Sov. Phys. Solid State **5**, 2404 (1964).
[5] E. Yagi, et al., Phys. Rev. B **54**, 7945 (1996).
[6] A. S. Alexandrov and N. Mott, in *Polarons and Bipolarons* (World Scientific, Singapore, 1995), p.155.
[7] D. Emin, Phys. Rev. B **48**, 13691 (1993).
[8] J. Pascual, et al., Phys. Rev. B **18**, 5606 (1978).
[9] G. A. Acket and J. Volger, Physica **32**, 1680 (1966).
[10] V. Cristea and V. Babes, Phys. Status Solid A **45**, 617 (1978).
[11] J. F. Baumard and F.Gervais, Phys. Rev. B **15**, 2316 (1977).
[12] J. W. DeFord and O. W. Johnson, J. Appl. Phys. **54**, 889 (1983).
[13] T. R. Sandin and P. H. Keeson, Phys. Rev. **177**, 1370 (1969).
[14] W. R. Thurber and A. J. H. Mante, Phys. Rev. **139**, A1655 (1962).
[15] V. N. Bogomolov, et al., Sov. Phys. Solid State **9**, 2502 (1968).
[16] A. E. Myasnikova, Phys. Lett. A **291**, 439 (2001).
[17] V. N. Bogomolov and P. M. Shavkunov, Sov. Phys. Solid State **5**, 1481 (1963).
[18] A. Germeau, et al., Phys. Rev. B **65**, 165331 (2002).
[19] H. Tang, et al., Phys. Rev. B **52**, 7771 (1995).
[20] J. D. Traylor, et al., Phys. Rev. B **3**, 3457 (1971).
[21] C. W. Chu, Phys. Rev. B **1**, 4700 (1970).

[22] K. M. Glassford and J. R. Chelikowsky, Phys. Rev. B **46**, 1284 (1992).
[23] Private communication with J. R. Chelikowsky.
[24] J. Bardeen and W. Shockley, Phys. Rev. **80**, 72 (1950).
[25] F. E. Low and D. Pines, Phys. Rev. **98**, 414 (1955).
[26] J. Shan, et al., Phys. Rev. Lett. **90**, 247401 (2003).
[27] T. D. Lee, et al., Phys. Rev. **90**, 297 (1953).
[28] D. M. Eagles, J Phys. Chem. Solids **25**, 1243 (1964).
[29] Y. Lépine and Y. Frongillo, Phys. Rev. B **46**, 14510 (1992).
[30] T. D. Schultz, Phys. Rev. **116**, 526 (1959).
[31] R. P. Feynman, Phys. Rev. **97**, 660 (1955).
[32] R. P. Feynman, et al., Phys. Rev. **127**, 1004 (1962).
[33] R. W. Hellwarth and I. Biaggio, Phys. Rev. B **60**, 299 (1999).
[34] F. Gervais and B. Piriou, Phys. Rev. B **10**, 1642 (1974).
[35] M. Cardona and G. Harbeke, Phys. Rev. **137**, 1467 (1965).
[36] H. R. Philipp and E. A. Taft, Phys. Rev. **120**, 37 (1960).
[37] The conductivity extraction analysis neglects effects of charge diffusion in-between excitation and the arrival of the THz probe at time τ. An estimate of this effect can be obtained from the characteristic diffusion length $l_{dif}\sim\surd(D\tau)$, with the diffusion coefficient D determined by the thermal the thermal electron velocity $v_{dif}\sim\surd(3k_bT/m^{**})$ through $D\sim(v_{dif})^2\tau_r$. For hot charges there is an additional effect to consider due to ballistic electron transport: fast moving electrons, velocity $v_{bol}\sim\surd(2(E_{ph}-E_g)/m^{**})$, just after excitation by a photon of energy E_{ph}, in a time $\tau_{bol}\sim100$ fs after excitation (J.R. Goldman and J.A. Prybyla, Phys. Rev. Lett. 72, 1364 (1994)), can cover a characteristic distance $l_{bol}\sim v_{bol}\tau_{bol}$. In silicon at low excitation densities, with effective mass $m^{**}=0.2m_e$ (R. N. Dexter, et al., Phys. Rev. 96, 222 (1954)) and band gap $E_g=1.2$ eV, both diffusive and ballistic effects are large: <200 nm for both l_{dif} (for $\tau=10$ ps, $T=30$ K) and l_{bol}, compared to the penetration depth $l_0\sim10$ nm. At higher excitation densities, increases scattering rates are expected to lead to smaller values for both l_{dif} and l_{bol}. These characteristic lengths are expected to be one to two orders of magnitude lower in TiO_2 due the large electron effective mass (see table 4.1), larger band gap and stronger scattering from phonons. For TiO_2, the assumption that the charge distribution does not change much in-between pump and probe times is therefore justified. In the silicon sample, the uncertainty in the charge distribution introduces a factor of ten error in the *absolute* magnitudes of the extracted interface conductivities presented here. Nevertheless, since we measure the THz wave transmitted through the entire excited region (and the modulation of the THz is, to a first approximation, proportional to the *product of density and penetration depth*), the error in the ratio of two measured conductivities is relatively small. Comparison *between* measured conductivities on the same sample is therefore still possible.
[38] It should also be noted that, at high densities, equation 3.6 (the separation of the complex conductivity into a product of frequency and spatially varying functions), does not strictly hold, as the response of a charge to the applied field depends on charge density, which varies along the spatial coordinate of laser propagation. The extracted conductivities therefore represent an average response of all charges, dominated by carriers in the region of high excitation density.
[39] C. A. Kukkonen and P. F. Maldague, Phys. Rev. Lett. **37**, 782 (1976).
[40] R. N. Dexter, et al., Phys. Rev. **96**, 222 (1954).
[41] R. N. Dexter, et al., Phys. Rev. **96**, 224 (1954).
[42] T.H.Geball, in *Semiconductors*, edited by N.B.Hannay (Reinhold Publishing, New York, 1959), p.330.
[43] N. W. Ashcroft and N. D. Mermin, in *Solid State Physics (1st edition)* (Saunders College, 1976), p10.
[44] S. D. Sarma, et al., Phys. Rev. B **37**, 6290 (1988).
[45] C. Tejedor and J. A. Vergés, Phys. Rev. B **19**, 2283 (1979).
[46] B. Oregan and M. Gratzel, Nature **353**, 737 (1991).
[47] A. Solbrand, et al., J. Phys. Chem.B **101**, 2514 (1997).
[48] T. Dittrich, Phys. Status Solidi A **182**, 447 (2000).
[49] A. Kirchner, et al., Phys. Rev. B **57**, 277 (1998).
[50] J. E. Spanier and I. P. Herman, Phys. Rev. B **61**, 10437 (2000).
[51] C. G. Granqvist and O. Hunderi, Phys. Rev. B **18**, 2897 (1978).
[52] J. I. Gittleman and B. Abeles, Phys. Rev. B **15**, 3273 (1977).
[53] L. Forro, et al., J. Appl. Phys. **75**, 633 (1994).
[54] N. G. Park, et al., J Phys Chem B **104**, 8989 (2000).
[55] G. M. Turner, et al., J. Phys. Chem. B **106**, 11716 (2002).
[56] H. K. Nienhuys and V. Sundstrom, Appl. Phys. Lett. **87**, 012101 (2005)
[57] J. Nelson, et al., Phys. Rev. B **63**, 205321 (2001).
[58] J. A. Anta, et al., Phys. Rev. B **65**, 125324 (2002).

Chapter 5

Exciton formation in ZnO

5.1 Background

In semiconductors with a low dielectric function, the shielding of charges is relatively weak, and Coulomb potentials between the negative electrons and the positive hoiles can be higher than their combined thermal energies. In this case, electrons and holes may form weakly bound electron hole pairs (Wannier excitons – see figure 5.1), rather than being separate, independent entities, as in high dielectric materials. Because of the similarity to hydrogenic solutions to the Schrödinger equation, the discreet energy levels of a Wannier exciton are assigned state descriptions 1S, 2S, 2P etc (figure 1.6). Excitons in direct gap semiconductors are also highly luminescent, and excitonic semiconductors are widely used in electro-optic devices. In particular zinc oxide (ZnO) has an exceptionally large exciton binding energy (60 meV [1]) and correspondingly high luminescence efficiency. As such, it is has been proposed as a possible lasing material for a UV polariton laser [2].

Following above-gap photoexcitation of low-dielectric semiconductors, excitons are formed in a two-step process: firstly, the thermalization and cooling of the hot electron-hole plasma gas takes place, allowing the formation of excitons with excess center of mass momentum ($\boldsymbol{K}\neq0$). Secondly, relaxation to the $\boldsymbol{K}=0$ state occurs. The vast majority of experimental work has employed time-resolved luminescence to probe the exciton formation dynamics (see for example [3-6]). Unfortunately, optical absorption/emission is most sensitive to the $\boldsymbol{K}=0$ state of the exciton [7, 8]. Hence, with the exception of recent time-resolved interband luminescence [8] and THz [9] measurements on confined exciton systems, optical experiments generally probe the combined rate due to both exciton formation *and* momentum relaxation. As a result, it is difficult to distinguish between a process with fast formation and slow momentum relaxation, and a process with slow formation and fast momentum relaxation.

In highly photo-excited semiconductors, excited above the so-called Mott density (in ZnO ~3×10^{23} m^{-3} [10, 11]), electron-hole interactions stabilize high density plasmas, leading to formation of a metastable electron-hole liquid (EHL) phase [12] instead of an exciton state. The equilibrium density of the EHL phase (i.e. the density resulting in the minimum energy per charge) is dependent on the screening of the electron-hole interaction by the polarizable lattice, and usually lies in the range 10^{22}-10^{25} m^{-3} [13]. In ZnO, the EHL density lies towards the upper end of this range: theory has predicted a value ~2×10^{25} m^{-3} [12], although experimental measurements suggest a slightly lower equilibrium density (~1×10^{24} m^{-3} [14]). Exciting the ZnO sample with 266 nm and 400 nm photons (penetration depth l_0~50 nm and 100 μm respectively) allows the excitation of high density (EHL) and low (exciton) density regimes.

To study the formation dynamics in these two regimes it is therefore advantageous to probe using a technique sensitive to both the *disappearance* of free charges and/or the *appearance* of the (bound) exciton state. Due to the distinct responses of free and bound charges [9, 15], THz time domain spectroscopy is ideally suited to follow *both* free and bound charge carriers on a picosecond timescale. In this chapter, we study exciton and EHL formation in single crystal zinc oxide by following the change in the complex conductivity after photoexcitation. By extending previous THz studies on exciton systems to the high density and high temperature regimes, we gain new insight into the behavior of excitonic semiconductors.

The majority of experimental work in this area concerns excitons in quantum wells or quantum dots – see, for example, references [3-9]. In these nanostructures the exciton binding energy is enhanced due to spatial confinement of the electron and hole wavefunctions. The unusually large exciton binding energy of ZnO makes it the ideal sample to study the fundamental properties of excitons, without having to structure the material on the nanometer scale, which inherently introduces defects and/or heterogeneities. In ZnO the exciton state is intrinsically stable, even in a crystalline sample. This offers certain advantages, most notably in reducing the effects of inhomogeneities.

5.2 Experimental details

In our experiments, a 12×8×1 mm ZnO single crystal substrate, (1010)-cut from MaTeK, is held in a closed cycle helium cryostat which allows variation of the crystal temperature in the range 20-300 K. Effects of asymmetry due to excitation and probing along [0001] and [0100] axes are found to be too small to detect in our measurements.

The sample is excited above the absorption gap (E_g=3.43 eV direct band gap) using two-photon excitation, with 400 nm (3.1 eV) 150 fs full width half maximum (FWHM) pulses, or one-photon excitation using 266 nm (4.5 eV) 150 fs FWHM pulses, generating a hot electron-hole gas with >1 eV excess energy in both cases. For two-photon excitation with energies exceeding the band gap ($2\hbar\omega >> E_g$), the non-parabolic bands give rise to efficient two-photon absorption, and a correspondingly small optical penetration depth. In ZnO, the decay of the two-photon excitation power (P) in the propagation direction can be described by $dP/dz = -\beta^{(2)}P^2$, where the two-photon absorption coefficient $\beta^{(2)}$ calculated following [16] is virtually independent of crystal axis. The laser power P typically used in the experiment described here (calculated from the measured fluence, f_l, and pulse duration FWHM 150 fs through $P=f_l/\mathrm{FWHM}$) leads to effectively 100% absorption of the excitation pulse. The excitation density N therefore decays hyperbolically in the z direction over a length scale inversely proportional to P^2. The excitation beam is significantly larger that the region probed by the THz pulse (~5 mm and ~1 mm respectively), such that the Gaussian profile of the excitation pulse can be ignored. With 266 nm excitation single photon absorption occurs, characterized by absorption coefficient $\beta^{(1)}=2\times10^5$ cm^{-1} [17] (corresponding to a penetration depth l_0~50 nm) and an excitation profile described by $dP/dz = -\beta^{(1)}P$. For both 400 nm and 266 nm excitation, we take into account reflective losses of the excitation pulses from the vacuum-sample interface in the calculation of excitation density (see equation 4.8). The excitation density N_0 and the conductivity σ_0 referred to in the following text are the excitation density and conductivity respectively at the sample interface.

It should be noted that, due to uncertainties in measured fluences and calculated absorption coefficients, the spatial decay of the excitation density assumed in the extraction of the conductivity is somewhat approximate. Furthermore, diffusion of carriers is also neglected, which may introduce further errors in assumed charge distributions [18], especially when measuring on long timescales. This systematic error causes inaccuracy in the *magnitudes* of the extracted interface conductivities presented here. However, since we measure the THz wave transmitted through the entire excited region (and the modulation of the THz is proportional to the product of density and penetration depth), the error in the ratio of two measured conductivities is relatively small. Therefore, comparison *between* measured conductivities is still meaningful.

5.3 Low density excitation

In this section, the response of ZnO to low density excitation (with 400 nm absorption) is discussed. In this regime, well below the Mott density, the average distance in-between excitations (r~100 nm) is much larger than the Bohr radius (a_{Bohr}) of the 1S exciton in bulk ZnO (reported to be in the range 18-80 Å [19, 20]). Here, the lowest energy state of the plasma is an exciton gas [21] (see figure 5.1).

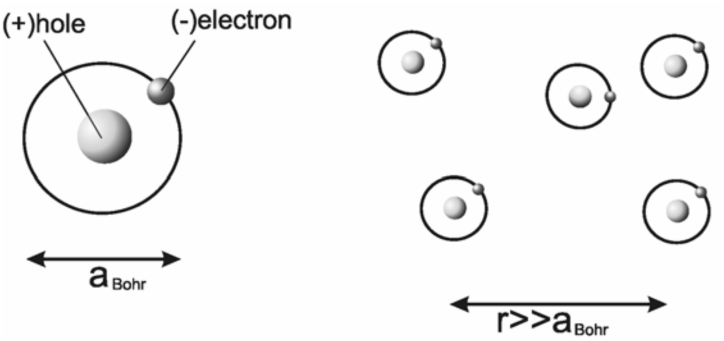

Figure 5.1 Left: a Wannier exciton with Bohr radius a_{Bohr}. Right: an exciton gas below the Mott density, with the average distance between excitations much larger than the Bohr radius of an exciton in ZnO.

The strength of THz-TDS lies in the direct determination of the complex conductivity $\sigma_0(\omega, \tau)$ at different times τ after photoexcitation. Figure 5.2(a) represents the dynamics of the photoconductivity at 0.6 THz ($\sigma_0(\omega$=0.6 THz, τ)), measured at 30 K with excitation fluence of 0.2 J/m^2, corresponding to an excitation density of ~1×10^{21} m^{-3}). After excitation, there is a fast rise (~5 ps, attributed to thermalization and cooling) followed by a decay of around 100 ps. Note that after around 50 ps, the imaginary component of the conductivity switches sign from positive to negative. This sign change corresponds to the *disappearance* of free charges and the *appearance* of the (bound) exciton state: the conductivity of a gas of free charges (described by the Drude model for conductivity) is compared to that for a gas of bound electrons and holes in figure 5.3. The restoring force introduced by the Coulomb interaction between an electron and its corresponding hole results in a shift of the response resonance from effectively zero to a frequency ω_0 (see equation 5.2). At low frequencies (i.e. at frequencies below ω_0), such a resonance causes a sign change in the imaginary component of the conductivity.

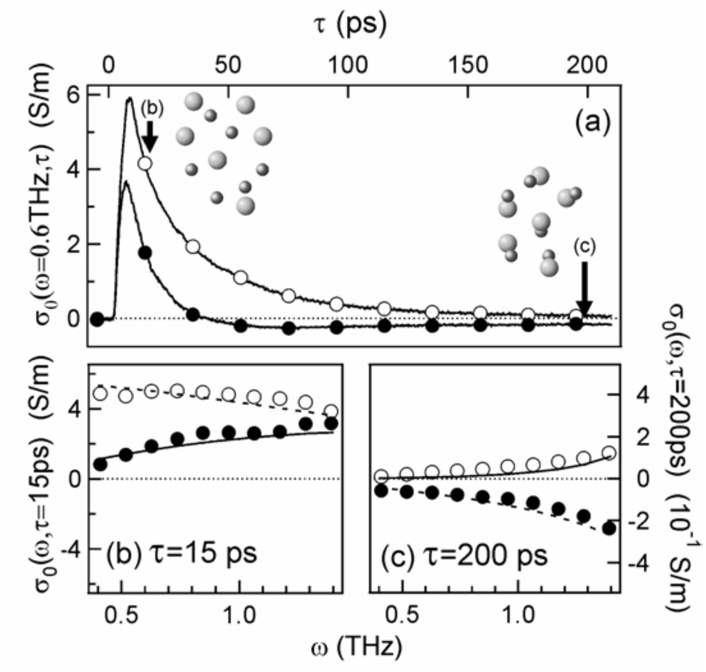

Figure 5.2 Conductivity dynamics in weakly photo-excited ZnO (using 2-photon excitation at 400 nm) at 30 K. (a) The change in the complex conductivity at the peak of the THz signal at 0.6 THz (real and imaginary parts as open and closed circles respectively) as a function of time after excitation. (b) Frequency dependent complex photoconductivity measured 15 ps after excitation. The response is dominated by free electrons and holes, and is reasonably well described by the Drude model (lines). (c) 200 ps after excitation most of the excited electrons and holes have paired to form excitons. The increased correlation of electrons and holes is shown by the sign flip of the imaginary conductivity (see figure 5.3): the lines represent the response expected from the polarizability of the exciton.

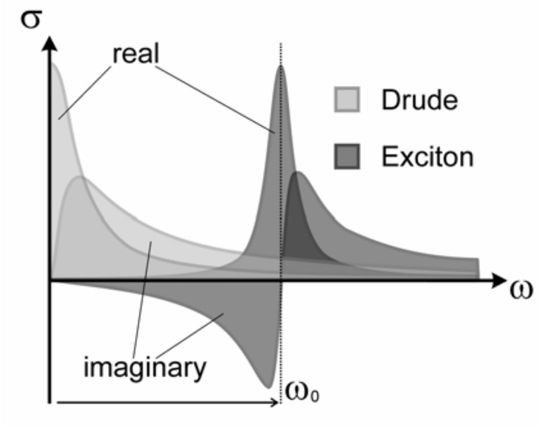

Figure 5.3 Conductivity of a gas of free charges (Drude) compared to that for a gas of bound electrons and holes (Exciton). The restoring force introduced by the Coulomb interaction between electrons and holes results in a shift of the response resonance from effectively zero in the Drude model to a frequency ω_0.

Figure 5.2(b) shows $\sigma_d(\omega, \tau=15\text{ ps})$ measured immediately after carrier cooling (15 ps after excitation), and is characteristic of free charges: the lines represent the Drude model of conductivity with a low scattering time 90 fs (reasonable for single crystalline materials at low temperature (see chapter 4)). Figure 5.2(c) shows $\sigma_d(\omega, \tau=200\text{ ps})$, well (200 ps) after photo-excitation. It should be noted that the imaginary component has switched sign, indicating the presence of a restoring force in the response. This change represents the evolution of a gas of free electrons and holes to a exciton state with bound electrons and holes [9]. The resulting conductivity σ_0 of an exciton under these conditions is given by the Clausius-Mossotti relation [22]

$$\frac{(\varepsilon-1)+{}^{i\sigma_0(\omega)}\!\big/\!_{\omega\varepsilon_0}}{(\varepsilon+2)+{}^{i\sigma_0(\omega)}\!\big/\!_{\omega\varepsilon_0}}=\frac{\varepsilon-1}{\varepsilon+2}+\frac{\alpha(\omega)N_{exc}}{3}, \tag{5.1}$$

where α is the exciton polarizability, N_{exc} the exciton density and $\varepsilon=9$ [1] the low frequency lattice dielectric constant. For Wannier type excitons, since the spatial extent of the exciton is fairly large (at least over several unit cells of the crystal) the effect of the lattice potential can be incorporated into the effective masses of the electron and hole and Wannier excitons have, at least approximately, hydrogen-like solutions to the Schrödinger equation [23]. It should be noted that such a simple model ignores valence band splitting [24]. The contribution to the polarizability of a transition dipole associated with the hydrogen like 1*s* to *np* transitions is given by

$$\alpha_{np}(\omega)=\left(\frac{2}{3}\frac{1}{4\pi\varepsilon_0}\frac{\left|\langle 1s|e\tilde{r}|np\rangle\right|^2}{E_{np}-E_{1s}}\right)\frac{\omega_0{}^2}{\omega_0{}^2-\omega^2-i\gamma_0\omega}, \tag{5.2}$$

where $\langle 1s|$ is the lowest energy state hydrogenic wavefunction, $|np\rangle$ the excited *p* state wavefunction, γ_0 the absorption linewidth, and $\omega_0=(E_{np}-E_{1s})/\hbar$ the transition resonance frequency determined by the energy levels E_{np} and E_{1s} ($\omega_0=8$ THz for the 1s→1p transition). The first part of equation 5.2 calculates the static (DC) dipole associated with an exciton transition, while the second part allows for a Lorentzian resonance lineshape for each transition [25]. The lines in figure 5.2(c) are calculated using equations 5.1 and 5.2, summing over all *p* states, assuming a typical linewidth of $\gamma_0=3$ THz (implying a sub-picosecond lifetime for excited states, common for Wannier excitons [26]) and density $N_{exc}=1.3\times10^{21}\text{ m}^{-3}$. Considering the uncertainty involved in the precise determination of absorbed fluence, the exciton density found from fitting the conductivity compares favorably to the estimated excitation density $N_0\sim1\times10^{21}\text{ m}^{-3}$. This indicates that most of the initially excited electron hole pairs eventually form excitons, while charge trapping and radiative exciton decay occur on longer timescales [27, 28]. The decay of the real conductivity can therefore be attributed to a decay of the photogenerated electron-hole plasma into a stable exciton gas, representing the exciton formation time in ZnO.

5.4 Temperature dependence

Previous THz studies on a confined exciton system at low temperature [9] have revealed similar picosecond formation dynamics as reported here. In this section, we report the *temperature dependence* of exciton formation. The decaying real component of the measured conductivities (scaled to the peak height) are plotted in figure 5.4(a) for different lattice temperatures (excitation fluence of 0.2 J/m^2, corresponding to an estimated initial excitation density ~1×10^{21} m^{-3}).

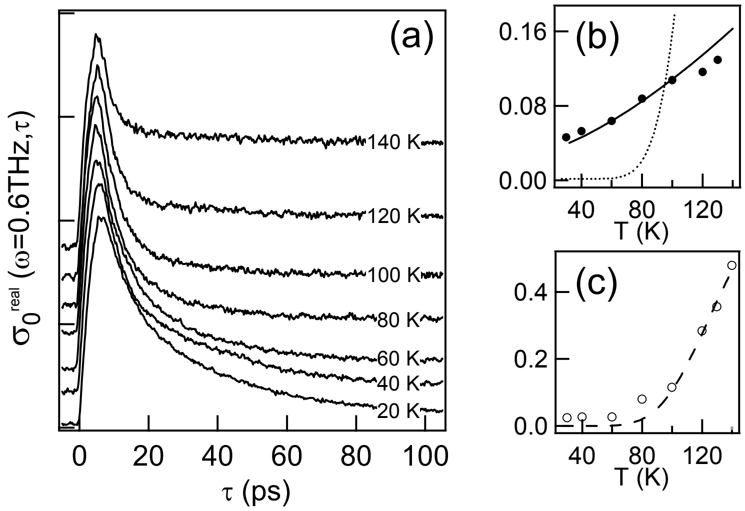

Figure 5.4 (a) Temperature dependence of the exciton formation rate investigated through the decay of the free charge density (shown for initial excitation density ~1×10^{21} m^{-3} and normalized to peak conductivity). (b) The exciton formation rate (in ps^{-1}) increases weakly with temperature. The dotted line displays the dependence expected for formation by optical phonon emission, while the solid line displays the much weaker temperature dependence associated with acoustic phonon emission. (c) The long term dissociated exciton fraction (defined as plateau conductivity divided by peak conductivity) increases with temperature. The dashed line indicates the dissociated expected for a binding energy of 60 meV.

The plasma decay / exciton formation rate increases by a factor of ~2.5 from 20-140K (the maximum rate is plotted, filled circles, as a function of temperature in figure 5.4(b)). This illustrates the importance of (thermally occupied) phonon modes in the exciton formation process: inelastic carrier-phonon scattering allows the excess excitation energy to be dissipated into the lattice [29]. The dotted line displays the temperature dependence expected for longitudinal optical phonon scattering (proportional to $exp(-\hbar\omega_{ph}/kT)$ [30], with ω_{ph}=72 meV [1]) while the solid line represents that for acoustic phonon scattering (proportional to $T^{3/2}$ [31]). It is clear from the relatively weak temperature dependence in the plasma decay rate that acoustic phonon scattering is the rate determining energy loss mechanism.

At higher temperatures, the long time equilibrium free charge density (that measured on the plateau after the initial plasma decay / exciton formation) increases due to thermally mediated exciton dissociation. The temperature dependence of the dissociated fraction (defined here as the magnitude of the plateau conductivity normalized by that at the peak) is displayed in figure 5.4(c). The dashed line shows the dissociation fraction expected for a simple two component equilibrium (here consisting of the bound and free states) with the forward step (dissociation from the bound state) having an activation barrier of 60 meV (the exciton binding energy) [32]. The agreement with the data is surprisingly good considering the crudeness of the approach employed in determining the dissociation fraction.

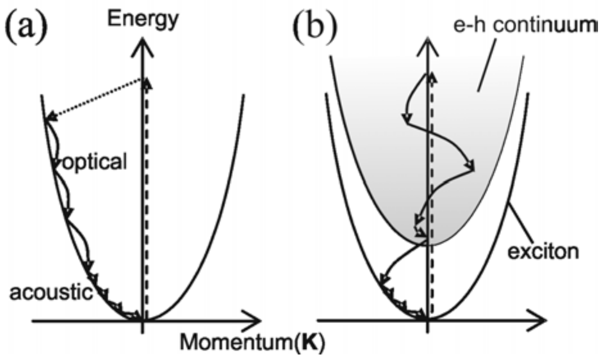

Figure 5.5 Exciton formation illustrated in terms of the “hot exciton cascade”. The parabola represents the exciton kinetic energy as a function of centre of mass momentum (**K**). After initial photon absorption (dashed line), a hot exciton, with **K**≠0, is formed by emission of an optical phonon (dotted line), needed to conserve momentum. Subsequent relaxation to the emissive **K**=0 state occurs through further emission of optical (large curved arrows) and, as the exciton falls to the bottom of the well, acoustic (small curved arrows) phonons. (b) THz measurements (see text) suggest that the motion of electrons and holes remains uncorrelated for much of the cooling process. In this case, a more realistic description involves cooling through the electron hole continuum, where the uncorrelated electron and holes have, on average, no net centre of mass momentum. After the initial cooling process, increased correlation in the motion of electrons and holes leads to a non-zero centre of mass momentum.

While, for a hot electron-hole gas, rapid longitudinal optical (LO) phonon emission is the most important energy loss pathway [33-36], slow acoustic phonon emission has been proposed to explain the slow rise of exciton luminescence (typically ~100 ps [3-5, 29]) within the framework of the "hot exciton cascade" [6] (see figure 5.5(a)). In this picture, photon absorption and subsequent emission of an optical phonon leads to hot exciton formation, with center of mass momentum **K** unequal to zero (**K**≠0). Relaxation to the emissive **K**=0 state occurs through further emission of optical and, closer to the bottom of the exciton potential well, acoustic phonons. Hence, the rate determining step for reaching the **K**=0 state (and thus luminescence) requires the loss of the last few quanta of excess energy. However, the slow decay in the free charge response observed here, similar to that of confined systems [9], suggest the motion of electrons and holes remains uncorrelated for much of the formation process. In this case, a more realistic description involves cooling through the electron hole continuum (see figure 5.5(b)), where the uncorrelated electron and holes have, on average, no net centre of mass momentum. Later in the cooling process, correlated motion between the paired electrons and holes (exciton formation) introduces a non-zero centre of mass momentum.

5.5 High density excitation

While excitons are certainly attractive from a technological viewpoint, they also offer unique possibilities for studying the interaction of quantum particles: In the dilute limit (where the distance between excitons is much larger than the exciton size) excitons behave as bosons. As such, they obey Bose statistics, and it has been postulated that an exciton Bose-Einstein condensate could form at low temperatures [21]. In the high density limit screening of the coulomb attraction prevents the binding of electron-hole pairs, and the insulating exciton gas undergoes a transition to a conducting Fermi electron-hole liquid (EHL) phase [12, 21, 37].

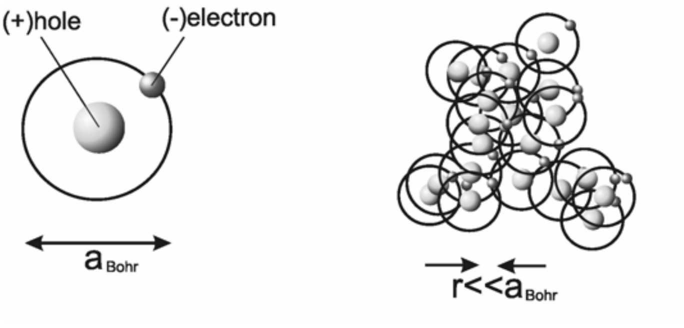

Figure 5.6 Left: Wannier exciton with Bohr radius a_{Bohr}. Right: a semiconductor excited above the Mott transition, with the average distance between excitations much smaller than the Bohr radius.

The equilibrium density of the EHL phase (i.e. the density resulting in the minimum energy per charge) is dependent on the screening of the electron-hole interaction by the polarizable lattice, and usually lies in the range 10^{22}-10^{25} m^{-3} [13]. In ZnO, the EHL density lies towards the upper end of this range: theory has predicted a value of 2×10^{25} m^{-3} [12], although experimental measurements suggest a slightly lower equilibrium density (~1×10^{24} m^{-3} [14]) in better agreement with our findings.

Since its excitation density can be easily varied with pump fluence, an excitonic semiconductor is a simple system to study this crossover from Bose to Fermi statistics. Exciting the ZnO sample with 266 nm photons instead of 400 nm photons generates a much higher excitation density (owing to the penetration depth l_0~50 nm compared to l_0~100 μm for 400 nm). This allows the study of dynamics in both the high (EHL) and low (exciton) density regimes. In the dilute excitation limit, excitons are formed via a two-step process: first thermalization and cooling of the hot electron-hole gas occurs, followed by relaxation to the bound exciton state. In the high density limit the exciton state is destabilized, and an insulating exciton gas will undergo the transition to a conducting plasma [21]. Due to multi-particle interactions one could imagine that the resulting high density plasma is unstable, and eventually a low density exciton gas is formed through recombinative processes.

In this section, we study the decay of a hot electron-hole plasma in single crystal zinc oxide, a direct band-gap semiconductor with high exciton binding energy [1]. Exciting the material below the Mott transition, we observe slow exciton formation, consistent with formation mediated by acoustic phonon emission. At excitation densities above the Mott density of ZnO we observe a rapid decay (~5 ps) of the electron-hole plasma. After the initial fast decay, a stable plasma state is reached which persists even on the nanosecond timescale, consistent with the formation of a stable electron-hole liquid. The electron-hole density of this stable state appears to be independent of excitation density.

At high excitation densities, the peak modulation of the THz is sub-linear with fluence, indicating that charge-charge interaction effects are present. In this non-linear regime, the estimation of the charge distribution [18] and the extraction of the complex conductivity [38] are not exact.

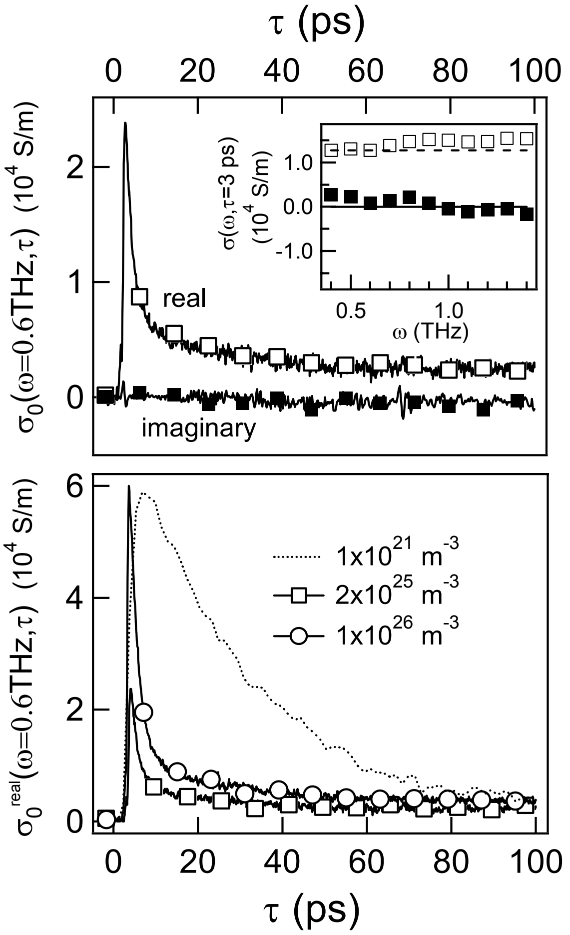

Figure 5.7 Conductivity dynamics for high excitation densities, measured at 20 K. Upper panel: The open (real) and closed (imaginary) squares show the fast conductivity dynamics for direct 266 nm photon excitation with initial density ~2×10^{25} m^{-3} (well above the Mott density ~3×10^{23} m^{-3}). Inset: the conductivity measured 3 ps after excitation. Lower panel: Decay of the real component for different excitation densities (for comparison the plasma decay caused by exciton formation, measured at low excitation density, is shown as a dotted line). The circles show the dynamics measured for initial density of ~1×10^{26} m^{-3}: it is clear that, while both measurements show similar fast decays, the magnitude of the signal on long times is only very weakly density dependent.

The extracted conductivity for 266 nm excitation fluence of 1.5 J/m^2, corresponding to an estimated excitation density ~2×10^{25} m^{-3} (appreciably larger than the Mott density of ZnO: calculated to be 3×10^{23} m^{-3} at 85 K, and only weakly temperature dependent, following refs. [10, 11]), is presented in the upper panel of figure 5.7. The conductivity measured at 0.6 THz is plotted as a function of time after excitation (the conductivity is observed to be frequency independent). While the imaginary conductivity is observed to be virtually zero at all pump-probe times, the real component decays to a plateau within around 20 ps.

The conductivity at both short and long times following photoexcitation is predominantly real, indicating that, at all times following photoexcitation, charges are not bound (i.e. we do *not* decay to an insulating exciton state). At these high densities, both band filling and electron-hole scattering serve to decrease the electron (and hole) momentum relaxation times (see section 4.7), such that the frequency dependence of the complex conductivity is expected to be different from that at low density, and resulting in a flat response in the probed frequency range (see inset of figure 5.7). The lines in the inset of figure 5.7 show the flat conductivity expected within the Drude model for a scattering time approaching zero.

The long time component of the conductivity persists even for nanosecond delay times. The initial decay, however, is much faster than the exciton formation dynamics observed at low excitation density (plotted as a dotted line in the lower panel of figure 5.7). By comparing the magnitude of the conductivity on longer times to that measured at the peak, we estimate that the plasma reaches a stable density at ~2×10^{24} m^{-3}. Further, the final, apparently stable density is only very weakly dependent on the initial excitation density, even when the initial excitation is increased by a factor of five (see open circles in the lower panel of figure 5.7).

One could imagine that the lowest energy state of the photo-excited sample could be a high density gas of excitons, with a near close packed density (i.e. close to the Mott density, ~3×10^{23} m^{-3} [10, 11]). The stable state we observe in the lower panel of figure 5.8 is characterized by significant *real* conductivity, indicating that this state is not composed of insulating excitons, but is a *conducting* state. This shows the formation of a metastable electron-hole liquid (EHL) phase [12], with an equilibrium density ~2×10^{24} m^{-3}. In ZnO, theory has predicted an EHL density of 2×10^{25} m^{-3} [12], although experimental measurements suggest a slightly lower equilibrium density (~1×10^{24} m^{-3} [14]), in better agreement with our findings.

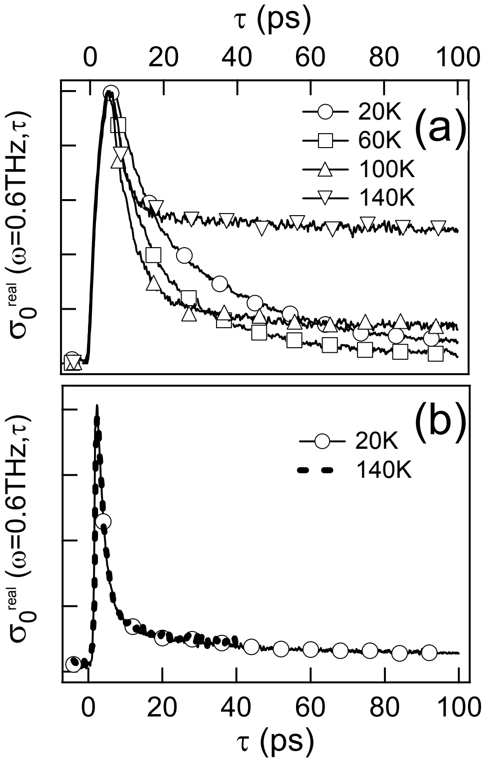

Figure 5.8 Temperature dependence of decaying conductivity (normalized to peak conductivity) for excitation density (a) ~1×10^{21} m^{-3} and (b) ~1×10^{26} m^{-3}. While exciton formation at low densities is strongly temperature dependent, as both the initially excited plasma and the exciton gas interact strongly with the phonons of the lattice, the plasma decay in at high densities is essentially independent of lattice temperature.

We are the first to report the extremely rapid formation dynamics of such an EHL state after intense photoexctiation. These fast dynamics are somewhat surprising, especially considering the excited plasma has a >1 eV excess energy. Indeed, the very fast dynamics measured here, faster than cooling observed for a low density plasma (indicated by the rise of the dotted line in figure 5.7) suggest that the liquid phase can form directly from the hot plasma. This process, which involves many-body (Auger) recombination of hot charges, shows up in the broad photo-emission spectrum of ZnO under high density excitation [39], which decays on a timescale similar to the decay of the THz conductivity [40]. In contrast, formation of the EHL phase in silicon, which is an indirect semiconductor, is three orders of magnitude slower [41] than reported here for ZnO. This in itself demonstrates that the formation process in ZnO is predominantly radiative.

It has been suggested that strong electron-hole interaction in ZnO, which allows for the stabilization of such a high density EHL, diminishes the role of phonon coupling in the liquid formation process [12]. In practice, this effectively means that charge-charge interactions are screened by the optical dielectric function. This picture is indeed corroborated by a complete lack of any temperature dependence in the high density dynamics: in figure 5.8 we plot the temperature dependence of the plasma decay for excitation densities ~1×10^{21} m^{-3} (a) and ~1×10^{26} m^{-3} (b). While exciton formation in (a) is strongly temperature dependent, as the both the initially excited plasma and the exciton gas interact strongly with the phonons of the lattice, the plasma decay in (b) is independent of lattice temperature within experimental resolution.

5.6 Conclusions

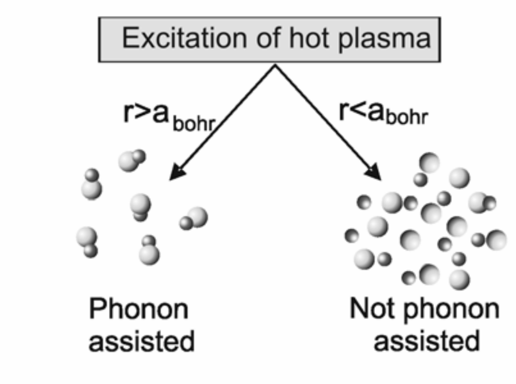

Figure 5.9 The plasma dynamics following excitation are strongly dependent on the excitation density. Below the Mott density (with average distance between excitations $r>a_{Bohr}$) an exciton gas forms. Above the Mott density ($r<a_{Bohr}$), the plasma forms an electron-hole liquid.

Photo-exciting a direct semiconductor such as ZnO generates hot electrons in the conduction band and hot holes in the valence band. The subsequent decay of this plasma is dependent on its density: when the average distance (r) between excitations is much larger than the Bohr radius (a_{Bohr}) the plasma decays to an exciton gas, with bound electron-hole pairs. This process is phonon mediated, and therefore faster for higher temperatures. At high excitation densities, when $r< a_{Bohr}$, an exciton gas does not form, but the excited plasma decays (through many body radiative recombination) to an electron-hole liquid (EHL) phase. This process is very fast, occurring while the plasma is still "hot". In contrast to exciton formation, EHL formation is not phonon mediated, and is essentially independent of lattice temperature.

References

[1] E. O'Kane, Phys. Rev. B **18**, 6849 (1978).
[2] M. Zamfirescu, et al., Phys. Rev. B **65**, 161205 (2002).
[3] P. W. M. Blom, et al., Phys. Rev. Lett. **71**, 3878 (1993).
[4] T. C. Damen, et al., Phys. Rev. B **42**, 7434 (1990).
[5] H. Kalt, et al., Phys. Stat. Sol. B **206**, 103 (1998).
[6] D. Kovalev, et al., Phys. Rev. B **54**, 2518 (1996).
[7] D. S. Chemla and J. Shah, Nature **411**, 549 (2001).
[8] J. Szczytko, et al., Phys. Rev. Lett. **93** (2004).
[9] R. A. Kaindl, et al., Nature **423**, 734 (2003).
[10] F. J. Rogers, et al., Phys. Rev. A **1**, 1577 (1970).
[11] J. Collet and T. Amand, Phys. Rev. B **33**, 4129 (1986).
[12] G. Beni and T. M. Rice, Phys. Rev. B **18**, 768 (1978).
[13] C. D. Jeffries and L. V. Reldysh, *Electron-Hole Droplets in Semiconductors* (North-Holland, Amsterdam, 1983).
[14] T. Skettrup, Solid State Commun. **23**, 741 (1977).
[15] E. Hendry, et al., Phys. Rev. Lett. **92**, 196601 (2004).
[16] I. M. Catalano, et al., Phys. Rev. B **33**, 7270 (1986).
[17] G. E. Jellison and L. A. Boatner, Phys. Rev. B **58**, 3586 (1998).
[18] The conductivity extraction analysis presented in section 3.4 neglects effects of charge diffusion in-between excitation and the arrival of the THz probe at time τ. This can be a severe approximation when the penetration depth l_0 is much smaller than the mean free path of the excited charges. An indication of the strength of such diffusive effects is given by the characteristic diffusion length l_{dif} and the characteristic ballistic path length l_{bol}. Due to the small scattering times τ_r observed in ZnO (τ_r<<1 ps from the observation of no significant imaginary component to the THz conductivity – see figure 5.7) and large band gap, l_{dif} and l_{bol} are expected to be orders of magnitude smaller in ZnO than in silicon (see Ref. [37] in chapter 4), and significantly smaller than the penetration depth l_0~ 50 nm for the times (in the picosecond range) after excitation reported here. Hence, the assumption that the charge distribution does not change significantly in-between pump and probe times is reasonable, particularly on short (<100 ps) timescales.
[19] M. Shim and P. Guyot-Sionnest, J. Am. Chem. Soc. **123**, 11651 (2001).
[20] S. M. Zhou, et al., Phys. Stat. Sol. A **202**, 405 (2005).
[21] C. W. Lai, et al., Science **303**, 503 (2004).
[22] P. W. Atkins, in *Physical Chemistry* (5th edition, Oxford University Press, Oxford, 1990), p. 650.
[23] D. F. Blossey, Phys. Rev. B **3**, 1382 (1971).
[24] A. Teke, et al., Phys. Rev. B **70**, 195207 (2004).
[25] For ZnO, the THz photon energies (1 THz=4 meV) are below the energy level spacing of the exciton, so that the exciton response at THz frequencies is dominated by the DC polarizability ~80 000 Å^3, giving rise to the predominantly imaginary conductivity observed in figure 5.2(c). The resonance at ω_0=8 THz, with a linewidth γ_0=3 THz, which describes the broadening of exciton levels, accounts for the observed small real contribution to the conductivity.
[26] R. Riera, et al., phys. stat. sol. B **207**, 393 (1998).
[27] D. C. Reynalds, et al., J. Appl. Phys. **88**, 2152 (2000).
[28] S. B. Zhang, et al., Phys. Rev. B **63**, 075205 (2001).
[29] P. E. Selbmann, et al., Phys. Rev. B **54**, 4660 (1996).
[30] F. E. Low and D. Pines, Phys. Rev. **98**, 414 (1955).
[31] J. Bardeen and W. Shockley, Phys. Rev. **80**, 72 (1950).
[32] In equilibrium, the dissociation and recombination rates, k_{dis} and k_{rec}, are related through $k_{dis}N_{exc}=k_{rec}N_{free}$, where N_{exc} and N_{free} are the exciton free charge densities respectively. The dissociated fraction, as defined in text, is given by $N_{free}/(N_{free}+N_{exc})=1/(1+k_{rec}/k_{dis})= 1/(1+A\mathrm{e}^{E/kT})$, where E=60 meV is the exciton binding energy and A is a fitting parameter.
[33] J. R. Goldman and J. A. Prybyla, Phys. Rev. Lett. **72**, 1364 (1994).
[34] H. Lobentanzer, et al., Phys. Rev. B **39**, 5234 (1989).
[35] M. Mehendale, et al., Appl. Phys. Lett. **71**, 1089 (1997).
[36] J. F. Ryan, et al., Phys. Rev. Lett. **53**, 1841 (1984).
[37] M. Nagai, et al., Phys. Rev. Lett. **86**, 5795 (2001).

[38] Strictly speaking, equation 3.6 (the separation of the complex conductivity into a product of frequency and spatially varying functions) does not hold. For the excitation discussed in this section (where an electron's response is expected to be dependent on the density of surrounding charges – see section 4.7), we measure the THz wave transmitted through the entire excited region, and the extracted conductivity gives an indication of the *average* frequency response over the spatially inhomogeneous excitation volume..

[39] T. J. Inagaki and M. Aihara, Phys. Rev. B **65**, 205204 (2002).

[40] T. Takeda, Phys. Stat. Sol. B **229**, 877 (2002).

[41] J. Shah and A. H. Dayem, Phys. Rev. Lett. **37**, 861 (1976).

Chapter 6

Exciton cooling in CdSe quantum dots

6.1 Background

Semiconductor quantum dots (QDs) have unique optical properties owing to the confinement of the electron and hole wave functions, giving rise to discrete energy levels [1]. In QDs in which confinement effects are considered strong [7], the energy level of the electron and hole state can be considered to be independent: the lowest energy exciton state is written $1S_{3/2}1S_e$, with $1S_{3/2}$ and $1S_e$ representing the lowest energy hole and electron levels respectively [7] (see figure 6.1). Through the particle dimensions, the precise energies of these discrete levels can be changed, and absorption and luminescence properties can be varied at will. This means QDs offer unique possibilities in optoelectronic applications such as light emitting diodes [2], solar cells [3, 4] and nanocrystal lasers [5].

For QD applications in solar cells, a key aspect is the step immediately following photo-excitation: the cooling of the photo-generated hot electron and hot hole to their lowest energy states [6]. Whereas in bulk semiconductors, rapid, sequential emission of phonon quanta results in fast cooling, in QDs the absence of a continuum of states means that energy transfer from the carriers to the lattice must occur in discrete steps. As the spacing between the electronic levels (hundreds of meV) is large compared to the LO phonon frequency (~25 meV), electron cooling via electron-phonon coupling requires the simultaneous emission of a large quantity of phonons, a process of low probability. Hence, it has been proposed that hot electron cooling in QDs is hindered by a so-called "phonon bottleneck", resulting in cooling times in the nanosecond range [8]. Such slow cooling properties could prove useful in solar cells [6] as slow cooling would allow the harvesting of the photon energy in excess of the band gap, nearly doubling the theoretical efficiency of a QD solar cell compared to a bulk semiconductor (silicon) device [6].

However, in CdSe (a II-VI semiconductor) QDs, the observation of extremely fast sub-picosecond electron relaxation [9-13] indicates the existence of mechanisms that allow the phonon bottleneck to be bypassed. Indeed, in small QDs, electron cooling has been reported [14] that is even faster than that for an electron in the bulk material. This counterintuitive result has been explained by an enhancement of Auger electron-hole interaction [10, 11, 13, 15, 16] which allows efficient transfer of energy from the electron to the hole, circumventing the phonon bottleneck for electron cooling in the presence of a hole. Hole relaxation is thought to be relatively efficient because of the large density of hole states [9]. Other explanations for rapid electron cooling have been proposed, including fast multi-phonon relaxation [17] and polaron effects [18]. However, slowing of electron dynamics by an order of magnitude when the hole is passivated through trapping [11, 13] suggests that the Auger effect is likely dominant for electron cooling in CdSe. Moreover, when more than one electron-hole pair (exciton) is present in a QD, it has been unequivocally demonstrated that relaxation occurs through Auger processes, in which energy is efficiently transferred between the different carriers. The inverse Auger process – impact ionization – has recently also been reported in QDs [10].

For a QD containing just one electron-hole pair, theory has indeed predicted efficient electron-hole coupling, with typical timescales on which electron-hole energy transfer occurs in the range from 500 fs [15] to 2 ps [16], though this has yet to be experimentally quantified. Most experimental studies to date have concentrated on the dynamics of the electron cooling through optical transient absorption (OTA) measurements [9, 14, 19-21]. However, transitions in the optical regime correspond to interband transitions and are per definition determined by the dynamics of both electrons and holes. There have been some efforts [11, 13] to study *intraband* electronic transitions which lie in the infrared. However, the lower energy hole transitions (which lie in the far-infrared [7]) are much more difficult to access with sufficient time resolution, and there have been no investigations to date on the dynamics of hole intraband transitions in CdSe QDs. A direct and independent determination of electron and hole cooling rates in single exciton QDs, which is required to unequivocally verify the Auger cooling mechanism and obtain information about electron-hole coupling times, has therefore remained elusive.

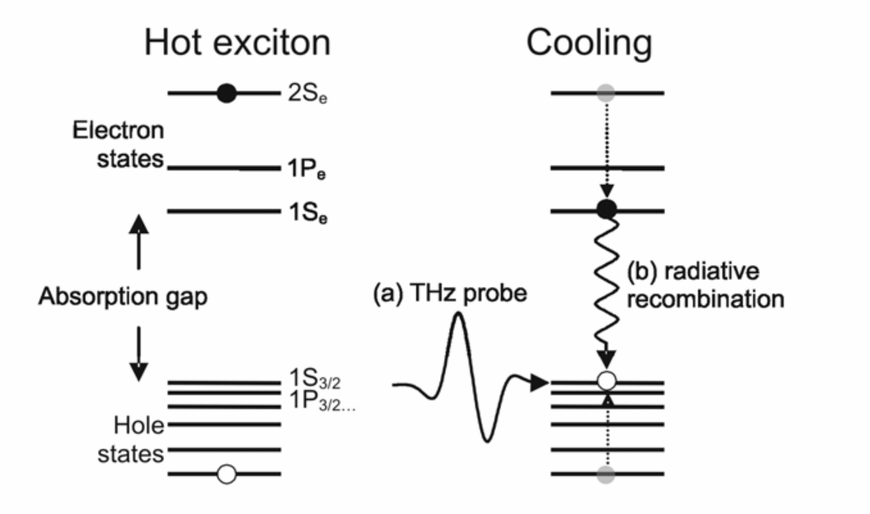

Figure 6.1 Left: discrete energy levels of a QD. Right: Excitation by the QD with 3.15 eV photons generates a distribution of hot electron and hole states. Cooling (dashed arrows) eventually results in electrons and holes decaying to their lowest energy $1S_{3/2}1S_e$ state. (a) THz pulses, $E_{THz}(t,\tau)$, are used to probe the hole population of the $1S_{3/2}$ level as a function of pump-THz probe delay τ. (b) Luminescence up-conversion is used to monitor the population of the $1S_{3/2}1S_e$ state, determined by the combined electron and hole cooling rates.

Figure 6.1 represents the experimental concept we propose to unambiguously determine electron *and* hole cooling dynamics using a combination of Terahertz time-domain spectroscopy (THz-TDS) [23-25] and luminescence up-conversion. The THz frequency range is sufficiently low that the response is dominated by hole transitions, and can be used to probe the hole $1S_{3/2}$ (cold) state population [25]. Combining this novel technique with femtosecond time-resolved PL measurements (which probe both electron and hole cold state populations) allows unambiguous separation of the electron and hole contributions to cooling.

In this section, THz-TDS and time resolved luminescence measurements on well-defined CdSe QD ensembles are presented. Our results constitute explicit proof of Auger assisted cooling for electrons, bypassing the phonon bottleneck. We obtain the first direct evidence of electron to hole energy transfer in CdSe QDs, and the first quantitative measurements of electron-hole coupling times.

6.2 Experimental details

For the present study, CdSe colloidal QDs were synthesized by hot injection of precursors into a coordinating solvent mixture, following the method reported by de Mello Donegá et al. [26]. This method allows the preparation of high-quality organically capped CdSe nanocrystals, with very few surface defects, resulting in high band-edge photoluminescence quantum yields and no defect related luminescence. Furthermore, the nanocrystal diameter (*d*) can be tuned from 1.7 to 15 nm, yielding ensembles with a very small size polydispersity (4-10%), without any post-preparative treatment. Briefly, the preparation consists on quickly injecting a solution of trioctylphosphine (TOP, 10 mL) containing Se (0.79 g) and $Cd(Me)_2$ (0.28 g) into a hot (300°C) coordinating solvent mixture (20 g of trioctylphosphineoxide, TOPO, and 10 g of Hexadecylamine, HDA). The reaction mixture is then stabilized at the growth temperature (240°C) and the nanocrystals are allowed to grow, yielding CdSe QDs with diameters ranging from 2.7 to 3.9 nm, depending on the growth duration (15 – 90 min). To prepare CdSe QDs larger than 3.9 nm additional precursors are slowly added while keeping the growth temperature at 240°C. Nanocrystals smaller than 2.7 nm require a modified procedure, with lower injection (100°C) and growth temperatures (150-200°C, depending on the desired size). Moreover, the nucleation and growth steps are carried out in different coordinating solvents. Nucleation is achieved by injecting a precursor solution (0.79 g Se and 0.87 g $Cd(Me)_2$ in 10 mL TOP) into 10 mL 2M TOP-Se at 100°C followed by dilution with 10 mL TOP at room temperature. This process yields a solution of 1.2 nm CdSe nanocrystals in TOP, which are subsequently grown to either 1.7 nm in TOP/dodecylamine at 150°C or to 1.9 – 2.5 nm in TOPO/HDA/TOP at temperatures between 150°C and 210°C. Synthesis and sample preparation were carried out in a glove box under Argon (less than 5 ppm O_2 and H_2O). The samples were characterized by measuring the photoluminescence and absorption spectra and photoluminescence quantum yields on diluted solutions (optical density ≤ 0.1 at the emission maximum, 0.2-0.4 at 400 nm). Nanocrystal diameter was obtained from the first exciton absorption peak by using an empirical calibration curve correlating the exciton peak energy with the nanocrystal size. This curve was constructed from experimental data published by several independent groups [27-31]. To test the reliability of the size estimates based on our calibration curve and to obtain information regarding size polydispersity the nanocrystal sizes of several samples were also determined by transmission electron microscopy (TEM). The TEM sizes are in good agreement (*i.e.* ±10%) with the values estimated from the exciton absorption peaks. Samples for the THz time-domain spectroscopy and time resolved up-conversion photoluminescence measurements were prepared by dissolving the crude reaction product in anhydrous hexane to yield CdSe concentrations in the mM range (0.5 – 7 mM, depending on the size). A blank sample containing only the ligands was also investigated, and found not to contribute to either the luminescence or THz-TDS signals.

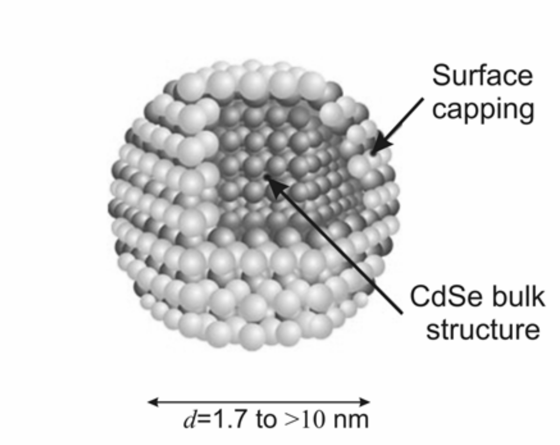

Figure 6.2 Schematic representation of a quantum dot of diameter d. The samples synthesized for the present study are monodispersed (d±10 %), with few defects (illustrated by their high quantum efficiencies). The surfaces are passivated by capping with TOPO-TOP-HDA.

E_{abs} (eV)	d (nm)	E_{em} (eV)	FWHM (meV)	σ (%)	QE (%)
2.70	1.7	2.59	150	<5	15
2.45	2.5	2.34	142	<5	32
2.31	3.0	2.21	220	10	30
2.25	3.2	2.16	136	<5	-
2.14	3.9	2.08	168	8	90
2.10	4.3	2.05	83	4	55
2.05	5.0	1.99	117	10	60
2.03	5.2	1.95	123	<10	-
1.94	6.4	1.89	123	<10	30
1.72	>10	1.70	250	-	-

Table 6.1 Optical properties of the QD ensembles: E_{abs}=energy of peak absorption, d=mean diameter, E_{em}=energy of peak emission, FWHM=full width half maximum of emission spectrum and σ= size distribution.

The resulting low-defect QD samples have low size dispersion (~5%, somewhat larger for larger particles – see table 6.1) with QD size varying from a mean diameter (*d*) of 1.7 nm to d>10 nm. Carriers generated in the latter are expected to have bulk-like properties. The samples, passivated by capping with TOPO-TOP-HAD (see figure 6.2), consist of high purity QDs with high luminescence quantum yields (also listed in table 6.1). The measured dynamics were found to be intrinsic to the QDs, and independent of solution in hexane or toluene. In both experiments, the 400 nm excitation fluence of 2 Jm^{-2} is sufficiently low to ensure a maximum of one exciton per QD. This is corroborated by the lack of fluence dependence of the measured dynamics. All experiments were carried out at room temperature (~300 K).

6.3 THz-TDS measurements

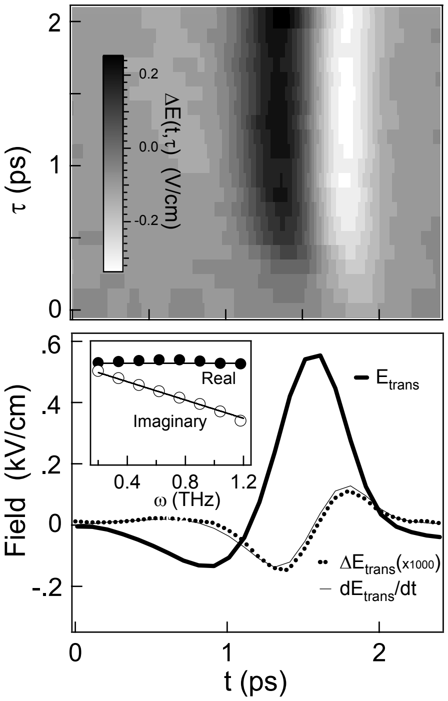

Figure 6.3 Upper panel: THz modulation ΔE of 3.2 nm QDs as a function of optical pump - THz probe delay time τ and THz sampling time t, for the THz field E_{trans} depicted in the lower panel (thick solid line). Lower panel: the THz modulation (dotted line) measured at τ=2 ps is simply proportional to the derivative of the driving field (thin solid line), indicating a phase shift of the THz pulse. Inset: the extracted conductivity for such a response is purely imaginary.

Hole cooling is investigated using THz-TDS. Exciting the QD samples with 400 nm (3.15 eV) photons leads to a distribution of hot electron and hole states. THz-TDS uses single cycle oscillations of a weak electromagnetic field (~1 kV/cm) $E_{trans}(t,\tau)$, measured directly in the time domain t (see figure 6.3), to probe changes in material response in the frequency range 0-2 THz [23], following photo-excitation at time τ. This frequency range corresponds to energies (1THz= 4meV) smaller than the energy level spacing in our QDs, and the signal is determined the non-resonant response of the intraband transitions (i.e. by the exciton polarizability). It was verified that the change in complex photoconductivity is indeed purely imaginary (see inset of figure 6.3), corresponding to a photo-excited phase shift of the THz pulse. Due to the small energy spacing of the hole levels compared to those of the lighter electron, the hole response dominates the signal, in particular its lowest energy $1S_{3/2}$ (cold) state polarizability [25, 33].

6.4 THz and luminescence rise times

Since the temporal shift of the THz field on photoexcitation is predominantly due to the polarizability of the $1S_{3/2}$ hole level, we can follow the hole cooling to the $1S_{3/2}$ state by directly measuring the phase shift of the THz pulse. The right panel of figure 6.4(a) plots the phase shift of the THz field as a function of time after excitation, for several QD diameters. The traces have been measured at the time of the probe THz field with maximum gradient (indicated by an arrow in the left hand panel of figure 6.4(a)).

Information about the combined electron and hole cooling rates are obtained from the time evolution of luminescence from the $1S_{3/2}1S_e$ state at the peak of the luminescence spectrum shown in the left panel of figure 6.4(b), investigated with fs luminescence up-conversion (see section 2.6). The luminescence signal is proportional to the product of hole and electron 1S populations. The results are plotted in the right hand panel of figure 6.4(b).

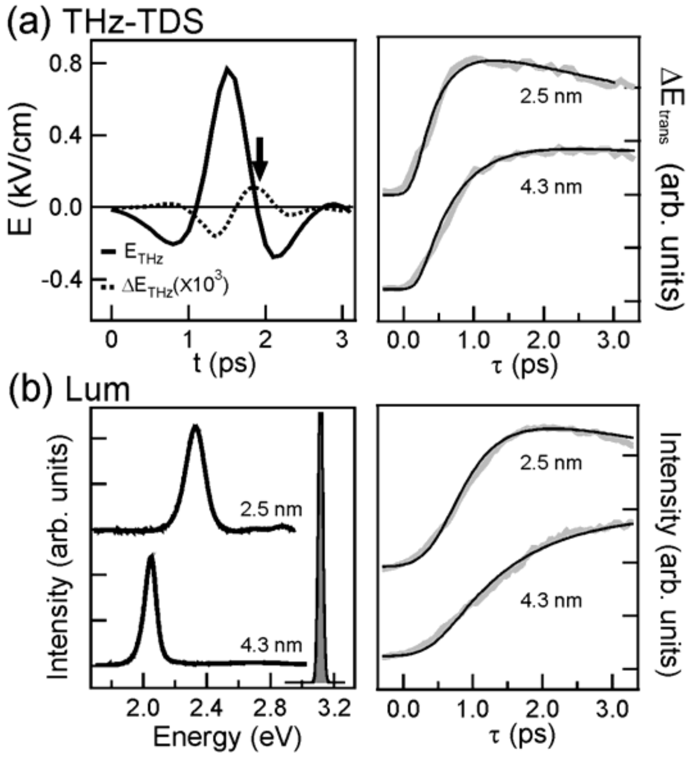

Figure 6.4 (a) LEFT: The THz field strength transmitted through a QD sample (3.9 nm, solid line) and photo-induced modulation after 2 ps (dotted line). RIGHT: The temporal phase shift of the THz field on photoexcitation is measured at the time marked with an arrow in the left panel, as a function of pump-probe delay, τ. This signal gives the transient hole population of the $1S_{3/2}$ level (see text). (b) LEFT: Luminescence spectrum. Also shown is the excitation pulse (shaded). RIGHT: We measure the increase in intensity as a function of delay τ at the peak luminescence spectrum (grey lines). The dynamics in both (a) and (b) are adequately described by exponential rise times determined by the carrier cooling rates (black lines in the right hand panels).

The dynamics in figure 6.4 can be adequately described by a convolution between a measurement response, $G(\tau)$ (a Gaussian function with FWHM~215 and 560 fs for THz and luminescence, see ref [34]) and an exponential rise described by a time constant τ_{rise}:

$$\int_0^\infty N_0 \frac{\tau_{decay}}{\tau_{decay}-\tau_{rise}}\left(e^{-\tau/\tau_{decay}}-e^{-\tau/\tau_{rise}}\right)G(\tau'-\tau)d\tau' \tag{6.1}$$

A decay term (τ_{decay}) is included for generality, as some hole trapping occurs in the smaller particles [25]. The results of the fits are plotted as black lines in the right panels of figure 6.4. The extracted rise times are plotted as a function of QD diameter d in figure 6.5. The hole cooling rate corresponds to τ_{rise} from the THz measurements, and the combined hole and electron rate by the luminescence τ_{rise}.

For QDs with d<3.3 nm, the combined luminescence rate follows the THz hole cooling rate very closely (~0.3 ps). For d>3.3 nm there is a clear slowing of the luminescence rise (to approximately 1.2 ps) compared to THz-TDS (~0.5 ps), indicating that electron cooling determines the delayed luminescence in larger particles.

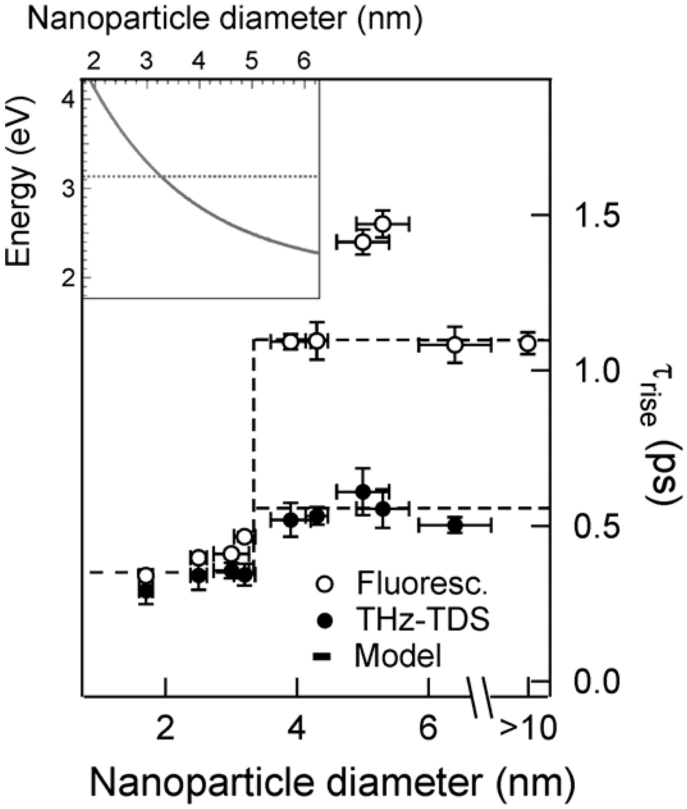

Figure 6.5 Rise (cooling) times obtained from exponential fits to the THz-TDS and luminescence measurements as a function of mean particle diameter (horizontal error bars indicate size distributions). Dashed lines are the result of the model described in section 6.6. Inset: Line indicates the energy of the $1P_{3/2}1P_e$ transition (the lowest energy transition allowing hot electron generation) calculated from ref. [1]. The horizontal dotted line signifies the excitation energy used in the experiment. The dark and light grey regions indicate particle diameters for which (given the excitation energy) hot and cold electrons respectively are photo-generated – i.e. only for diameters d>3.3 nm must electron (as well as hole) cooling be considered, marking a clear step in the luminescence and THz rise times.

6.5 Electron and hole cooling times

These results can be understood by considering the energy of the $1P_{3/2}1P_e$ transition (the lowest energy allowed transition for which hot electrons are photo-generated), shown in the inset of figure 6.5, following the calculations of Norris and Bawendi [1], given the fixed excitation energy used in the experiments (horizontal dotted line). It is clear the step in the experimental data in figure 6.5 coincides (at d=3.3 nm) with the onset of excitation of the electron into the hot $1P_e$ state. This means that for d<3.3 nm the electron is always excited into its cold state, and hole cooling is responsible for the delayed rise of both the luminescence and THz signals. For d>3.3 nm, the luminescence signal rise slows down, owing to electron relaxation from the $1P_e$ to the $1S_e$ state. The 1.2 ps electron cooling is in good agreement with previous reports [9-13].

Remarkably, the *hole* cooling rate also slows down for d>3.3 nm, despite the fact that the hole itself has *less* excess energy when the electron is excited to the $1P_e$ rather than the $1S_e$ state (comparing e.g. d=3.2 and 3.9 nm). This observation is stressed in figure 6.6, which shows hole cooling times inferred from THz data as a function of hole excess energy, for electronic excitation into the cold $1S_e$ and hot $1P_e$ states.

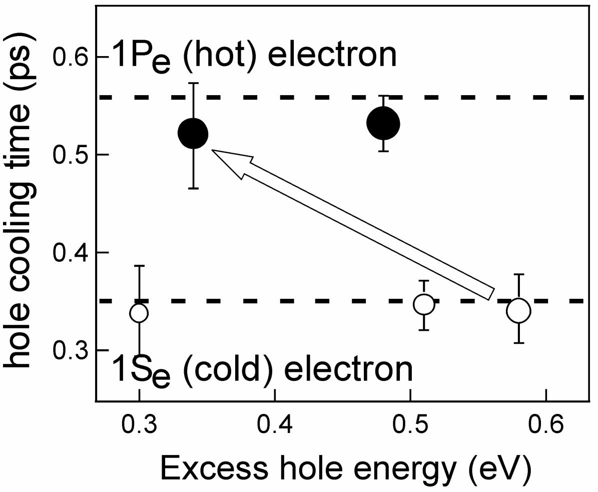

Figure 6.6 Hole cooling time as a function of hole excess energy (calculated from ref. [1]), for CdSe QDs with diameters proportional to the symbol size (2.5, 3.0, 3.2, 3.9 and 4.3 nm, respectively). Filled symbols denote particles for which the electronic hot state is optically accessible with the 3.15 eV excitation pulse; open symbols are those for which the electron is excited into its cold state. Clearly, hole cooling slows down considerably with the electron in the hot state. Dashed lines are the result of the model described in section 6.6.

These observations allow for two conclusions: firstly, electron cooling in small QDs is clearly comparable to bulk cooling (indicated by the luminescence rise of the sample with *d*>10 nm), corroborating that a mechanism is available in which the phonon bottleneck is bypassed. Secondly, the observation of delayed hole cooling upon higher electronic excitation directly reveals that this mechanism entails energy transfer from electrons to holes (the holes get re-excited upon electron cooling, resulting in an apparent slowing down of hole cooling), and is the first direct confirmation of the Auger cooling mechanism [15][16]. A common prediction of both references [15] and [16] is that electron-hole coupling is only weakly dependent on QD diameter. This is consistent with our observations: for *d*>3.3 nm the luminescence rise experiences a very modest size dependence. An additional small increase (~0.25 ps) in the luminescence rise time for *d* between 4.5 and 5 nm indicates that electron cooling from higher lying excited states down to the $1P_e$ state is much faster than the $1P_e \rightarrow 1S_e$ decay assigned to the step at *d*=3.3 nm. The sample with *d*=6.4 nm cools at a similar rate to the bulk-like *d*>10 nm sample.

6.6 Cooling model

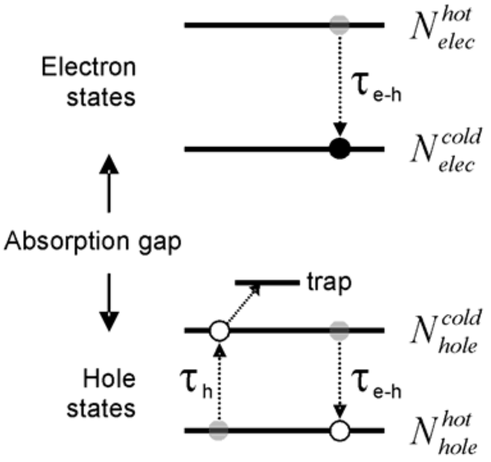

Figure 6.7 Five-level model for Auger cooling in QDs. The time dependent probabilities (*N*) of occupying each level are given by equations 6.2-6.5, with τ_h the hole cooling time, and $\tau_{e\text{-}h}$ the electron-hole coupling time. To be able to describe the experimental data on longer timescales, a term accounting for hole trapping (τ_{decay}) is included.

To establish that the step in the hole cooling around *d*=3.3 nm can be quantitatively accounted for by electron to hole energy transfer, we have modeled the system with a five-level calculation. Hot electron and hole states are represented by one level each (time dependent probabilities of occupation N_{elec}^{hot} and N_{hole}^{hot} respectively), as are the cold states (occupation N_{elec}^{cold} and N_{hole}^{cold}), with the fifth level constituting the unexcited QD – see figure 6.7. For *d*<3.3 nm, only cold electrons are produced upon photo-excitation, along with hot holes. Relaxation of hot holes (hole cooling time τ_h) leads to population of the cold state, for which slower hole trapping (described by time τ_{decay}) is included for generality [25]. For *d*>3.3 nm, hot electrons are also produced, and electron relaxation is accompanied by the generation of hot holes (being the hypothesis behind the Auger cooling mechanism). This process is described by the electron-hole coupling time $\tau_{e\text{-}h}$. The system is then described by the four coupled equations:

$$\frac{\partial N_{elec}^{hot}}{\partial t} = -\frac{1}{\tau_{e-h}} N_{elec}^{hot} \begin{cases} +0, d < 3.3 \text{ nm} \\ +\delta(t), d > 3.3 \text{ nm} \end{cases}, \tag{6.2}$$

$$\frac{\partial N_{elec}^{cold}}{\partial t} = \frac{1}{\tau_{e-h}} N_{elec}^{cold} \begin{cases} +\delta(t), d < 3.3 \text{ nm} \\ +0, d > 3.3 \text{ nm} \end{cases}, \tag{6.3}$$

$$\frac{\partial N_{hole}^{hot}}{\partial t} = -\frac{1}{\tau_h} N_{hole}^{hot} + \frac{1}{\tau_{e-h}} N_{elec}^{hot} + \delta(t), \tag{6.4}$$

$$\frac{\partial N_{hole}^{cold}}{\partial t} = \frac{1}{\tau_h} N_{hole}^{hot} - \frac{1}{\tau_{e-h}} N_{elec}^{hot} - \frac{1}{\tau_{decay}} N_{hole}^{cold}, \tag{6.5}$$

where the functions $\delta(t)$ describe occupation of the relevant electron and hole state at time *t*=0. The calculated signals (proportional to N_{hole}^{cold} (THz) and $N_{elec}^{cold} \times N_{hole}^{cold}$ (luminescence)), can then be simulated, by taking into account broadening due to the finite resolution of the measurements, through

$$\int_0^\infty N_{hole}^{cold}(\tau) G_{THz}(\tau' - \tau) d\tau', \tag{6.6}$$

$$\int_0^\infty N_{elec}^{cold}(\tau) N_{hole}^{cold}(\tau) G_{lum}(\tau' - \tau) d\tau'. \tag{6.7}$$

Numerical solution to this model fully reproduces all observed transients for d< 4.5 nm (the diameter at which states higher than $1P_e$ are excited) with hole cooling and electron-hole coupling times of 330±50 fs and 1±0.15 ps, respectively – see figure 6.8. This second value lies between theoretical estimates of the electron-hole coupling time of 0.5 ps [15] and 2 ps [16] for the $1P_e \rightarrow 1S_e$ electronic transition in CdSe QDs.

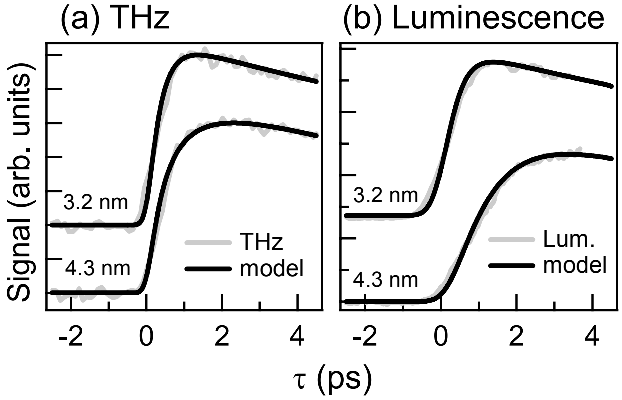

Figure 6.8 Fits (black lines) to the experimental data (grey lines) assuming the five level model described in text, shown for two QD diameters either side of the transition at *d*=3.3 nm (see figure 6.5).

The dynamics reproduced by this simple model reproduce the data surprisingly well. The simulations can be approximated very well using equation 6.1 – i.e. have near exponential dynamics – and the derived exponential times are shown as dashed lines in figures 6.5 and 6.6. Clearly, the increase in hole cooling time for *d*>3.3 nm can be fully accounted for by electron to hole energy transfer.

6.7 Conclusions

By combining THz-TDS and luminescence up-conversion we are able to completely map the cooling processes for both the electron and the hole in CdSe quantum dots of various diameters. We find efficient, Auger-assisted electron cooling and make the first quantitative measurement of the electron-hole coupling time. The observed fast cooling for both the electron and the hole has important implications for the application of QDs in 'hot carrier' photovoltaic devices. Harvesting carriers before cooling will require either extremely rapid, sub-picosecond charge collection, or the suppression of Auger effects through hole trapping and/or designing QDs with similarly large electron and hole level spacing.

References

[1] D. J. Norris and M. G. Bawendi, Phys. Rev. B **53**, 16338 (1996).
[2] V. L. Colvin, et al., Nature **370**, 354 (1994).
[3] W. U. Huynh, et al., Science **295**, 2425 (2002).
[4] E. W. McFarland and J. Tang, Nature **421**, 616 (2003).
[5] V. I. Klimov, J. Phys. Chem. B **104**, 6112 (2000).
[6] A. J. Nozik, Annu. Rev. Phys. Chem. **52**, 193 (2001).
[7] A. L. Efros and M. Rosen, Annu. Rev. Mater. Sci. **30**, 475 (2000).
[8] K. Brunner, et al., Phys. Rev. Lett. **69**, 3216 (1992).
[9] V. I. Klimov and D. W. McBranch, Phys. Rev. Lett. **80**, 4028 (1998).
[10] V. I. Klimov, et al., Science **287**, 1011 (2000).
[11] V. I. Klimov, et al., Phys. Rev. B **61**, R13349 (2000).
[12] P. Yu, et al., Nano Lett. **4**, 1089 (2004).
[13] P. Guyot-Sionnest, et al., Phys. Rev. B **60**, R2181 (1999).
[14] V. I. Klimov, et al., Phys. Rev. B **60**, 13740 (1999).
[15] L. W. Wang, et al., Phys. Rev. Lett **91**, 056404 (2003).
[16] A. L. Efros, et al., Sol. Stat. Comm. **93**, 281 (1995).
[17] P. C. Sercel, Phys. Rev. B **51**, 14532 (1995).
[18] S. Sauvage, et al., Phys. Rev. Lett **88**, 177402 (2002).
[19] U. Woggon, et al., Phys. rev. B **54**, 17681 (1996).
[20] J. Z. Xu, et al., Prog. Nat. Science **12**, 729 (2002).
[21] C. Burda, et al., J. Phys. Chem. B **105**, 12286 (2001).
[22] S. Xu, et al., Phys. Rev. B **65**, 045319 (2002).
[23] M. C. Beard, et al., J. Phys. Chem. B **106**, 7146 (2002).
[24] E. Hendry, et al., Phys. Rev. Lett. **92**, 196601 (2004).
[25] F. Wang, et al., submitted to Phys. Rev. Lett. (2005).
[26] C. d. M. Donegá, et al., J. Phys. Chem. B **107**, 489 (2003).
[27] C. B. Murray, et al., J. Am. Chem. Soc. **115**, 8706 (1993).
[28] M. Jacobsohn and U. Banin, J. Phys. Chem. B **104**, 1 (2000).
[29] V. N. Soloviev, et al., J. Am. Chem. Soc. **115**, 8706 (2000).
[30] X. Peng, et al., J. Am. Chem. Soc. **120**, 5343 (1998).
[31] W. W. Yu, et al., Chem. Mater. **15**, 2854 (2003).
[32] C. de Mello Donegá, et al., J. Phys. Chem. B **107**, 489 (2003).
[33] A very rough estimate for the polarizability (α) of states in a QD can be obtained by considering simple particle in a box type solutions to the Schrödinger equation [ψ_n, with eigen energy E_n, see: (see: S.V. Gaponenko, Optical Properties of Semiconductor Nanocrystals (Cambridge University Press, 1998))] by summing over all transition polarizabilities for each final state through $\alpha = 1/(6\pi\varepsilon_0)\left|\langle\psi_{initial}\left|e\tilde{r}\right|\psi_{final}\rangle\right|^2/(E_{final} - E_{initial})$. From this we estimate hole polarizabilities three orders of magnitude larger than those for electron states. The lowest energy hole 1S state contributes a factor nine times more to the polarizability than the 1P state. See ref. [25] for more accurate calculations.
[34] The function $G(\tau)$ describing the broadening of the THz rise in figure 6.4(a) depends on both the time dependent excitation density, the THz probe field, and the material photoconductivity – see section 3.6. We estimate the response time of 215 fs using equation 3.18 for our known THz pulse shape and excitation pulse width (150 fs), assuming a completely imaginary conductivity in our probed frequency range, as plotted in the inset of figure 6.3. The response function of the luminescence measurement is much simpler, independently determined by auto-correlation of the laser pulse.

Chapter 7

Charge generation in conjugated polymers

7.1 Background

A conjugated polymer is an organic semiconductor in which all π electronic states are occupied and π^* states empty (see figure 1.11). In these materials, photons with energies exceeding the energy gap can be absorbed leading to the population of π^* states, much like the photo occupation of the conduction band in an inorganic semiconductor. As a consequence, organic semiconductors have many of the properties associated with their inorganic counterparts: due to the delocalization of the π bands, absorption of light triggers electrical conduction [1] (a property which can be utilized to make polymer solar cells [2, 3]), while charge injection can result in intense luminescence. Despite their apparent similarity to inorganic semiconductors, there are, however, obvious differences. For example, measured zero frequency mobilities of polarons in polymers are orders of magnitude lower than in conventional inorganic semiconductors [4]. Moreover, the zero frequency mobility increases with temperature [5], while mobility in inorganic semiconductors tends to decrease with temperature [6].

Despite their limited conductivity, the mechanical flexibility of conjugated semiconducting polymers means they are increasingly finding applications in opto-electronic devices such as light-emitting diodes (LEDs) and solar cells [7]. However, many of the fundamental aspects of the photo-excitation process in these materials have remained the subject of intense debate. One of the key remaining questions [8-11] is whether, initially upon photoexcitation, excitons or free polarons are primarily formed. In the band picture, excitation with photons of energy greater than the band gap initially forms a polaron gas, which may subsequently decay to lower energy exciton states. However, it has been suggested that a molecular exciton picture [12] is more relevant for polymers. In this model, absorption of a photon generates a hot exciton, which may dissociate into polarons after migration to defects [13], by absorption of a second photon [14] or by bimolecular exciton-exciton annihilation [15]. Whether the band picture or the exciton model is more appropriate to describe the photoexcitation process in polymers depends on the electron-hole binding energy, i.e. whether excitons may be described as Wannier or Frenkel type. Reports of the exciton binding energies in polymers span a huge range: from 20 meV [1, 16] to more than 1 eV [17]. Hence, while the observation of significant photoconductivity [1] demonstrates the presence of conducting charges, it is unclear whether carriers are generated directly on ultrafast timescales or produced on longer timescales through exciton dissociation mechanisms.

In actual polymer samples, the π bands are not very well defined, as defects in the carbon chain cause the overlap of atomic orbitals to be broken. The conducting properties are determined by the quantity known as the *conjugation length* (defined as the number of continuous defect free polymer units). One key issue is therefore the effect of polymer morphology on charge and energy transfer (an excellent review is provided in [18]). The sample morphology also determines to what extent the polymer chains constituting the sample can interact. Such interchain interactions can result in charge transfer between polymer strands, which is essential to charge transport across macroscopic distances, as the length of one polymer strand is limited [18]. Indeed, it has been suggested that interchain charge transport limits the overall charge mobility [19], by noting that mobility within one single chain is much higher than over an entire amorphous film [20]. For excitons, delocalization over different chains is adverse to the use of these materials in electroluminescent devices, as interchain excitons are intrinsically weakly emissive [21].

It has been proposed that up to 90% of the excitations in thin film samples result in interchain species [22, 23], with the largest part of the electron and hole wavefunctions residing on separate polymer chains, though this is certainly controversial [18, 24]. Theoretical modeling has recently shown that interchain effects are particularly important in close packed polymer crystals [25]. In reality, film samples are generally amorphous and disordered, as the large polymer molecules are very difficult to crystallize. This leads to a structure with a large variance in chain-chain distances [26] (see figure 7.1(a)), with only a small fraction of the polymer chain length ‘close’ to neighboring chains. Hence, solid polymer films are largely somewhere in-between close-packed crystalline samples and solutions, where the polymer chains are, on average, far enough apart to be considered isolated (shown in figure 7.1(b)).

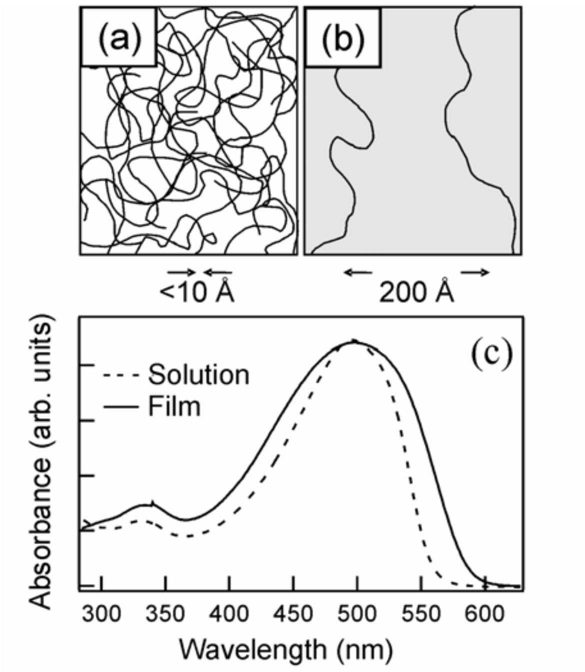

Figure 7.1 Pictorial representation of sample morphology for (a) film and (b) benzene solution samples. In the film, the nearest neighbor chain distance can be as small as 4 Å [27]. Comparison between the two samples allows the study of interchain effects on the photophysics of these materials. (c) Normalized UV-VIS absorption spectra for a solution and a film sample. The broader absorption of the film sample suggests a more disordered state.

As a result of these considerations, the role of the morphology on the semiconducting polymer's optical, electrical and electro-optic properties has been the subject of many studies, see e.g. Refs. [18, 28-30]. Many such studies make use of the change in optical transitions upon changing the polymer morphology. Indeed, the UV-VIS spectra of benzene solution and thin film samples are very different (see figure 7.1(c)). Here, the broadened absorption of the film sample suggests that the thin film phase is more disordered than the solution [31]. Indeed, the strong interaction with "good" solvents such as benzene, allows the polymer to adopt an open, extended chain conformation in solution [32]. As a result of interchain interactions, the polymer fluorescence can also be redshifted; the exciton energy levels are lowered when the exciton becomes increasingly delocalized. Ultrafast time-domain studies have provided additional insights into morphological effects on dynamical processes after photoexcitation, e.g. by comparing the excited state absorption dynamics to the fluorescence decay [33], and variations in photoluminescence [34]. It has also been demonstrated, however, that such optical studies may be complicated by the fact that different types of excitons and charges may have very similar spectral signatures [34-38]. THz time domain spectroscopy (THz-TDS) complements optical studies, as it allows one to *directly* probe both exciton and free charge species simultaneously: it is sensitive to the real *and* imaginary components of frequency-dependant photoconductivity, and as such, can monitor free *and* bound charges on a sub-picosecond timescale.

In this section, we use THz-TDS to follow the sub-picosecond excitation process in two phases of the model semiconducting polymer poly[2-methoxy-5-(2'ethyl-hexyloxy)-1,4-phenylene vinylene] (MEH-PPV). In solution the polymer concentration is sufficiently low, and the solvation (in benzene) is sufficiently strong [39], so that we can study this process on essentially isolated polymer chains. In the thin film phase interchain interactions are present [18, 21, 23, 26, 27, 34, 40]. On short (sub-picosecond) times, only a small number (<1%) of free charges is generated in the solid film, while this number is even smaller (by approximately two orders of magnitude) in solution. On longer timescales (> 5 ps) mobile charges are not observed and the photo-induced changes in the THz waveform are mainly due to the polarizability of excitons. Furthermore, in the film sample the restricted motion of the polymer chains, and the stronger effect of torsional disorder, limit the exciton size and reduce the exciton polarizability by a factor of three. The possible effects of interchain species [18, 21, 27, 30, 34] on the observed excitation properties are discussed.

7.2 Experimental details

MEH-PPV films of ~20 μm thickness are prepared by drop casting the polymer from a benzene solution onto water-free quartz plates, using dry polymer from Sigma Aldrich. Films produced in this manner have average chain-chain distances <10 Å [27]. All measurements on film samples are performed under vacuum (<10^{-3} mbar) and the excitation spot continuously moved to impede photo-oxidation and steady state heating. Solution samples are made in water free benzene of concentration 2.6 g/l (corresponding to an average chain-chain separation ~200 Å). Benzene was chosen as it is transparent to THz radiation and is a good solvent for MEH-PPV [39]. Photo-oxidation of the polymer in solution is abated by using a quartz flow cell. Photoexcitation is accomplished with 400 nm (3 eV), 150 fs full width half maximum (FWHM) laser pulses, allowing excitation above the absorption gap of MEH-PPV, which is located at 2.5 eV [41]. Unless stated otherwise, the measurements presented here were performed at room temperature (~300 K) with the maximum excitation fluence of 60 Jm^{-2}. An essentially linear dependence on excitation fluence is observed (see section 7.5).

The THz set-up is described in section 2.2. The field strength $E(t)$ transmitted through the sample is measured directly in the time domain, through electro-optical sampling with

800 nm, 150 fs pulses: this "gating" technique allows a time resolution better than the THz pulse duration [42], permitting the study of the transient photoconductivity in these materials with sub-picosecond temporal resolution, and allowing us to probe the excitation process in real time [43]. Following optical excitation, we measure the pump-induced modulation $\Delta E(t,\tau)$ [42, 44] (plotted in the lower panel of figure 7.3 for the solution sample) of the transmitted THz field (plotted in the upper panel of figure 7.3) as a function of delay τ between pump and THz probe-pulses. In figure 7.3, $\tau=0$ is chosen to be the pump-probe delay where a modulated signal is first observed. At all delays the modulation is <1% of the weak incident THz electric field (peak field ~1 kV/cm). It should be noted that these fields are much lower than the MV/cm fields typically used in devices, so that our THz pulse acts as a true probe pulse, not perturbing the system.

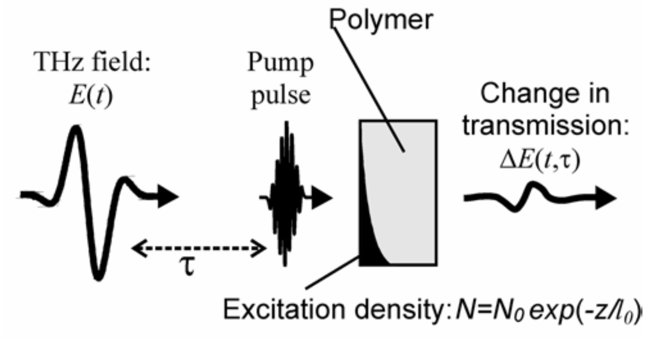

Figure 7.2 The measurement involves obtaining the pump-induced change in transmission, $\Delta E(t,\tau)$, as a function of delay τ between pump pulse and THz probe field $E(t)$. The 400 nm excitation results in a exponentially decaying density $N(z)$ in the samples, characterized by a skin depth l_0~3 mm in solution and ~100 nm in the film [45].

The transient THz transmission of MEH-PPV shows two distinct decays – the cut of the two dimensional data at $t=1.2$ ps is shown as a solid line in figure 7.4. After an initial fast rise (<0.3 ps, limited by the time resolution of the measurement and consistent with previous reports [46]), the signal decays rapidly (similar for both solution and film samples, and independent of excitation fluence), described fairly well by an exponential decay with time constant 0.9± 0.2 ps. The very weak remaining signal decays on a much lower timescale, with a time constant of ~100 ps and ~300 ps for solution and film samples respectively. These photo-excited changes in THz transmission are attributed to electronic excited states of the polymer, as thermal heating effects are estimated to be orders of magnitude smaller: from a thermo-optical coefficient of 10^{-4} K^{-1} (typical for polymer films [47]) an estimated maximum pump-induced temperature increase of 100 K would cause a modulation <0.001%, much lower than the noise level of the experiment.

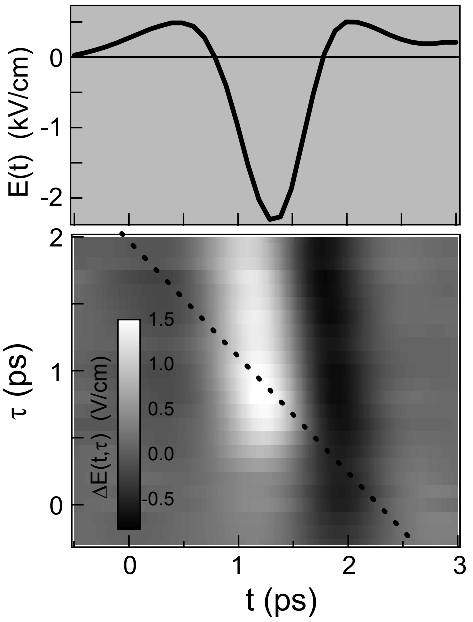

Figure 7.3 A measurement taken on the solution sample: $E(t)$ – upper panel – is the transmitted THz field, with FWHM~1 ps. The lower plot presents the excitation-induced modulation $\Delta E(t,\tau)$ of the THz probe field at delay τ. There is a decrease in magnitude of $\Delta E(t,\tau)$ as function of τ, indicating a decrease in conductivity with pump-probe delay. There is also a shift to the left of the modulation waveform, becoming more like the derivative of $E(t)$ in the upper panel. This occurs as the imaginary component of the conductivity becomes more dominant (see figure 7.7(a)). The dotted line at a 45° angle represents the path of the pump pulse in the measurement, i.e. each point in a horizontal cross section $\Delta E(t,\tau)$ has a different pump-probe delay. Since the temporal decay of the signal is on the order of the FWHM of the THz probe pulse, this must be taken into account in the analysis (see section 3.5). Transforming the data along this line introduces an alternative parameter τ' to describe the time between the excitation pulse and all points on the probe THz pulse with same pump-delay.

Similar fast dynamics have been observed in transient absorption (TA) and stimulated emission measurements [22, 24, 48] on MEH-PPV and similar derivatives. Indeed, we have performed TA measurements on our samples, probing with 800 nm pulses (using the set-up described in section 2.6), and observe comparable decay kinetics: the dotted line in figure 7.4 shows the transient change in transmitted probe 800 nm intensity, after exciting with a 400 nm pulse. The response at 800 nm has, however, been attributed to both exciton transitions [48] and free charge absorption [37], so unambiguous determination of species with this experiment alone is not possible.

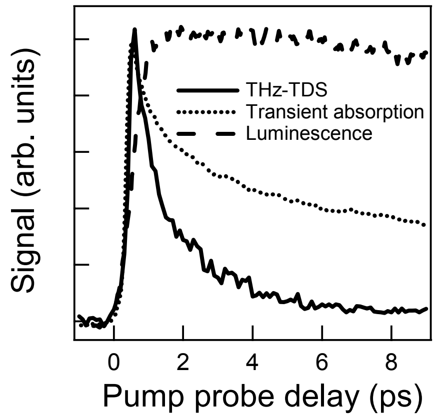

Figure 7.4 Dynamics of THz field modulation (full line, measured at the peak of the THz pulse at *t*=1.2 ps), transient absorption intensity (dotted line, measured with 800 nm probe pulse) and luminescence intensity (up-converted with 800 nm pulse), after excitation with a 400 nm excitation pulse. Signals have been normalized to peak height.

Figure 7.4 also shows the transient luminescence intensity (specifically, the luminescence intensity at 600 nm (at the band edge) up-converted by a delayed 800 nm pulse – set-up described in section 2.6), after excitation with a similar 400 nm fluence as used in both THz and TA measurements. The luminescence signal is measured on a different laser set-up with lower time resolution, leading to a broadening of the 300 fs rise time reported by Hayes et al [49] for luminescence of a similar MEH-PPV sample. Clearly, no fast decay dynamics are observable in the luminescence data. The decay of the luminescence intensity is fluence dependent (faster for higher fluence), but typically ~100 ps and 300 ps for film and solution samples respectively for a similar excitation fluence as in both THz and TA measurements. The luminescence has been assigned to decay of the radiative exciton state, and our observed decay rate is comparable to published values [49, 50].

From their vastly different dynamics, it is clear that luminescence and TA measurements are sensitive to different photo-excited species, and cannot themselves provide a full characterization of the photophysics of conjugated polymers. Photoconductivity measurements [51] meanwhile, which can probe free charge populations directly, lack the time resolution to study ultrafast photoexcitation processes. In contrast to conventional transient-absorption studies, in which only the amplitude of the probe beam is recorded, in THz studies both the amplitude *and* the phase of the THz field $E(t)$ are determined, and allows for the extraction of both the real *and* imaginary parts of the *complex* conductivity. This permits the simultaneous detection of free *and* bound (exciton) charges.

Using THz-TDS, we can investigate the transient complex photoconductivity of a photo-excited sample through the photo-induced modulation in the transmitted probe THz field (see chapter 3). Local field effects considered for porous TiO_2 in section 4.8 are not expected to play an important role in determining the global conductivity: a perfect polymer chain can be thought of as homogeneous along the carbon-carbon backbone, the direction in which we expect the maximum contribution to conductivity, and inhomogeneity will only be introduced by defects. Further, the low dielectric function and conductivity of a polymer means that screening of the applied electric field is expected to be a relatively minor effect – see equation 4.12. Indeed, in contrast to the measured conductivities on porous TiO_2, an essentially linear dependence of signal on pump fluence is observed (see figure 7.10), while the frequency dependence of the measured conductivities does not change on increasing the density. In the extraction of conductivities discussed in later sections, the samples have therefore been treated as homogeneous, described by *average* dielectric functions of 2.5 [41] and 3.1 [52] (i.e. that of benzene) for thin film and solution samples respectively.

7.3 Short-time conductivity: free charges

The results for sub-picosecond conductivities (at $\tau' = 0.5$ ps) extracted using the procedure presented in section 3.5 are shown in figures 7.5(a) and 7.5(b) for solution and film samples respectively. A consequence of the extraction analysis, which takes into account the spatially varying excitation density, is that the extracted conductivities $\sigma(z)$ are also a varying function of spatial coordinate z. For a meaningful comparison between the different samples, we therefore discuss the conductivity at the interface σ_0 normalized to the density of absorbed photons at the sample interface, defined as σ_0/N_0. This quantity allows for a convenient and meaningful comparison between the conductivities in two samples with very different extinction coefficients (characterized by penetration depths of l_0~3 mm and 100 nm [45] for solution and film samples respectively). For a fluence of 60 Jm^{-2}, the maximum fluence used in these experiments, N_0 is estimated (see equation 4.8) from l_0 and the absorbed fluence (40 Jm^{-2}) to be 2.7×10^{22} m^{-3} for the solution and 8×10^{26} m^{-3} for the film.

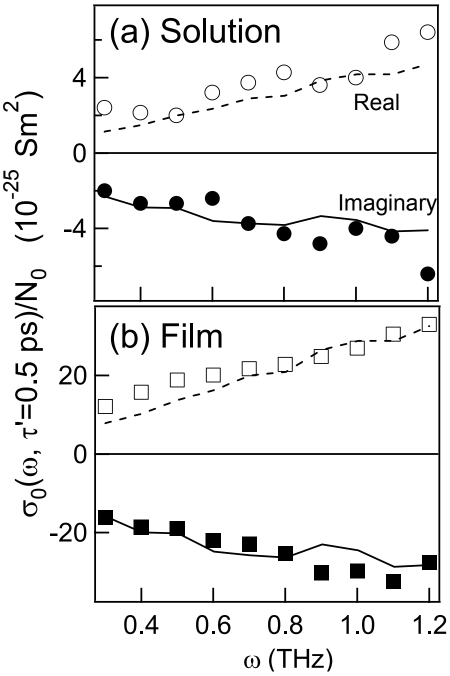

Figure 7.5 (a) The frequency-dependent complex conductivity at the solution interface, normalized to initial surface excitation density – see text – measured in solution 0.5 ps after excitation. The measured conductivity has the characteristics associated with dispersive transport of free charges: significant real and imaginary parts, both increasing with frequency. The lines show the expected conductivity for a free charge, simulated following the formalism in Ref. [53]. The best fit comes from a quantum efficiency $\phi=0.5\times10^{-6}$, indicating that only a very small fraction of excitons dissociates into free charges on such short timescales. (b) The lines show the same simulation with $\phi=3\times10^{-6}$, indicating that the close proximity of neighboring chains in the film sample facilitates exciton dissociation.

The short-time conductivity has the same basic characteristics in both samples: significant contributions of real and imaginary parts to the conductivity, both increasing with frequency. The observation of a large real component to the conductivity indicates that charges are relatively free to respond to the probe THz field (i.e. binding energy < 1 THz, or 4 meV). Here, charge carriers have a velocity in phase with the THz field (or, equivalently, dissipate energy from the THz field into the sample). The observed frequency dependence of the conductivity is characteristic of dispersive free charge transport in a disordered medium, where localization caused by the disorder in the material structure causes non-Drude behavior [43]. Indeed, the frequency dependence of the complex conductivity can be reproduced by a model of disorder-limited hole transport along the polymer chains, using the formalism introduced in Ref. [53] (plotted as lines in figures 7.5(a) and 7.5(b)). This model is based on the tight-binding approximation combined with static torsional disorder – deviations from planar alignment of the carbon chain – determining the effective conjugation length of the polymer. The scaled result for complex *hole* conductivity is plotted as lines in figure 7.5. Our measurement is the sum of electron *and* hole conductivities. We expect the contributions to be similar, as they are limited by the same conformational restraints. Indeed, electron and hole conductivities measured at 34 GHz are comparable [20]. According to Martens *et al.* [54], the much lower electron mobilities observed in time-of-flight experiments or admittance spectroscopy may be traced to extrinsic effects such as trapping of electrons by impurities or structural defects. In figure 7.5 it is clear that the simulation reproduces the key characteristics of our measured conductivity: Substantial real *and* imaginary parts increasing with frequency. This implies that conductivity on the fast timescale is dominated by *free* charges. These are generated promptly on the timescale of our experiment – i.e. within the first 300 fs.

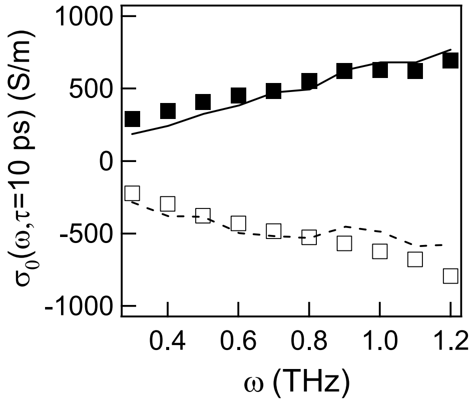

Figure 7.6 The complex conductivity measured 10 ps after photoexcitation on an MEH-PPV/PCBM blended sample, demonstrating the response for thermalized hole charges. The lines represent the simulated conductivity for a density 8.0×10^{21} m^{-3}.

Species generated by excitation with 400 nm (3 eV) light have an initial excess energy of approximately 0.5 eV above the absorption gap of MEH-PPV [9]. These 'hot' species may respond to the THz field differently from thermalized carriers, to which the discussion above applies. However, we also measured the conductivity of MEH-PPV film containing 50% by mass PCBM (1-(3-methoxycarbonyl)-propyl-1-phenyl-(6,6)C_{61}, an exciton-dissociating electron scavenger), resulting in an order of magnitude larger conductivity which persists even on nanosecond timescales. Figure 7.6 depicts the conductivity 10 ps after photoexcitation (after cooling) revealing the conductivity of thermalized holes. The lines represent the model introduced above with a density 8.0×10^{21} m^{-3}. The similarity of the frequency dependences in figures 7.5(b) and 7.6 strongly suggests we are looking at cool charge carriers in *both* cases, since we would expect a very different conductivity for hot and cool charges – a non-thermal charge would be able to overcome many of the energy barriers that determine the simulated conductivity from reference [53].

By comparing the conductivity in figures 7.5(a) and 7.5(b) it is clear that the free charge signal in solution is *smaller* than in the film by almost an order of magnitude. This implies that the product of quantum efficiency of charge generation (ϕ) and mobility (μ) is smaller in solution. If, to begin with, we make the rather naïve assumption that the charge mobility is identical in both materials, we can compare the data and the simulation by varying only ϕ to fit our data: the model in Ref. [53] simulates the mobility (μ) of a charge along the polymer backbone. This is related to the measured conductivity (σ_0) and the quantum efficiency (ϕ) through $\sigma_0=(\phi N_0)\mu e$. Then, knowing the absorbed experimental fluence, which determines the excitation density at the sample surface (N_0) through the absorption length of the light (l_0) used in the analysis (see equation 4.8), we can completely reproduce our data by varying only ϕ. Doing this, we find $\phi=0.5\pm0.2\times10^{-6}$and $\phi=3\pm1\times10^{-6}$ for solution and thin film samples, respectively. The error stated in these values originates mainly from uncertainty in the laser fluence of the excitation pulse, which affects the absolute magnitude of the fitted charge generation efficiency. It should be noted, however, that since exactly the same fluence is used in both measurements, the ratio of quantum efficiencies in thin film and solution samples can be determined with much larger accuracy, and is found to be $\phi_{\mathrm{film}}/\phi_{\mathrm{sol}}=6\pm1$, assuming identical mobility of charges in both samples.

However, the charge mobilities are known to be different in the two samples [20, 56], and the extracted factor of six difference between the film and solution samples from comparison to the mobility model certainly represents a *lower limit*: the model we use to calculate the frequency dependent mobility neglects both non-torsional defects (such as chemical defects resulting in a disruption of the π-conjugation [55]) and charge coupling to the lattice (polaron formation), and, as such, overestimates the conductivity. These effects have been shown to be much larger in films than in solution: from comparison of the model to measured mobilities at GHz frequencies, it was demonstrated that the model overestimates conductivity by a factor of 10-100 in solution [20] and an additional order of magnitude in film samples [56]. Correcting for this, it is evident that free charges are more efficiently generated in the thin film sample ($\phi\sim10^{-3}$) than in solution ($\phi\sim10^{-5}$). It should be noted that, compared to GHz frequencies, we are much less sensitive to defects at THz frequencies (as more local transport is probed) so that these numbers and their ratio constitute upper limits. Furthermore, the GHz mobilities were obtained from pulsed radiolysis experiments (such as reported in Ref. [56]), and the carrier densities were calculated assuming that all the energy deposited in the sample was used to generate charges. As this efficiency is generally much smaller than 100%, this sets a conservative *lower* limit for the carrier mobilities, and an *upper* limit for the quantum efficiencies estimated here.

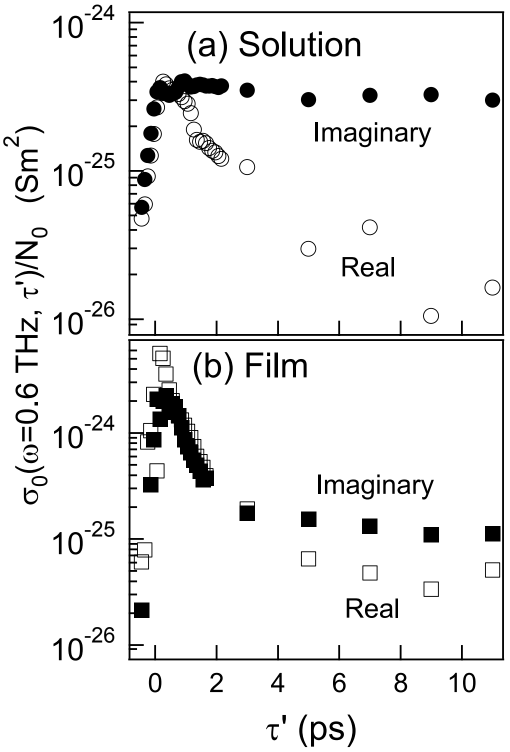

Figure 7.7 (a) Real and imaginary parts of the conductivity as a function of time *τ'* after photoexcitation, measured at 0.6 THz (the central frequency of the THz pulse), in the solution sample. The signal rises in around 300 fs, and in the first picosecond after photoexcitation both real and imaginary parts are significant. The real conductivity decays to effectively zero within ~5 ps, while the imaginary component persists for up to a nanosecond. (b) The same measurement on the film sample. Here, the initial conductivity is much higher, indicating a higher concentration of free charges. These persist on longer timescales, giving significant real conductivity after 5 ps. The imaginary component of conductivity decays within 150 ps, in agreement with the exciton lifetime in MEH-PPV films [49].

It is clear from the low quantum efficiencies that free charges are not the most common photospecies. As to the origin of the minority charge carriers, we note that for the high fluences used in our experiments, 2nd order effects may be anticipated, as the distances between excitations are typically a few nanometers, of the order of the electron-hole mean square displacement of 11 Å [57]. Indeed, exciton-exciton annihilation [58], generating free charges, may contribute to the small real component of the slowly decaying conductivity in figure 7.7(b). However, it cannot be the origin of the charge generation at early times, since we observe a linear dependence of the signal on excitation fluence, consistent with Moses et al. [10] and incompatible with an exciton-exciton annihilation mechanism. Further, this mechanism requires diffusional motion, which occurs slower than the timescale considered here.

The observed linear fluence dependence on both solution and film samples indicates that the probability per excitation of electron-hole dissociation is constant. This picture fits in well with recently established hot exciton dissociation mechanisms [12, 59]. These exciton models [12, 59] account for fast photogeneration of charges by the rapid dissociation of singular excitons (where the excess excitation energy is available for dissociation within ~100 fs after excitation). The unrelaxed, nascent excitons (before cooling) may use the excess excitation energy (above the lowest energy exciton state, around 0.5 eV for 400 nm) to dissociate into free charges. This results in a small number of free and thermalized charges with a predicted quantum efficiency $<<10^{-2}$. Carlos et al. [14] have included excitation to even higher energy states by a second photon within the excitation pulse, resulting in dissociation efficiencies $\sim 10^{-2}$, in agreement with our data. At high fluences, this process is linear in excitation intensity due to saturation of the initial absorption. Since exciton cooling is rapid (~100fs) [12, 59] hot exciton dissociation process explains the fast generation of free charges, within the first 300 fs, observed here.

'Hot' exciton dissociation is corroborated by the observed changes in the signal resulting from variation in the excitation wavelength and sample temperature. Experimentally, when corrected for the lower density of incident photons, excitation with 266 rather than 400 nm results in a fast signal that is twice as large, corresponding to a larger quantum yield for the generation of free charges. Further, because the exciton dissociation energy originates from the excitation pulse rather than from thermal contributions, hot exciton models also predict temperature independent dissociation. In our experiments, cooling the film sample from 300 to 30 K results in a small (<20%) *increase* in the signal attributed to free charges. The most likely explanation for this is an increase in mobility, rather than density, possibly due to decreasing torsional disorder in the polymer chain on cooling down.

The larger value for ϕ in the film sample (two orders of magnitude higher than in the solution sample) suggests that the close proximity of neighboring chains in the film sample facilitates hot exciton dissociation by allowing the resulting electron and hole charges to escape on separate chains, and minimizing any subsequent interaction. This mechanism agrees well with recent work of Lipson *et al.* [26] and Virgili *et al.* [60] who observe strong morphological effects on the photocurrent in PPV film samples. The interchain escape mechanism is not possible in solution due to the large nearest neighbor distances (~200 Å), so that the separated charges must reside on the same chain. This reasoning also explains why significant real conductivity is observed for times $\tau' > 5$ ps in the films sample (see figure 7.7(b)), indicating that at least some free charges have not recombined on these longer timescales, while in the solution sample the real component of the conductivity effectively decays to zero within 5 ps (see figure 7.7(a)). It should be noted that even the small number of free charges observed on sub-picosecond timescales in the solution sample may also result from chain-chain interactions: a small amount of aggregation may lead to interchain dissociation (though, for a good solvent such as benzene this is at most a weak effect [39]). Thus, a perfectly isolated polymer chain may not show *any* free charge generation, even on sub-picosecond timescales [60]. Reversely, in a perfectly organized film sample the free charge yield might be much larger, and close to the 100% generation efficiency, as e.g. observed by Hegmann *et al*. for organic single crystals [61].

While the chain-chain interactions seem to be essential to the mechanism of generation and survival of mobile charges (as evidenced by the large difference between short time conductivity in solution and film samples), the similar frequency dependence (which is a probe of the length scales involved in disorder dominated charge transport) in both samples suggests we are observing intrachain transport. Nevertheless, we can not rule out the interchain transport on long timescales. In fact, since the polymer chains are not infinite in length, interchain transport is required for there to be any DC conductivity (observed in such polymer films [1]). However, the THz field probes the high-frequency mobility on relatively shallow potential energy surfaces; clearly, transport along the polymer carbon backbone is highly favored over interchain transport, and the THz field of 1 kV/cm is too small to pull charges over an energy barrier. In other words, interchain hopping rates lie well below the THz range, and outside our frequency window.

7.4 Long-time conductivity: exciton states

The real part of the photoconductivity in both solution and film samples decays over 1-2 orders of magnitude within a few picoseconds, as shown in figure 7.7. The imaginary conductivity decays more slowly (~100 ps and ~300 ps for film and solution respectively). These decays agree well with exciton lifetimes in these materials from transient luminescence measurements [49, 62]), suggesting that the remaining conductivity on longer timescales results from excitons. We cannot, from our data, identify the free charge decay mechanism: it may be due to e.g. charge recombination or trapping at defects in the polymer chain.

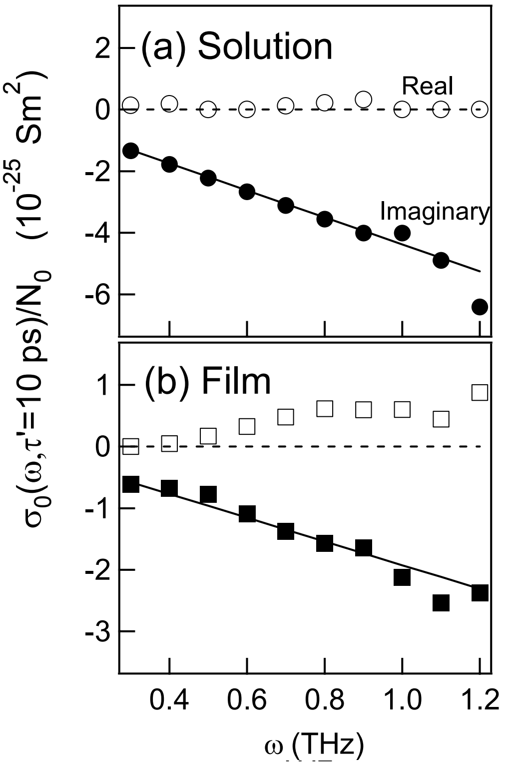

Figure 7.8 The normalized frequency-dependent complex conductivity measured in (a) solution and (b) film samples, 10 ps after excitation. At these times, the conductivity is predominantly imaginary: the solid and dashed lines show the response expected for excitons with polarizability α_{sol}=1950±640 Å^3 and α_{film}=770±180 Å^3 respectively, i.e. the average polarizability of excited species at these times is found to be three times larger in solution than in film.

After the initial fast decay, the remaining conductivity is mostly imaginary throughout the probed frequency range – see figure 7.8 (at τ'=10 ps). This is the spectral signature associated with the dielectric polarization of excitons, corresponding to temporary distortion of the exciton wavefunction by the field: the THz field can only induce an elastic deformation of the electron-hole wavefunctions (or, equivalently, a perturbation of the electron-hole separation), and does not give rise to any energy dissipation. Assuming that all absorbed photons contribute to the exciton conductivity (a reasonable assumption since free charge generation is very low and exciton recombination occurs on much longer timescales) the signal is determined by the average polarizability α of exciton species in the material and the instantaneous excitation density N_0. Indeed, we can model the response using the Clausius-Mossotti equation, which relates α to the low frequency conductivity [63]:

$$\frac{(\varepsilon-1)+\frac{i\sigma_0(\omega)}{\omega\varepsilon_0}}{(\varepsilon+2)+\frac{i\sigma_0(\omega)}{\omega\varepsilon_0}}=\frac{\varepsilon-1}{\varepsilon+2}+\frac{\alpha(\omega)N_0}{3}, \tag{7.1}$$

Probing at frequencies (1 THz = 4.1 meV) well below any exciton resonance or the exciton binding energy, the complex conductivity is determined by the DC polarizability (α_{dc}) of the exciton. The product of the density and polarizability therefore determines the fits shown in figure 7.8, yielding α_{dc}^{sol}=1950±640 Å^3 and α_{dc}^{film}=770±180 Å^3.

The values of exciton polarizability extracted from fitting the data are comparable to previous measurements on PPV samples, in the range 800–3333 Å^3 (see Ref. [64] for a summary), and comparable to the theoretical estimate of 1000 Å^3 for an exciton on an isolated PPV chain [57]. The errors in the extracted polarizabilities again originate mainly from uncertainty in the measured excitation fluence, which is identical in both measurements. Hence, the ratio of the solution and film polarizabilities $\alpha_{dc}^{sol}/\alpha_{dc}^{film}=2.5\pm 0.3$ can be determined with much larger accuracy. In solution, α_{dc}^{sol}=1950±640 Å^3 implies that the excitons are, on average, fairly weakly bound. For an exciton with a polarizability of this order (binding energy~0.8 eV [57]) the wavefunction is spread over several monomer units (root-mean square distance between electron and hole ~11 Å [57]), in agreement with observations on other pi-conjugated systems [8, 65]. In the film, the substantially smaller polarizability suggests the particles are on average more localized (<11 Å). The most obvious difference between the samples is the interchain distance: several authors have suggested that interchain species exist in significant numbers in film samples of PPV polymers [22, 23], though this is certainly controversial [24]. Our results indicate that interactions with neighboring chains do not, as one might expect, significantly increase delocalization. On the contrary, a *decrease* in polarizability in the film is observed, which can be explained by the increased disorder of the polymer chains in the film: the increased restriction placed on the polymer chains leads to a shorter average effective conjugation length, which in turn limits the exciton dimensions [30, 65].

7.5 Charge generation in model polymer solar cells

Polymer solar cells are a relatively recent development in the field of optoelectronics [3]. These devices utilize the semiconducting properties of conjugated polymers to convert light energy into electrical current. In comparison with existing silicon solar cells, polymer solar cells are light weight, flexible, and are both cheaper and more environmentally friendly in fabrication. On the negative side, polymer solar cells still struggle with relatively low energy conversion and degradation [2, 3]. In order to improve the operation of such cells, it is therefore imperative to understand the fundamental processes occuring after photoexcitation.

The high quantum yield of insulating excitons in conjugated polymers (see section 7.4) means that a polymer by itself cannot be used as the base material for a solar cell. Because of their insulating properties, excitons cannot trigger current, and therefore a second step is required in the solar cell in order to dissociate the bound electron-hole pairs into free charge carriers. A common method to achieve this in polymer solar cells is to mix the polymer with an electron or hole acceptor. The resulting blend allows for charge transfer (see figure 7.9), which increases the quantum yield of free carriers, by allowing the trapping of electrons (holes) at acceptor sites, and allowing the corresponding holes (electrons) to move freely along the polymer chain. In particular, PCBM (1-(3-methoxycarbonyl)-propyl-1-phenyl-(6,6)C61), a soluble fullerene, has proven to be an efficient electron scavenger for exciton dissociation in MEH-PPV [66].

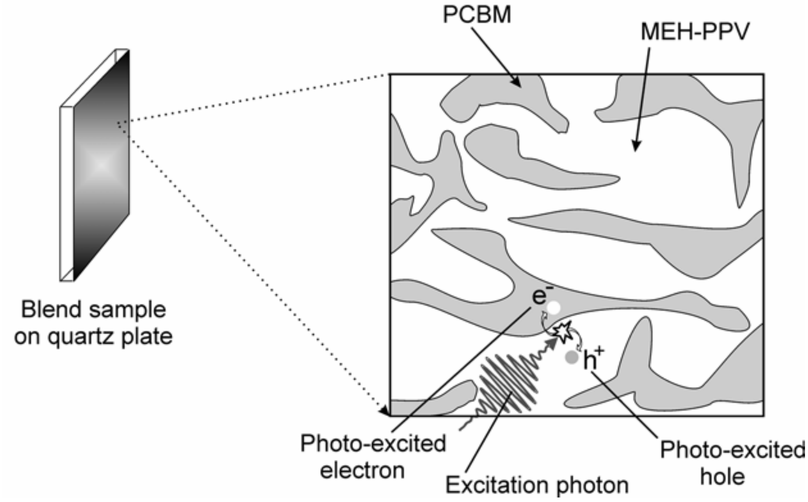

Figure 7.9 The morphology of an MEH-PPV/PCBM blend sample: the sample consists of regions of PCBM, the exact dimensions of which depend critically on preparation and treatment, but approximately <10 nm here [67]. When a photon is absorbed close to the interface between two regions, or the exciton diffuses to the interface, a charge transfer process can occur, resulting in electron injection into the PCBM whilst the hole remains in the polymer.

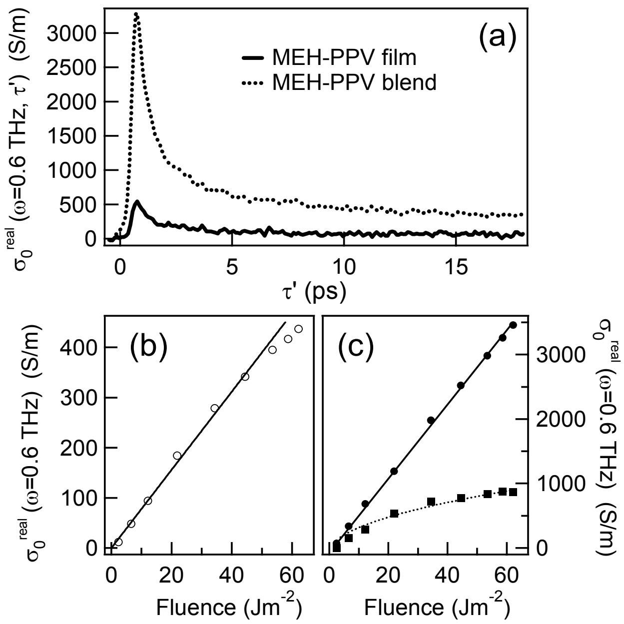

Figure 7.10 Comparison between photoconductivity of the MEH-PPV film and the MEH-PPV/PCBM blend (a) Real part of the conductivity, measured at 0.6 THz, as a function of time after excitation, for the MEH-PPV film (solid line) and the blend (dotted line). (b) Excitation fluence dependence of MEH-PPV film sample, measured at peak of the THz modulation (τ'=0.5 ps). (c) Excitation fluence dependence of blend sample, measured at peak (τ'=0.5 ps, circles) and after peak (τ'=10 ps, squares). The solid lines in (b) and (c) are linear fits to the data, while the dotted line is a square root function.

Figure 7.10(a) shows the real part of the conductivity as a function of time after excitation for an MEH-PPV/PCBM blend (1:1 by weight, prepared by mixing in chloroform solution and drop casting onto 1 mm quartz plate), compared to that for a pure MEH-PPV drop cast film. The most obvious difference in figure 7.10(a) is that the photoconductivity of the blend is almost an order of magnitude larger than in the polymer film, even within the rise of our signal. Since the absorption coefficient of PCBM is smaller than MEH-PPV at 400 nm [68], this additional signal cannot arise from direct excitation of the PCBM regions. This is confirmed by measurements on a pure PCBM film, for which the photoconductivity is around an order of magnitude smaller than the blend. Both of these observations indicate that the increase in conductivity in the blend is due to the dissociation of excitons in the MEH-PPV chains near the interfaces of PCBM molecules and polymer chains, giving rise to a relatively large number of free holes on the polymer chains, in agreement with reference [67]. The fast rise of the signal indicates that excitons are dissociated within the ~300 fs time resolution of the measurement, in agreement with references [10, 69]. Our observation of an increase in THz photoconductivity for samples with higher doping levels suggests that dissociation is much less than 100 %, consistent with reference [66].

The frequency dependent response of the free holes in the blend is very similar to that observed for charges in the pure polymer film (cf. figures 7.5(b) and 7.6). The temperature dependence is also similarly weak, with a ~20-30 % increase in conductivity on cooling the blend from 300 K to 30 K, as in the pure polymer film. However, while comparable fast decays are observed in the conductivities of both samples, some free holes (resulting from exciton dissociation) contribute to a long time real conductivity of the blend persisting even into the nanosecond regime (well beyond the exciton lifetime of the pure polymer film). This is observed as a long tail of the blend conductivity in figure 7.10(a). The decay of this conductivity tail has been measured with transient microwave spectroscopy, where the authors report decay times of 10-50 ns [67].

The excitation fluence (f_l) dependence of the conductivity of the blend is also presented in figure 7.10(c), and compared to that in the pure polymer film (figure 7.10(b)). It should be noted that the frequency dependence of the measured conductivities is independent of excitation fluence, with only the amplitude increasing for larger fluences. The conductivity measured at the peak signal (open and closed circles for pure polymer and blended sample respectively) for both samples is essentially linear with excitation fluence. At higher excitation fluences in the pure polymer sample, the conductivity dependence is very slightly sub-linear. This is attributed to radiation damage of the sample, as degradation is observed much faster when the sample is not continuously refreshed by in-plane motion during the experiment. This degradation is not observed in the blend sample, presumably due to the larger conductivity of the blend, which allows for more efficient heat dissipation.

After the peak (in the tail of the conductivity), the contribution to the real conductivity of surviving holes is sub-linear with fluence, reasonably described by power law dependence in the range $f_l^{0.3}$-$f_l^{0.5}$ (the dotted line in figure 7.10(c) is a square root dependence). This effect does not arise from saturation of traps, since this would produce a super-linear dependence. There are, however, several effects which could explain the observed sub-linear dependence. Firstly, since exciton dissociation will only be able to occur in regions close to the interfaces between MEH-PPV and PCBM, the local charge density in these regions is expected to be very large. This may lead to charge-charge effects (see section 4.7), limiting the conductivity at high densities. However, we may also expect these effects to play a role on short timescales, which is not observed. An alternative explanation would be an increase in non-geminate electron-hole recombination at high densities. Since this requires diffusion of charges [67], we may expect a larger decrease in conductivity on longer timescales. We suggest this back-recombination may limit the conductivity of such polymer blends at high excitation density. A more in-depth analysis of this behavior in model polymer solar cells (by, e.g., investigating how the sub-linearity appears as a function of time after excitation) is beyond the scope of this thesis, and will be presented in a future paper.

7.6 THz emission spectroscopy

Although the observation of significant real photoconductivity in MEH-PPV films [1] demonstrates the presence of free charges, it does not itself tell us whether carriers are generated directly on ultrafast timescales or produced on longer timescales through, for example, exciton-exciton annihilation. Unfortunately, conventional transient photoconductivity measurements [16, 51] lack the resolution to resolve the ultrafast excitation process. However, the results from previous sections indicate that photoexcitation of MEH-PPV leads to the generation of free charges on ultrafast timescales, within the ~300 fs time resolution of THz-TDS.

Additional information about the timescale of charge carrier generation and nature of the transport can be obtained by probing the radiation dispersed by the accelerating charges [70, 71]. When changes in photocurrent occur on (sub)-picosecond timescales, THz radiation is emitted. The shape of the THz pulse is determined by the rise and decay of the photocurrent, and thus provides a direct probe of the ultrafast transient photoconductivity. In this manner, information regarding the rate of charge carrier generation and time-dependent mobility can be obtained. This technique is ideally suited to the study of charge generation and cooling on sub-picosecond timescales, and has been successfully applied to study the photoexcitation dynamics in materials such as low temperature grown gallium arsenide [71]. Previous measurements on semiconducting polymer systems have also proven useful [70], but suffered from a limited bandwidth so that sub-picosecond processes could not be resolved.

In this section, we employ THz emission spectroscopy to study the ultrafast charge generation in MEH-PPV. We set an upper limit for charge generation in MEH-PPV within the first 200 fs after photoexcitation. By comparing our results to a model system (gallium arsenide) the quantum efficiency for charge generation in the polymer is confirmed to be less than 1% – over two orders of magnitude lower than in GaAs. Both conclusions are consistent with charge generation through hot exciton dissociation.

The insulating GaAs crystal is <100> cut, produced by Wafer Technology LTD. The ~20 μm MEH-PPV films are prepared by drop casting from chloroform solution onto water free quartz plates, using dry polymer from Sigma Aldrich. Silver electrodes are placed directly on the GaAs crystal and copper electrodes are incorporated into the polymer film (both ~1 cm spacing). In both cases, a static field of is 10 kV/cm applied. At such low field charge injection effects are negligible [72], and only photocurrent is observed. Photoexcitation is accomplished with 400 nm (3 eV) laser pulses with a durations of 180 fs (full width at half maximum, FWHM), allowing above band gap excitation of both GaAs and

MEH-PPV (1.6 eV [71] and 2.4 eV [72] respectively). The excitation spot size in both measurements is ~2 mm. A parabolic mirror is placed as close to the samples as possible to properly collect all radiated frequency components, and no effects due to the weak focusing are observed. The emitted THz pulse is detected in the far field through electro-optical sampling (see section 2.2) using 800 nm pulses (FWHM 180 fs) incident on a 1.2 mm <110> ZnTe crystal.

The measured THz fields, $E(t)$, emitted by the GaAs and MEH-PPV samples are shown in figure 7.11(a) and (b), for absorbed fluences (corrected using equation 4.8) of 10 and 225 μJ/cm^2 respectively. Measured laser fluences were corrected for reflection effects using the dielectric functions of GaAs and PPV films, from [73] and from [41], respectively.

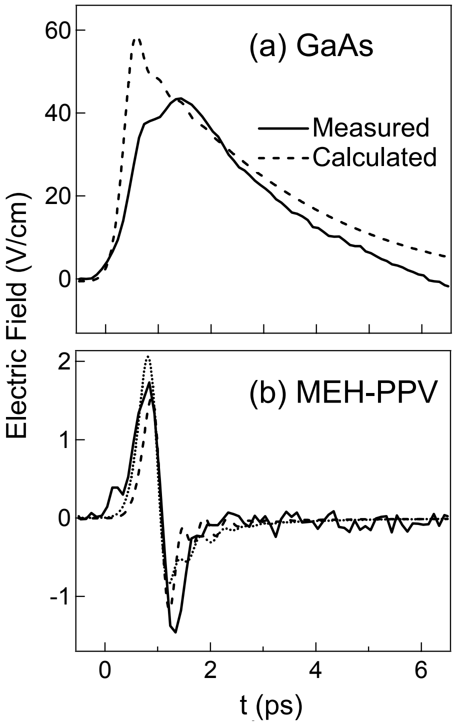

Figure 7.11 Electric fields radiated from (a) GaAs, excited using 10 μJ/cm^2, 180 fs, 400 nm pulses, and (b) MEH-PPV, excited using the same pulses at 225 μJ/cm^2, both biased with an external field of 10 kV/cm. The broad positive peak in the generated field in (a) is due to a slow rise in photocurrent resulting from electron cooling effects. In (b), the sharp change in electric field direction suggests a peak in photoconductivity: the initial rise in photocurrent due to generation of carriers is followed by a rapid decrease in carrier mobility due to the finite conjugation length of the polymer backbone. The dashed lines show the response calculated using time dependent mobilities from Refs. [74] and [53] respectively, plotted in figure 7.12, assuming instantaneous generation of charges. The dotted line in (b) shows the corresponding pulse assuming charges generated by hot excitons with a dissociation rate of (200 fs)$^{-1}$.

For MEH-PPV, a higher fluence is required to obtain sufficient signal to noise, while for GaAs care must be taken to avoid detector saturation. Although the signal *amplitude* scales linearly with both the strength of the applied bias field and the photoexcitation intensity, the signal *shape* (time dependence) is independent of these experimental parameters. In both samples the THz pulse is radiated only when *both* the static field and excitation pulses are present, ruling out optical rectification [75] as a source of signal. Despite the lower fluence, the pulse emitted from the GaAs sample is approximately 25 times larger than that from MEH-PPV. The waveforms are also very different in shape, with one main peak from the GaAs photocurrent, while the MEH-PPV sample gives approximately equal positive and negative peaks, indicating that the rise and fall of photocurrent in this sample occurs on a very similar timescale. Also, the GaAs signal is much broader, with a FWHM~3 ps, compared to <1 ps for the polymer.

To model the data shown in figure 7.11, we note that the emitted THz in the far field, $E(t)$, is proportional to the time derivative of the time dependent current density [76]. The current can be written as a convolution of the time dependent carrier generation rate and the mobility, $G(t)$ and $\mu(t)$, so that

$$E^{inc}(t) \propto \frac{\partial}{\partial t} E^{app} \int_{0}^{+\infty} \mu(\tau) G(t-\tau) d\tau, \tag{7.2}$$

where E^{app} is the applied static field in the sample driving the current. To compare $E^{inc}(t)$ – the field incident on the detector – to $E(t)$ – our detected waveform – we have to account for the propagation of the field through the electro-optic sensor used in the experiments. The detected waveform, $E(t)$, is related to $E^{inc}(\omega)$, the Fourier transform of $E^{inc}(t)$, through the detector response function, $f(\omega)$ (see section 2.3). Therefore by modeling $G(t)$ and $\mu(t)$ in equation 7.2, we can calculate $E^{inc}(t)$ and propagate the waveform through our sensor, obtaining the detected waveform $E(t)$, to reproduce the data.

As several dynamic processes may occur directly following photoexcitation, carrier properties on ultrafast timescales can be very different from the equilibrium behavior in a material. Hence it seems inappropriate to use steady state mobilities (~8000 and ~10^{-5} cm^2/Vs for GaAs [77] and MEH-PPV [4], respectively) to describe $\mu(t)$ on sub-picosecond timescales after excitation. In the case of GaAs, exciting at 400 nm (with 1.5eV excess energy) results in photo-electrons having sufficient energy to undergo inter-valley scattering into the higher energy L and X valleys. However, the low mobility of electrons in these valleys means the onset of photoconductivity is delayed, which is determined by the dynamics of electrons scattering into the high mobility Γ valley. The resulting time-dependent mobility in GaAs, $\mu(t)$, can be calculated using a kinetic model developed by Stantan and Bailey [74], assuming asymptotic behavior at long times to the steady state electron mobility of 8000cm^2/Vs [77], as plotted in figure 7.12(a). Evolution of the hole response is ignored in this calculation since hole mobilities are over an order of magnitude lower [78]. Also plotted is the generation rate, $G(t)$, given by the Gaussian intensity profile of the 400nm excitation pulse. It is clear that the slow evolution of the THz field emitted from the sample in figure 7.11(a) arises from slow cooling of electrons and the resulting slow rise in $\mu(t)$, rather than a slow generation process. Indeed, we can reproduce the data quite well – the result is plotted as a dashed line in figure 7.11(a) – using equation 7.2. It should be noted that the only adjustable parameter is the amplitude of $G(t)$.

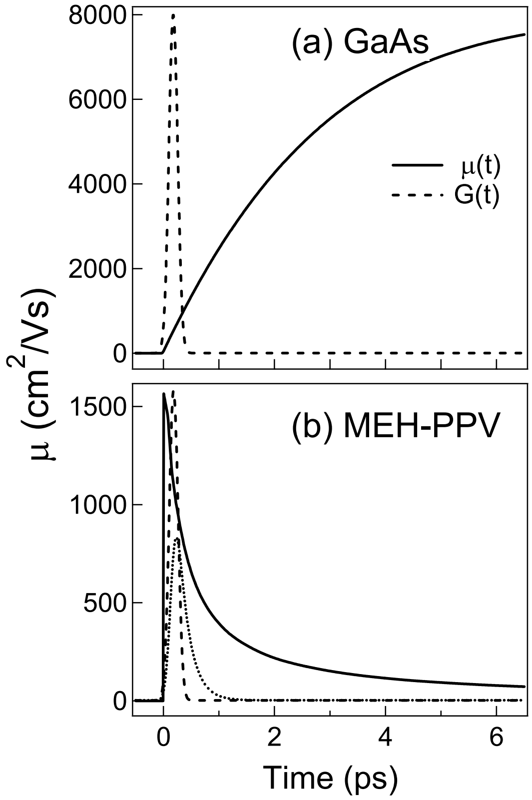

Figure 7.12 Comparison of timescales involved in charge generation and cooling; the solid lines in both figures represent the calculated time dependent mobility, μ (t), in (a) GaAs (excitation with 400 nm, calculated using the formalism introduced in Ref. [74]) and (b) MEH-PPV (calculated from Ref. [53] – see text). Dashed lines represent the generation rate, G(t), assuming instantaneous generation of charges upon excitation, i.e. described by the Gaussian intensity profile of the excitation pulse (FWHM 180 fs). The dotted line in (b) describes the generation rate for charges generated from hot excitons with a dissociation rate of (200 fs)$^{-1}$ (see text). In (a) the rise in photocurrent is dominated by the slow evolution in μ(t), while in (b) the rise in G(t) and decay in μ(t) occur on the same timescale.

The time dependent mobility of the MEH-PPV sample is calculated following the formalism in Ref. [53]. This model, also used to simulate the frequency dependence of charge conductivity in section 7.3, is based on the tight-binding approximation combined with static torsional disorder – i.e. deviations from planar alignment of the polymer chain determining its effective conjugation length. The calculated time-dependent diffusivity, $D(t)$, is related to the time-dependent mobility in the presence of an applied field through the Einstein relation, $\mu(t) = eD(t)/k_bT$ [79]. The resulting *hole* mobility is plotted in figure 7.12(b). The electron mobility probed in the THz frequency domain is expected to be similar to that of holes. Indeed, microwave conductivity measurements (near 30 GHz) have revealed comparable mobilities of holes and electrons on isolated MEH-PPV chains [20]. According to Martens *et al.* [54], the much lower electron mobilities observed in time-of-flight experiments or admittance spectroscopy may be traced to extrinsic effects such as trapping of electrons by impurities or structural defects. On the picosecond timescale involved in the present experiments such extrinsic effects are expected to play a minor role.

Clearly, $\mu(t)$ in MEH-PPV has a shape very different from that in GaAs, with a very large initial value decreasing rapidly towards the small steady state values observed in these samples (~10^{-5} cm^2/Vs [4]). In GaAs, the mobility increases with time as carriers cool and return to the highly mobility state in the Γ valley. In MEH-PPV, the finite conjugation length along the polymer backbone provides a large initial mobility, but greatly restricts charge motion at long times, as the rate determining step at longer times is the hop across the inter-segment barrier. This rapid damping of charge motion leads to a maximum in photoconductivity, where the rise in photocurrent is due to the charge generation, and damping by the finite conjugation length causes the subsequent rapid decay. This agrees qualitatively with the double peak structure of the radiated THz field in figure 7.11(b), with the maximum in photocurrent corresponding to the change in sign of the emitted field.

Whereas for GaAs it is apparent that $G(t)$ simply follows the excitation intensity, for the polymer $G(t)$ depends on the precise mechanism of carrier generation. Assuming, however, that $G(t)$ has the same Gaussian profile as the excitation intensity – that is, neglecting any delay in onset of carrier generation (expected from cooling effects or charge generation from exciton-exciton annihilation) – we can reproduce the radiated THz field shown in figure 7.11(b), varying only the amplitude of $G(t)$ as before. The calculated curve reproduces the waveform reasonably well, including the magnitude of positive and negative lobes.

The fact that the calculated radiated field oscillates faster than the measurement suggests that charge generation may not be fully instantaneous, and *G*(*t*) may be slightly broader than the intensity profile of the excitation pulse. The dotted line in figure 7.11(b) is calculated assuming an extra generation step described by rate (200 fs)$^{-1}$: the charge generation rate, $G_0(t)$, now depends on the pump intensity profile (described by rate *G*(*t*)), the extra formation step (described by rate *k*=(200 fs)$^{-1}$), and the time dependent excitation density, $N(t)=\int_{-\infty}^{t}(G(t')-kN(t'))dt'$, such that $G_0(t)=kN(t)$. The calculation assuming this additional formation rate determining step agrees better with the measured THz pulse in terms of the width, but the agreement in shape is slightly diminished.

In any case, this analysis sets an upper limit for charge generation within 200 fs of photoexcitation, which is much faster than the diffusion timescales that would be required for charge generation by, for example, exciton-exciton annihilation [15] or cold exciton dissociation at defects [13]. Hence, another mechanism for rapid charge generation in semi-conducting polymers must be operative. It is also evident that the cooling effects observed in GaAs are much less significant in the polymer sample, as these would induce broadening in $\mu(t)$, and a corresponding broadening in the radiated THz field. The good agreement between the calculated and experimentally observed emitted THz field corroborates the theoretical model of dispersive charge transport which is limited by disorder-induced barriers, causing non-Drudian transport.

By comparing the magnitudes of *G*(*t*) required to reproduce the data in figure 7.11, and taking into account the excitation fluences used in the experiment, it is straightforward to compare the relative quantum efficiencies of charge generation in the two samples. This yields a quantum efficiency in MEH-PPV of approximately 0.05% of that in GaAs. It should be noted that the accuracy of this number is again limited by the accuracy of the model used to describe $\mu(t)$ in the polymer, particularly at short times. On longer timescales (in the ps to ns range), an estimate of this accuracy can be made by comparing mobilities measured in the microwave (30 GHz) region [20] to those predicted by the model at the same frequency [53]. From this comparison, it is apparent that the error in the model due to additional non-torsional defects is approximately a factor of ten, though this is certainly much smaller on the sub-picosecond timescales probed here, where defects will play a much less important role. Hence, it is clear that only a small fraction of photoexcitations in the polymer results in the ultrafast generation of free charges. This is inconsistent with the band structure picture, where initial above band gap photo-excitations initially exist as free charges, which may later relax to sub-band gap exciton states. In addition, the rapid generation of charge carriers is also not consistent with an exciton-exciton annihilation mechanism, as this requires (slow) exciton diffusion.

A more probable mechanism, consistent with both the low quantum efficiency *and* the rapid generation of *thermal* carriers, is through *hot* exciton dissociation [12, 59] discussed in section 7.3. Since exciton cooling occurs on the 100-300 fs timescale [12, 59], this mechanism results in rapid charge generation, entirely consistent with the <200 fs generation time and <1 % charge generation efficiency observed in this work.

7.7 Conclusions

To conclude, we have measured the THz frequency-dependent conductivity on sub-picosecond timescales of a solution and thin film sample of a model semi-conducting polymer (MEH-PPV). This allows us to study interchain effects on the ultrafast processes that follow photoexcitation. Our results indicate that the close proximity of nearest neighbor chains in the film sample facilitates exciton dissociation on sub-picosecond timescales by allowing the resulting electron and hole charges to escape on separate chains, and permitting significant real conductivity even on much longer timescales. In solution, significantly fewer charges are photo-generated, but the increased freedom of the polymer chains results in a larger conjugation length and excitons with greater spatial extent and a correspondingly larger average polarizability than in the film sample.

These results show that the differences in morphology have a pronounced effect on the ultrafast photophysics of polymer semiconductors. This is in agreement with recent work by several other groups [29, 40, 80-83]. These findings have implications for the design and application of polymers in electro-optic devices [7]: these devices work by converting light to excitons and/or charges and vice versa. Hence, by controlling interchain distances, properties that are important to the operation of such devices can be modified. In particular, it is clear that chain morphology plays a key role in the ultrafast exciton dissociation into separated free charges. Morphological effects have also been observed in polymer solar cells, where thermally induced changes can result in a significant increase in device efficiency [2, 84, 85]. Other devices, such as polymer light-emitting diodes, rely on the conversion of free electrons and holes into light emission. For these devices, the presence of weakly emissive interchain species greatly limits the efficiency of this process [21, 40, 86]. Hence, for efficient luminescent devices [87], interchain effects are undesirable.

We have also studied charge generation in a film sample by measuring the radiated THz wave after photo exciting the polymer with a femtosecond visible pulse in the presence of an electric field. This allows us to study the rise and fall of photocurrents in these materials on sub-picosecond timescales. We find an upper limit for charge generation in MEH-PPV of 200 fs after photoexcitation, and estimate the quantum efficiency for charge generation in the polymer to be over two orders of magnitude lower than in GaAs. Both conclusions are consistent with charge generation through hot exciton dissociation in semiconducting polymers.

References

[1] C. H. Lee, et al., Phys. Rev. B **47**, 15543 (1993).
[2] V. Dyakonov, Appl. Phys. A - Mater. **79**, 21 (2004).
[3] J. Nelson, Curr. Opin. Sol. Stat. Mat. **6**, 87 (2002).
[4] E. Lebedev, et al., Appl. Phys. Lett. **71**, 2686 (1997).
[5] P. W. M. Blom, et al., Phys. Rev. B **55**, R656 (1997).
[6] J. Shan, et al., Phys. Rev. Lett. **90**, 247401 (2003).
[7] M. Angelopoulos, IBM J. Res. Dev. **45**, 57 (2001).
[8] G. Hadziioannou and P. F. v. Hutten, in *Semiconducting Polymers* (Wiley-VCH, Weinheim, 2000).
[9] A. Kohler, et al., Nature **392**, 903 (1998).
[10] D. Moses, et al., Phys. Rev. B **61**, 9373 (2000).
[11] D. Moses, et al., Synth. Met. **125**, 93 (2001).
[12] V. I. Arkhipov, et al., Phys. Rev. Lett. **82**, 1321 (1999).
[13] B. Dulieu, et al., Phys. Rev. B **57**, 9118 (1998).
[14] C. Silva, et al., Phys. Rev. B **64**, 125211 (2001).
[15] G. J. Denton, et al., Phys. Rev. Lett. **78**, 733 (1997).
[16] C. H. Lee, et al., Phys. Rev. B **49**, 2396 (1994).
[17] M. Chandross, et al., Phys. Rev. B **50**, 14 702 (1994).
[18] B. J. Schwartz, Ann. Rev. Phys. Chem. **54**, 141 (2003).
[19] A. R. Inigo, et al., Synth. Met. **139** (2003).
[20] R. Hoofman, et al., Nature **392**, 54 (1998).
[21] L. J. Rothberg, et al., Synth. Met. **80**, 41 (1996).
[22] M. Yan, et al., Phys. Rev. Lett. **72**, 1104 (1994).
[23] J. G. Muller, et al., Phys. Rev. Lett. **88**, 147401 (2002).
[24] B. Kraabel, et al., Phys. Rev. B **61**, 8501 (2000).
[25] A. Ruini, et al., Phys. Rev. Lett. **88**, 206403 (2002).
[26] S. M. Lipson, et al., J. Appl. Phys. **95**, 6138 (2004).
[27] H. A. Mizes and E. M. Conwell, Phys. Rev. B **50**, R11243 (1994).
[28] M. Wohlgenannt, et al., Phys. Rev. B **69**, 241204(R) (2004).
[29] M. Ariu, et al., Phys. Rev. B **67** (2003).
[30] A. J. Cadby, et al., Phys. Rev. B **62**, 15604 (2000).
[31] T. Q. Nguyen, et al., J. Chem. Phys. **110**, 4068 (1999).
[32] T. Q. Nguyen, et al., J. Phys. Chem. B **104**, 237 (2000).
[33] S. Xu, et al., Phys. Rev. B **64**, 193201 (2001).
[34] T. Q. Nguyen, et al., J. Phys. Chem. B **104**, 237 (2000).
[35] S. V. Frolov, et al., Phys. Rev. Lett. **85** (2000).

[36] S. Stagira, et al., Phys. Rev. B **64**, 205205 (2001).
[37] H. D. Burrows, et al., J. Mol. Struct. **563**, 41 (2001).
[38] B. Kraabel, et al., Phys. Rev. B **50**, 18543 (1994).
[39] G. H. Gelinck, et al., Synth. Met. **84**, 595 (1997).
[40] S. Vaidyanathan, et al., Synth. Met. **142**, 1 (2004).
[41] *Polymer Data Handbook* (Oxford University Press, Oxford, 1999), p. 722.
[42] M. C. Beard, et al., Phys. Rev. B **62**, 15764 (2000).
[43] E. Hendry, et al., Phys. Rev. Lett. **92**, 196601 (2004).
[44] M. C. Beard, et al., J. Phys. Chem. B **106**, 7146 (2002).
[45] M. Samoc, et al., J. Opt. Soc. Am. B **15**, 817 (1998).
[46] P. Jepsen, et al., Appl. Phys. Lett. **79**, 1291 (2001).
[47] E. Kang, et al., J. Solgel Sc. Tech. **26**, 981 (2003).
[48] S. Stagira, et al., Phys. Rev. B **64**, 205205 (2001).
[49] G. R. Hayes, et al., Phys. Rev. B **52**, R11 569 (1995).
[50] I. B. Martini, et al., Phys. Rev. B **69**, 035204 (2004).
[51] D. Moses, et al., Phys. Rev. B **54**, 4748 (1996).
[52] The dielectric function of solution is taken to be that of the solvent.
[53] F. C. Grozema, et al., J. Phys. Chem. B **106**, 7791 (2002).
[54] H. C. F. Martens, et al., App. Phys. Lett. **77**, 1852 (2000).
[55] H. Becker, et al., Macromolecules **32**, 4925 (1999).
[56] J. M. Warman, et al., J. of Phys. C. **14**, 9935 (2002).
[57] J. W. v. d. Horst, et al., Chem. Phys. Lett. **334**, 303 (2001).
[58] N. T. Harrison, et al., Phys. Rev. Lett. **77**, 1881 (1996).
[59] D. M. Basco and E. M. Conwell, Phys. Rev. B **66**, 155210 (2002).
[60] T. Virgili, et al., Phys. Rev. Lett. **94**, 117402 (2005).
[61] F. A. Hegmann, et al., Phys. Rev. Lett. **89**, 227403 (2002).
[62] G. H. Gelinck, PhD Thesis (Delft University of Technology, Delft, The Netherlands, 1998), p. 81.
[63] N. W. Ashcroft and N. D. Mermin, in *Solid State Physics* (Saunders College, 1976), p. 542.
[64] G. H. Gelinck, et al., Phys. Rev. B **62**, 1489 (2000).
[65] M. Knupfer, et al., chem. phys. lett. **318**, 585 (2000).
[66] M. C. S. N. A. Schultz and N. S. Sariciftci, Phys. Rev. B **67**, 085202 (2003).
[67] T. J. Savenije, et al., Phys. Rev. B **69**, 155205 (2004).
[68] H. Hoppe, et al., Sol. Energ. Mat. Sol. C. **80**, 105 (2003).
[69] C. J. Brabec, et al., Chem. Phys. Lett. **340**, 232 (2001).
[70] C. Soci and D. Moses, Synth. Met. **139**, 815 (2003).
[71] H. Nemec, et al., J. Appl. Phys. **90**, 1303 (2001).
[72] I. H. Campbell, et al., Appl. Phys. Lett. **72**, 1863 (1998).
[73] S. Bergfeld and W. Daum, Phys. Rev. Lett. **90**, 036801 (2003).
[74] C. J. Stanton and D. W. Bailey, Phys. Rev. B **45**, 8369 (1992).
[75] X. C. Zang, et al., Appl. Phys. Lett. **61**, 2764 (1992).
[76] P. U. Jepsen, et al., J. Opt. Soc. Am. B **13**, 2424 (1996).
[77] J. S. Blakemore, J. Appl. Phys. **53**, R123 (1982).
[78] M. L. Lovejoy, et al., Appl. Phys. Lett. **61**, 2683 (1992).
[79] G. Oshanin, et al., Phys. Rev. E **66** (2002).
[80] T. G. Bjorklund, et al., Synth. Met. **142**, 195 (2004).
[81] M. Fakis, et al., Phys. Rev. B **68** (2003).
[82] B. J. Schwartz, Annu. Rev. Phys. Chem. **54**, 141 (2003).
[83] C. H. Tan, et al., Org. Electron. **3**, 81 (2002).
[84] J. K. J. van Duren, et al., Adv. Funct. Mater. **14**, 425 (2004).
[85] M. Drees, et al., Phys. Rev. B **69** (2004).
[86] R. H. Friend, et al., Nature **397** (1999).
[87] J. A. E. Wasey, et al., Phys. Rev. B **64**, 205201 (2001).

Summary

Semiconductors are a class of materials that can be engineered to either conduct or insulate, making them essential building blocks of many electro-optical components and devices. Such devices rely on the conversion of light into charge carriers (as in a solar cell) or vice-versa (as in a light-emitting diode). In silicon (the most commonly used semiconductor) it has long been known that optical excitation leads to the generation of *free* charge – herein lies the principle behind a silicon solar cell. In other semiconductors, however, another process can take place: the formation of so-called excitons. Excitons are formed when the electron and the hole cannot escape each other, remaining *bound* to each other without recombining. A key factor determining the efficiency of electro-optical devices is therefore the probability of exciton and free charge formation after photoexcitation, and their subsequent transport through the material.

In this thesis, ultrafast laser techniques are used to study photoexcitation processes in novel semiconductors and novel semiconductor structures, focusing on THz time domain spectroscopy (THz-TDS). This technique uses a quickly oscillating electric field to probe charges, which are generated in a semiconductor with a femtosecond (100 fs = 10^{-13} s) laser pulse. The oscillating field is not applied using electrodes, but instead is contained in a freely propagating electrical pulse of ~1 ps (= 10^{-12} s) duration. Free charge carriers are accelerated by this field, and the energy from this acceleration can be dissipated to the lattice through scattering, resulting in *absorption*. The absorption of the field is proportional to the *real* conductivity. Excitons on the other hand, cannot absorb the field pulse, but slow its propagation - this gives rise to *imaginary* conductivity. The ability of THz-TDS to measure simultaneously the real and imaginary conductivity makes it a very powerful tool in the characterization of photoexcitation properties (e.g. in determining the quantum efficiencies of free charge and exciton generation, and characterizing their subsequent transport).

In polarizable semiconductors (materials with high dielectric functions), the dispersive response of free charges contains key information about the nature of electrical conduction, the electron mobility and the mass of the conducting particles. In chapter 4, the electron transport properties of single crystal titanium dioxide (TiO_2) and porous TiO_2 (fused nanoparticles, used e.g. in Grätzel solar cells) are investigated using THz-TDS. TiO_2 is a high dielectric function semiconductor widely used in photocatalysts and solar energy converters. It is clear that the ionic character of TiO_2 gives rise to a strong electron-lattice interaction, leading to the formation of a polaron: a quasi-particle consisting of an electron and the accompanying lattice deformation. In the single crystal sample we find transport to be limited

by polaron formation leading to an electron effective mass much larger than the electron rest mass and low electron mobilities ~1 cm^2/Vs at room temperature. In the porous sample, screening of the electric field restricts electron mobility further, and we set an upper limit for short term electron mobility in these samples of ~10^{-3} cm^2/Vs. This value is still significantly larger than long term mobilities measured with time of flight techniques on porous samples, indicating that significant improvement in charge transport in Grätzel cells is possible if traps can be passivated and/or inter-particle transport can be improved. While the electron mobility limits the internal resistance of a cell, the overall quantum efficiency of the Grätzel solar cell is limited by electron diffusion to the outer electrodes of a cell. Screening effect are not expected to play a role in diffusion, which is unaffected by electric fields. Our results demonstrate that a substantially lower internal cell resistance is possible if screening effects can be reduced, either by increasing the volume fraction of the transport material, or by using less polarizable materials.

In non-polarizable semiconductors (materials with low dielectric functions), the electrons and holes can bind together to form excitons instead of becoming separated, independent particles, as in polarizable semiconductors (such as TiO_2). With THz-TDS we can use the drastically different response of excitons and free charge carriers to distinguish and measure the dynamics of the two species. In chapter 5, we study the formation of an exciton gas in ZnO, after initially exciting a plasma with >1 eV excess energy, using THz TDS. In the low density regime (where electron-hole pairs do not interact), we observe very slow formation of an exciton gas, occurring on a ~100 ps timescale, coinciding with the disappearance of the conducting plasma consisting of free carriers. The relatively slow dynamics indicate that excitons are not formed until virtually all the initial excess energy of photoexcitation is lost. Exciting the sample to higher electron-hole densities, the Coulomb attraction which binds electrons and holes together at low density may be screened, leading to the formation of an electron-hole liquid. The transition from an insulating gas of excitons to a conducting liquid state occurs near the Mott density. Above this density, we observe formation of an electron-hole liquid in around 5 ps after excitation. These very fast dynamics, faster than cooling observed at low density, suggest that the liquid phase can form directly from the hot plasma, probably through many-body recombination of hot charges. This conclusion is corroborated by the temperature dependence of the dynamics: while exciton formation in the low density regime is strongly temperature dependent, the liquid formation dynamics in the high density regime are essentially independent of lattice temperature.

Semiconductor quantum dots (QDs) have unique optical properties owing to the confinement of the electron and hole wave functions, giving rise to discrete energy levels. Especially for QD applications in solar cells, a key aspect is the step immediately following absorption of a photon: the cooling of the photo-generated hot electron and hot hole to their lowest energy states. Whereas in bulk semiconductors, rapid, sequential emission of phonon quanta results in fast cooling, in QDs the absence of a continuum of states means that energy transfer from the carriers to the lattice must occur in discrete steps. As the spacing between the electronic levels (typically ~200 meV) is large compared to the LO phonon frequency (~25 meV), this requires the simultaneous emission of a large quantity of phonons, a process of low probability. Hence, it has been proposed that hot electron cooling in QDs is hindered by a so-called "phonon bottleneck", resulting in cooling times in the nanosecond range. In chapter 6, THz-TDS is combined with luminescence up-conversion, to study the cooling of holes and electrons respectively in cadmium selenide QDs of various diameters. We observe the first direct evidence of electron to hole energy transfer, confirming the Auger assisted cooling for electrons. This mechanism allows the phonon bottleneck to be bypassed, and we obtain the first quantitative measurements of electron-hole coupling in CdSe QDs.

Polymeric semiconductors are cheap and flexible alternatives for standard semiconductors such as silicon. As such, they are finding increasing application in electro-optical devices such as light-emitting diodes and solar cells. In spite of the efforts by research groups worldwide, it is still not clear what exactly happens when a polymeric semiconductor absorbs a photon. In silicon, it is well known that optical excitation generates free charge carriers. In a semiconducting polymer, the observation of significant real conductivity indicates that free charge carriers can also be photogenerated. However, the mechanism for charge generation in a polymeric semiconductor is still much debated. In answering this question, one of the most important questions is: are excitons or free charges primarily formed upon photo-excitation? In chapter 7, we use THz-TDS to follow the sub-picosecond excitation process in two phases of the model semiconducting polymer poly[2-methoxy-5-(2'ethyl-hexyloxy)-1,4-phenylene vinylene] (MEH-PPV). In solution the polymer concentration is sufficiently low, and the solvation (in benzene) is sufficiently strong, so that we can study this process on essentially isolated polymer chains. In a thin film sample interchain interactions are present. By measuring the real and imaginary component of photoconductivity on femtosecond time scale, it is clear that mainly excitons are formed on photoexcitation, with an efficiency of almost 100%. Very few free charges are formed in the solution sample (< 0.1%), and remain mobile for only a short time (~10^{-12} s). In the film, a higher number of free charges are generated (< 1%), indicating that the interaction between chains helps the dissociation process. These results are important for applications of polymer semiconductors in solar cells, making clear that another mechanism is required to dissociate excitons before the photo-generated electrons and holes can diffuse to the cell electrodes.

Samenvatting

Halfgeleiders zijn een klasse van materialen die kunnen geleiden of isoleren, en vormen als zodanig essentiële bouwstenen van elektro-optische apparaten. De werking van dit soort componenten berust vaak op de omzetting van licht in ladingsdragers (bijv. in een zonnecel), en vice versa (zoals in een licht emiterende diode). Voor silicium (de meest gebruikte halfgeleider) is reeds lang bekend dat optische excitatie leidt tot de vorming van vrije ladingen – hierop berust ook de werking van de silicium zonnecel. In andere halfgeleiders kan echter ook een ander proces plaatsvinden: de vorming van zogenaamde excitonen. Een exciton wordt gevormd als het electron en het gat niet van elkaar kunnen ontsnappen, en aan elkaar gebonden blijven zonder te recombineren. Een zeer belangrijke factor die de efficientie van elektro-optische componenten bepaalt is daarom de waarschijnlijkheid van de vorming van excitonen en vrije ladingen, en hun verdere transport door het materiaal.

In dit proefschrift worden ultrasnelle lasertechnieken gebruikt om licht-geïnduceerde-processen in nieuwe halfgeleiders en nieuwe halfgeleiderstructuren te onderzoeken. Wij gebruiken in het bijzonder THz tijdsdomein spectroscopie (THz-TDS). De techniek behelst het heel snel aan- en uitzetten van een electrisch veld, direct nadat met een femtoseconde (100 fs = 10^{-13} s) laserpuls ladingen en excitonen zijn gemaakt. Het veld wordt niet met electrodes aangelegd, maar met een vrij propagerende electrische puls met een duur van 1 ps. De vrije ladingsdagers worden versneld in dit veld, botsen daardoor met het rooster, en kunnen daardoor energie uit het veld in het rooster stoppen: het veld wordt verzwakt (absorptie). De absorptie van het veld is evenredig met de reële geleiding. Excitonen daarentegen, kunnen het veld niet absorberen, maar alleen een beetje vertragen – dit is imaginaire geleiding. Door gelijktijdig de reële en imaginaire geleiding te meten, biedt THz-TDS de unieke mogelijkheid om de effecten van fotoexcitatie te onderzoeken – bijvoorbeeld om de quantum efficientie voor generatie van van vrije ladingen en excitonen te bepalen, alsook de karakterisering van hun transport.

In polaire halfgeleiders (materialen met hoge diëlektrische functie), kunnen wij de eigenschappen van mobiele electronen en gaten onderscheiden door hun karakteristieke respons. In hoofdstuk 4, worden de eigenschappen van vrije elektronen in titaan dioxide (TiO_2) en poreuze TiO_2 (gefuseerde nano-deeltjes, die bijv. in Grätzel zonnecellen worden gebruikt) onderzocht met THz-TDS. TiO_2 is een polaire halfgeleider die veel in foto-katalisatoren en zonnecellen wordt gebruikt. Het is duidelijk dat het ionische karakter van TiO_2 met een sterke elektron-rooster interactie gepaard gaat, hetgeen tot de vorming van een polaron leidt: een deeltje dat uit een elektron en een roostervervorming bestaat. In het pure kristal vinden wij dat het transport wordt beperkt door polaronvorming. Dit is evident vanwege de uitzonderlijk hoge elektron massa (vele malen de massa van een vrij elektron) en een lage elektronenmobiliteit van ~1 cm^2/Vs (bij kamertemperatuur) veroorzaakt. In het poreuze TiO_2 is elektronmobiliteit *op korte tijdsschaal* verder gereduceerd tot ~10^{-3} cm^2/Vs door het afschermen van het elektrische veld. Deze waarde is nog steeds groter dan de mobiliteit *op lange tijdschaal* in poreuze samples, en dus is een significante verbetering van ladingstransport in Grätzel cellen mogelijk als defecten kunnen worden gepassiveerd en het transport tussen de nano-deeltjes kan worden verbeterd. Mobiliteit van elektronen en gaten, die verlaagd is door het afschermen van het elektrische veld, bepaalt de interne weerstand van een cel. De quantum efficientie van de cel wordt bepaald door diffusie van elektronen en gaten naar de elektroden. Het afschermen van het elektrische veld speelt geen rol in de diffusie van ladingsdragers, die onafhankelijk is van het elektrische veld. Dat betekent dat er een lagere interne celweerstand mogelijk is als de volume fractie van het poreuze materiaal groter is, of minder polariseerbare materialen gebruikt worden.

In apolaire halfgeleiders (materialen met lage diëlektrische functie), zijn de elektronen en de gaten met elkaar verbonden (d.i. de vorming van excitonen) en zijn dus geen afzonderlijke, onafhankelijke deeltjes, zoals in materialen met hoge diëlektrische functie (zoals TiO_2). Met THz-TDS kan de drastisch verschillende respons van excitonen in vergelijking met vrije elektronen en gaten een nuttig hulpmiddel zijn in het onderzoek naar de dynamica van vrije en gebonden ladingsdragers. In hoofdstuk 5 onderzoeken wij met THz-TDS de vorming van een exciton gas vanuit een electron-gat plasma met ~1 eV exces energie. In het lage dichtheidsregime, is de dynamica relatief langzaam (op een tijdschaal van ongeveer 100 ps), hetgeen betekent dat het plasma heel koud moet zijn voor de vorming van een exciton gas. De Coulomb-krachten die elektronen en gaten bij lage dichtheid verbindt wordt bij hoge dichtheid afgeschermd, wat in dat geval tot een elektron-gat vloeistof leidt. De overgang van een isolerend gas van excitonen naar een geleidend elektron-gat vloeistof vindt plaats nabij de zgn. Mott dichtheid. Boven deze dichtheid is de vorming van een elektron-gat vloeistof heel snel, (~5 ps). Deze zeer snelle dynamica is aanzienlijk sneller dan de afkoeling van het plasma; de vloeibare fase kan blijkbaar direct vanuit het hete plasma worden gevormd, waarschijnlijk door multi-ladings recombinatie (toegestaan door de directe bandstructuur). Deze conclusie wordt versterkt door de temperatuursafhankelijkheid van de dynamica: terwijl exciton vorming sterk afhankelijk is van de roostertemperatuur, is de vormingsdynamica van de vloeibare fase temperatuursonafhankelijk

Quantum dots (QDs) hebben unieke optische eigenschappen vanwege de beperking van de elektron en gaten golffuncties, wat tot afzonderlijke energie toestanden leidt. Voor QD toepassingen in zonnecellen, is een zeer belangrijke de stap die onmiddellijk na foto-excitatie: het koelen van het foto-geïnduceerde hete elektron en hete gaten naar hun laagste energietoestand. Terwijl in bulk halfgeleiders, de snelle, opeenvolgende emissie van fonon-quanta snel koelen mogelijk maakt, betekent het ontbreken van een continuum van toestanden in QDs dat de energieoverdracht van de hete ladingen aan het rooster in afzonderlijke stappen moet gebeuren. Aangezien de afstand tussen de elektronische toestanden (typisch ~200 meV) groot is in vergeleken met typische LO fonon energiën (~25 meV), vereist dit de gelijktijdige emissie van een grote hoeveelheid fononen, een proces met een lage waarschijnlijkheid. Daarom heeft men voorgesteld dat het koelen van hete elektron in QDs door een zogenaamd "fononknelpunt" wordt belemmerd, resulterend in nanoseconde koelingstijden. In hoofdstuk 6, wordt THz-TDS gecombineerd met tijdsopgelosde luminescentie, om het respectievelijke koelen van gaten en elektronen te onderzoeken in cadmium selenide QDs met diverse diameters. Wij zien voor het eerst overdracht van de elektron energie aan gaten op hele korte tijdschalen, hetgeen Auger koelen voor elektronen bevestigt. Dit mechanisme omzeilt het fononknelpunt, en wij presenteren de eerste kwantitatieve metingen van elektron-gat koppeling in CdSe QDs.

Polymere halfgeleiders zijn goedkope en flexibele alternatieven voor standaard halfgeleiders, zoals silicium. Als zodanig vinden ze toenemend gebruik in opto-electronsiche toepassingen, zoals licht emiterende diodes, beeldschermen en zonnecellen. Ondanks de inspanningen van vele onderzoeksgroepen wereldwijd, is het nog steeds niet duidelijk wat er precies gebeurt wanneer een organische polymere halfgeleider een foton absorbeert. In silicium is reeds lang bekend dat optische excitatie leidt tot de vorming van vrije ladingen. In een halfgeleidend polymeer is het duidelijk dat optische excitatie mede leidt tot de vorming van vrije ladingen, gezien de aanzienlijk geleidbaarheid. Maar er kunnen ook excitonen worden gevormd. Één van de belangrijkste vragen is, of hoofdzakelijk excitonen of vrije ladingen worden gevormd. In hoofdstuk 7, gebruiken wij THz-TDS om het proces van de sub-picoseconde excitatie in twee verschillende fasen van het model halfgeleidende polymeer poly[2-methoxy-5-(2'ethyl-hexyloxy)-1.4-phenylene vinylene] (MEH-PPV) te volgen. In een oplossing is de polymeer concentratie voldoende laag, en de solvatatie (in benzeen) voldoende sterk, zodat wij dit proces in geïsoleerde polymeerketens kunnen onderzoeken. In een ander sample bestaande uit een dunne, gecondenseerde film zijn inter-keten interacties wel aanwezig. Door op femtoseconde tijdschaal zowel reële als imaginaire geleiding te meten, is het duidelijk geworden dat voornamelijk excitonen gevormd worden, met een efficiency van bijna 100%; in de oplossing worden zeer weinig ladingen gevormd (< 0.1%), en die zijn daarbij ook nog maar een hele korte tijd mobiel: slechts 1 ps (10^{-12} s). In de film, wordt een groter aantal vrije ladingen gevormd (<1%), dus interactie tussen ketens helpt de dissociatie van excitonen. Voor toepassingen in bijv. zonnecellen is dit resultaat belangrijk, omdat het duidelijk maakt dat het onstane exciton op een of andere manier gedissocieerd moet worden; pas dan kan geleiding van de tegengestelde ladingen naar de verschillende electrodes plaatsvinden.

Acknowledgments/Dankwoord

It is a difficult task to list all the people who contributed, directly and indirectly, to this thesis. I therefore apologize in advance for anyone I have (inevitably…..) forgotten to mention below.

Firstly, I would like to thank my promoter, Mischa Bonn, for giving me the opportunity to come to the Netherlands. Your guidance and friendship have been important to me these last four years, and I hope we can continue to work together in the future. I would also like to thank our many close scientific collaborators. Firstly, Feng Wang, Jie Shan and Tony Heinz – thanks for the comprehensive introduction to THz spectroscopy, the pleasant ensuing collaboration and for making my stay in New York such a pleasant one. I express gratitude towards Juleon Schins and Laurens Siebbeles from Delft, and Celso de Mello Donegá and Daniel Vanmaekelbergh from Utrecht, for the fruitful collaborations. I must also thank Hong Zhang from the University of Amsterdam for allowing me to access his fluorescence up-conversion set-up, contributing to the results presented in chapter 6. For several helpful THz and conductivity related discussions, I thank Aart Kleyn, Paul Planken and Brian O'Regan. From Berlin, I am grateful to Klaus Reimann, Tobias Kampfrath and Luca Perfetti for making our trips there both productive and enjoyable. Aside from our collaborations, the work in this thesis could not have taken place were it not for the excellent technical support, both in Leiden (specifically, Rob van Schie and Peter Schakel) and at Amolf (Ilja Stavenuiter, Hinco Schoenmaker and Rob Kemper).

I am also very grateful to all the great people I have had around me for the last four years, who contributed to a fantastic working atmosphere. In Leiden (in order of increasing ratio of height to shoe size): Ellen, Michael, Otto, Sylvie, Emile, Johan and Mike. And last, of course, Wim. I am grateful for the many drunken evenings and all the nonsensical talk! A particular thank you to Mattijs for sharing both the frustration and successes of working day to day on the THz set-up. I truly enjoyed working with you over the last three years (and I honestly felt bad about kicking your butt on the squash court all those times...). Equally congenial were the group members at Amolf (in order of increasing moronisity [1]): Maria, Doseok, Han-Kwang, Chien-Ching, Sjors, Marc and Avi – memorable times were aplenty!

A special mention must also go to the Stoere Mannen en Vrouwen: Lulu, Yvonne (and Baby Lulyv), Cece* and Cece#, Jeje and Cecile, Stefan, J.T. Harvey [2], Pepa and

---

[1] I would like to point out that this is not meant to be insulting. Indeed, at Amolf, being a "moron" is quite an honour.

[2] Appl Ergon. **33**, 523 (2002).

[3] Plagiarized from "Monty Python and the Holy Grail".

*Cedric Crespos

#Cecile Coriole

Helen: I blow my nose at you [3]. Thanks for the gloriously coconutty adventures in Bordeaux, Liverpool, Paris, Bayonne, Bordeaux, Bunol and, of course, Scotland. Long may the Verbond van Stoere Mannen en Vrouwen continue!

Outside of science, I am in particular grateful to Ollie and her family for many happy times in the last year or two. Ik zal me altijd Sinterklaas 2004 blijven herinneren! I also thank the guys from LUSV Badminton, from Friday Night Football, and my tennis buddy Alan Choi, for keeping me (reasonably…..) fit for the rigors of a PhD.

Though this thesis presents work from the past four years, I would also like to express my thanks to some people who helped me on the way to the Netherlands. Malcolm Kadodwala, my previous supervisor, initiated everything by kindly arranging my summer placement in Leiden in 2000. I am also grateful to Andy, David and the rest of the guys from ChemPhys, for not shouting at me too much when I turn up a few hours late for our reunions. I would also like to thank my oldest (not eldest) friends: Stewart, Barry, Graham and Darren, for keeping me up to date with all the latest news/rumors from back home.

Last, but certainly not least, I would like to thank my family for the unconditional love and support they have always given me, in particular over the last four years. To my brothers, Gareth and Scott, and Mum and Dad: Glenmavis will always be “home” to me.

Euan

Subjects dealt with in this thesis:

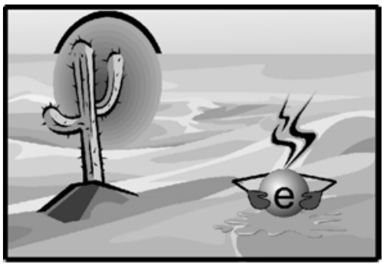

(Hot electrons)

(Electron thermalization)

(Electron confinement)